NOVA SCHOOL OF SCIENCE & TECHNOLOGY

DEPARTMENT OF PHYSICS

BEATRIZ DOS REIS ANTUNES PAIS

BSc in Biomedical Engineering

AUTOMATED MICROFLUIDIC PLATFORM FOR QUANTITATIVE ANALYSIS OF MOLECULAR TRANSPORT ACROSS BIOMIMETIC INTERFACES

MASTER IN BIOMEDICAL ENGINEERING

NOVA University Lisbon
September, 2025

NOVA SCHOOL OF SCIENCE & TECHNOLOGY

DEPARTMENT OF PHYSICS

AUTOMATED MICROFLUIDIC PLATFORM FOR QUANTITATIVE ANALYSIS OF MOLECULAR TRANSPORT ACROSS BIOMIMETIC INTERFACES

BEATRIZ DOS REIS ANTUNES PAIS

BSc in Biomedical Engineering

Adviser: Miguel Neves
Associate Researcher, i3S - Institute for Research and Innovation in Health, University of Porto

Co-adviser: João Cruz
Associate Professor, NOVA School of Science and Technology

Examination Committee

Chair: Célia Henriques
Associate Professor, NOVA School of Science and Technology

Rapporteur: Rui Igreja
Full Professor, NOVA School of Science and Technology

Member: Miguel Neves
Associate Researcher, i3S - Institute for Research and Innovation in Health, University of Porto

MASTER IN BIOMEDICAL ENGINEERING

NOVA University Lisbon
September, 2025

Automated Microfluidic Platform for Quantitative Analysis of Molecular Transport across Biomimetic Interfaces

This document was created with the (pdf/Xe/Lua)LaTeX processor and the NOVAthesis template (v7.2.5) [1].

To my parents Vanda and João, and my brother Miguel.

Acknowledgements

The completion of a Master's thesis is both a demanding and rewarding journey, and it is one I could never have accomplished alone. Over the past months, I have experienced many challenges as well as moments of growth and achievement, and I have been fortunate to be surrounded by people who supported me, encouraged me, and walked by my side throughout this process.

First and foremost, I would like to express my deepest gratitude to my supervisor Miguel Neves at i3S/FMUP for his unwavering support and guidance. You were always ready to listen, to give me advice, and to encourage me to follow the best path forward. Thank you for being open to new ideas, for creating such a welcoming environment at the workplace, and even for teaching me to appreciate a good *francesinha*. To my co-supervisor, Professor João Cruz at NOVA School of Science and Technology, thank you for always being ready to help whenever I needed support, even when my work fell outside your direct area of expertise. Your promptness and willingness to assist were invaluable.

I am also grateful to the Lifesaver Project and its Consortium, particularly to the colleagues with whom I worked directly and who helped shape this thesis: Inês Mendes Pinto from i3S in Porto, Lisa Muiznieks, Olivier Fournier and Ivana Brenta from the Microfluidics Innovation Center in Paris, Michael Gasik from Seqvera in Helsinki, and Andrea Cruz from the International Iberian Nanotechnology Laboratory in Braga. Thank you for your kindness and understanding in a world that often feels overwhelming.

To NOVA School of Science and Technology, my academic home for the past five years, I owe sincere thanks for the knowledge, experiences, and friendships that culminated in this milestone. What a long journey it has been—from my very first online classes during the COVID pandemic to finally graduating alongside the wonderful friends I made along the way. To all of them, you have a permanent place in my heart. Daniela, thank you for being the kindest and most considerate roommate. I would also like to thank Margarida and Madalena whose friendship has been a constant in my life. I am deeply grateful for the strength and joy you continue to bring me. And most importantly to my boyfriend, Gil—thank you for sharing every step of this journey with me, for giving me the best advice when I needed it, and for laughing with me through life. I love you deeply

wherever we might be.

Finally, I turn to the most important people in my life—my family. To my grandparents, uncles, aunts, cousins, and especially to my brother Miguel: thank you for your endless love and support. To my mom and dad, words will never be enough to express my gratitude. You have been my foundation since day one, and everything I achieve, I achieve because of you. This thesis is dedicated to you.

To all those who encouraged me, guided me, and cheered me on during this process: thank you. I am truly grateful.

”

“O caos é uma ordem por decifrar.”

— José Saramago, Livro dos Contrários
(Writer)

Abstract

A comprehensive understanding of human physiology and disease is crucial for advancing drug discovery and developing effective therapies. This requires physiologically relevant *in vitro* models supported by standardized, robust, and reproducible methods. Traditional 2D cell cultures and animal models often fail to mimic the dynamic microenvironments and selective transport functions of human tissue barriers. While microfluidic barrier models offer better biomimicry, many are limited by technical complexity, lack of standardization, and insufficient real-time analysis capabilities, especially under non-equilibrium conditions. Non-equilibrium molecular transport is a critical feature of many biological barriers, including the renal tubule, blood–brain barrier, intestinal epithelium, and placental interface. These systems rely on active transport mechanisms, directional fluid flow, and dynamic concentration gradients that cannot be accurately modeled using static or oversimplified systems. This work presents a fully automated microfluidic platform with programmable control and closed-loop feedback for standardized analysis of molecular transport across biomimetic tissue barriers. It enables dynamic regulation, precise fluid handling, and high-resolution monitoring, with continuous compensation for solvent drag and hydrostatic pressure. Proof-of-concept validation demonstrates the system's potential to minimize user intervention, improve reproducibility, and support inter-laboratory standardization. The platform offers scalable, high-fidelity modeling of barrier function under dynamic conditions, with broad applications in translational research and preclinical drug development.

Keywords: Microfluidics, Fully Automation, Non-Equilibrium Molecular Transport, Organ-on-a-chip, Biological Barriers

Resumo

Uma compreensão abrangente da fisiologia humana e dos mecanismos das doenças é fundamental para o avanço da descoberta de fármacos e o desenvolvimento de terapias eficazes. Tal requer modelos *in vitro* fisiologicamente relevantes, sustentados por metodologias padronizadas, robustas e reprodutíveis. Culturas celulares 2D e modelos animais, por norma, falham ao replicar os microambientes dinâmicos e as funções de transporte seletivo das barreiras tecidulares humanas. Embora os modelos de barreira microfluídicos ofereçam um biomimetismo melhorado, muitos permanecem limitados pela complexidade técnica, falta de padronização e capacidades insuficientes para análise quantitativa em tempo real, especialmente em condições de não-equilíbrio. O transporte molecular em condições de não-equilíbrio é uma característica crítica de várias barreiras biológicas, incluindo o túbulo renal, a barreira hematoencefálica, o epitélio intestinal e a interface placentária. Estes sistemas dependem de mecanismos de transporte ativo, fluxo de fluido direcional e gradientes de concentração dinâmicos, que não podem ser modelados com precisão usando sistemas estáticos ou simplificados. Este trabalho apresenta uma plataforma microfluídica totalmente automatizada, com controlo programável e *feedback* em circuito fechado, para análise padrão do transporte molecular através de barreiras tecidulares biomiméticas. A plataforma permite a regulação dinâmica das condições experimentais, controlo preciso de fluidos e monitorização de alta resolução, com compensação contínua de forças como o deslocamento de solvente e a pressão hidrostática. A validação da prova de conceito demonstra o potencial do sistema para minimizar a intervenção do utilizador, melhorar a reprodutibilidade e apoiar a padronização interlaboratorial. A plataforma oferece um modelo escalável e de elevada fidelidade da função de barreira em condições dinâmicas, com ampla aplicabilidade na investigação translacional e no desenvolvimento pré-clínico de fármacos.

Palavras-chave: Microfluídica, Automatização Integral, Transporte Molecular de Não-Equilíbrio, Orgão-num-Chip, Barreiras Biológicas

Contents

List of Figures

List of Tables

Acronyms

ATP Adenosine Triphosphate *(pp. 10, 14, 15)*

BBB Blood Brain Barrier *(pp. 1, 2, 6, 11, 13–15)*
BSA Bovine Serum Albumin *(pp. 16, 17, 21, 22, 24, 25, 33–36)*

CFD Computational Fluid Dynamics *(pp. 22, 34, 35)*

DO Dissolved Oxygen *(pp. 16, 27, 37, 39)*

ECM Extracellular Matrix *(pp. 1, 6, 11)*
EPDM Ethylene Propylene Diene Monomer *(p. 20)*
ETFE Ethylene Tetrafluoroethylene *(p. 19)*

FBS Fetal Bovine Serum *(p. 38)*

GFB Glomerular Filtration Barrier *(pp. 14, 33)*

hiPSC human induced Pluripotent Stem Cells *(p. 7)*
HPLC-MS High-Performance Liquid Chromatography-Mass Spectrometry *(pp. 7, 8)*

ID Inner Diameter *(pp. 19, 20, 78)*

MC Microfluidic Chip *(p. 3)*
MPS Microphysiological Systems *(pp. 5, 38, 39)*
MWCO Molecular Weight Cut-Off *(pp. 10, 20, 22, 33)*

NEMD Non-equilibrium Molecular Dynamics *(pp. 15, 16)*

OC Organ-on-a-Chip *(pp. 5–7, 16, 37–39)*

OD Outer Diameter *(pp. 19, 20, 78)*

p_{abs} Absolute Pressure *(p. 37)*
PBS Phosphate Buffer Saline *(pp. 20, 22, 24, 32)*
PDMS Poly(dimethylsiloxane) *(pp. 3, 6)*
PEEK Polyether Ether Ketone *(p. 19)*
PFA Perfluoroalkoxy *(p. 19)*
PID Proportional-Integral-Derivative *(pp. 28, 30, 34)*
PLA Polylactic Acid *(p. 19)*
PMT Photomultiplier Tube *(p. 24)*
pO_2 Oxygen Partial Pressure *(pp. 31, 37)*
PoC Placenta-on-a-Chip *(p. 7)*
PTFE Polytetrafluoroethylene *(p. 19)*

R1 Reservoir 1 *(pp. 4, 22, 30–32)*
R2 Reservoir 2 *(pp. 4, 22, 30–32)*
RS Recirculation System *(pp. 3, 4)*

UV Ultraviolet *(pp. 22, 23, 35)*

1

Introduction

1.1 Microfluidic-based Organ-on-a-Chip Technologies

Advancing our mechanistic understanding of human pathophysiology—and, by extension, enhancing drug development and evaluation—faces a crucial obstacle: effectively translating encouraging *in vitro* findings into successful clinical outcomes. The substantial attrition rate in drug discovery, with average research and development costs per approved therapy exceeding 2.8 billion dollars and only about 6.7% of candidates advancing from Phase I trials to regulatory approval, underscores a persistent translational gap [2–4]. This challenge is largely attributed to the limitations of traditional preclinical models.

1.1.1 Limitations of Traditional *in vitro* and *in vivo* Models

Although widely employed in early drug testing, traditional two-dimensional (2D) static culture systems fail to recreate the complex structural, mechanical, and biochemical environment inherent to living tissues, as extensively reported in the literature [5–7]. Accurate *in vivo* drug responses depend strongly on physiologically relevant features such as extracellular matrix (ECM) interactions, cellular diversity, spatiotemporal biochemical gradients, mechanical deformation, shear forces, and interstitial fluid dynamics [5, 8–11]. Animal models, designed to mitigate this translational gap, frequently present species-dependent variations in drug metabolism, transporter activity, immune mechanisms, and intracellular signaling pathways, thereby constraining their applicability to human physiology [12, 13]. These discrepancies are especially critical when evaluating molecular transport across physiological barriers.

Biological barriers—including the blood brain barrier (BBB), intestinal epithelium, alveolar capillary interface, placental barrier, and glomerular filtration barrier—function as dynamic and selectively permeable structures that tightly control the movement of ions, metabolites, and macromolecules between tissues and the systemic circulation [14–18]. Developing physiologically relevant models of these barriers is crucial for deepening our understanding of pharmacokinetic mechanisms—spanning drug absorption, distribution, metabolism, and excretion—and for uncovering the underlying processes that drive a

wide range of pathological conditions, including neurodegenerative disorders, cancer metastasis, and maternal–fetal diseases, among others [18–21]. Conventional *in vitro* systems frequently fall short of reproducing the intricate cellular and structural interactions that define these dynamic interfaces, resulting in unreliable assessments of drug permeability, therapeutic efficacy, and toxicity. For example, static BBB that omit critical cell–cell communication—such as interactions between astrocytes and endothelial cells—and lack physiological shear forces often overpredict drug transport and fail to accurately represent active efflux mechanisms mediated by specific transporters [19–22]. Furthermore, many *in vivo* animal models, including placental models (Fig. 1.1), do not accurately reproduce critical human physiological and molecular characteristics, thereby limiting their translational validity [23]. At the same time, ethical and regulatory frameworks, exemplified by the European Union 3R's initiative, promote the reduction, refinement, and eventual replacement of animal experimentation in preclinical research, underscoring the importance of developing advanced, human-relevant *in vitro* model systems [24].

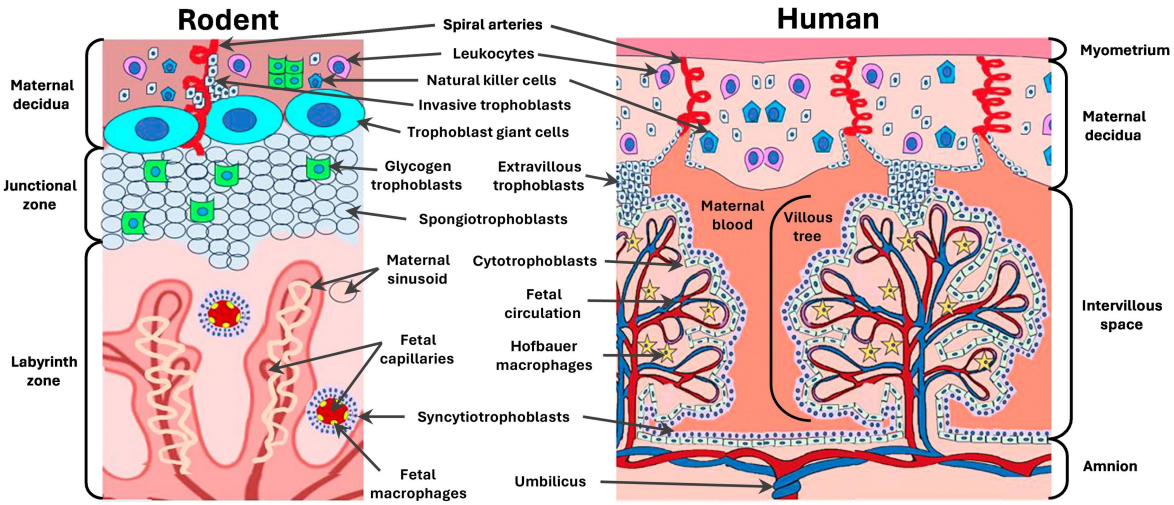

Figure 1.1: **Composition of rodent *versus* human maternal-fetal interfaces.** Both humans and rodents share a hemochorial placenta, where maternal blood is in direct contact with fetal trophoblasts. However, the structural organization and cell types differ: humans feature an intervillous space formed by villous trees, while rodents possess a labyrinth zone. Humans rely on cytotrophoblasts, syncytiotrophoblasts, and extravillous trophoblasts, whereas rodents also have unique cell types such as trophoblast giant cells, spongiotrophoblasts, and glycogen trophoblasts, which contribute to hormone production and maternal tissue remodeling. Adapted from [23].

1.1.2 Microfluidics

Microfluidics is the science and technology of manipulating small fluid volumes through channels of tens to hundreds of micrometers in dimension. Besides allowing the analysis of small sample quantities in a short time, microfluidics also permits to carry out separations and detections with high resolution and sensitivity at a low cost [25].

The essential idea of microfluidics is to integrate operations that usually require a whole laboratory in a simple micro-sized system. Therefore, the development of microfluidic

systems is of utmost pertinency. A microfluidic chip (MC) is constituted by channels usually embossed in the surface of a material such as glass, silicon, or most commonly, poly(dimethylsiloxane) (PDMS). This network of microchannels inside the MC connects to the macro-world through inlets and outlets present on the chip (Fig. 1.2).

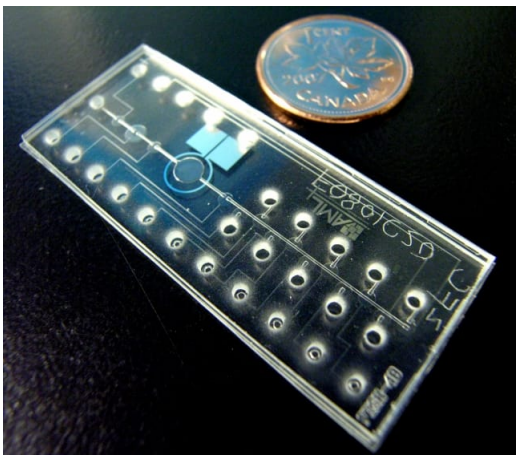

Figure 1.2: **Example of a microfluidic chip.** Size comparison with a coin. Adapted from [26].

Using this technology, fluids are directed, mixed, separated or manipulated in order to obtain multiplexing, automation, and high-throughput systems. Some of the desired features of MCs are, for example, detection of pathogens, electrophoresis and lab-on-a-chip[1] analyses [26]. However, MCs are not the only approach to performing microfluidic operations; microtubing and many pressure-driven flow designs can also be employed in the field of microfluidics. To keep fluids running through a microfluidic device, high-precision fluid control systems are required, such as a pressure controller, pumps/syringes, flow and pressure sensors, and valves [27].

1.1.2.1 Pressure-Driven Flow Microfluidics

Microfluidics is an overly broad field of study. This work is focused on pressure-driven flow microfluidics in recirculating systems using a pressure controller (Annex I.1), pressure and flow sensors (Annex I.2) and valves, emphasizing on a check valve design forming a 'recirculating bridge' (Annex I.3).

Fluid recirculation facilitates the transport of nutrients, drugs, and cell secretions within a circulating environment that mimics physiological conditions. With this mechanism, the fluid arriving to an outlet of the MC is reinserted in the circuit. There are different recirculation system (RS) setups, suitable for specific applications, such as hydrostatic pressure RS, loop RS, and syringe, peristaltic or pressure pump RS [28].

Concerning the fluid's direction, the circulation can be unidirectional or bidirectional. Figure 1.3 represents one way of a bidirectional RS. Adding a valve system to that circuit

[1]Type of microfluidic application able to integrate many medical tests in one chip only, hence leveraging its importance in biomedical engineering.

enables a unidirectional flow path, which is interesting when reproducing physiological conditions, given that blood flow is unidirectional in the human vasculature [29].

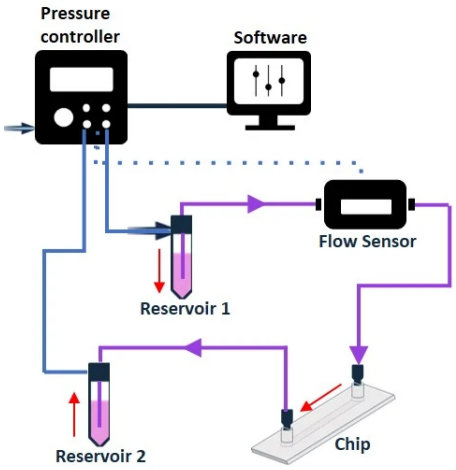

Figure 1.3: **Bidirectional recirculating system using a pressure pump.** The flow from reservoir 1 (R1) to reservoir 2 (R2) is shown here, but the system can also operate in reverse. From [28]

There are diverse types of valves that can be used in a unidirectional circulation loop. These are rotatory, check, pinch and 3/2 valves. Using the recirculating bridge assembly (Annex I.3), it is possible to design an automated unidirectional RS [28], as represented in Figure 1.4.

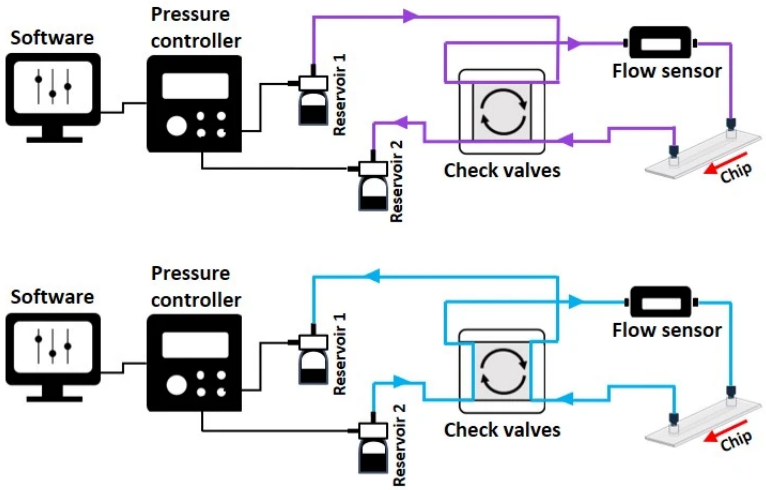

Figure 1.4: **Automated unidirectional recirculation system using a recirculating bridge.** Fluid goes from R1 to R2 (top) and from R2 to R1 (bottom), but notably the flux direction in the chip remains unchanged. Adapted from [28].

To regulate the fluid flow rate on the microfluidic system, it is important to bear in mind some properties that influence the channels' hydraulic resistance [30], in particular the length and inner diameter of the tubing, and the fluid's viscosity and density.

The Hagen-Poiseuille law states that

$$Q = \frac{\Delta P \pi r^4}{8 \mu L}, \tag{1.1}$$

where Q is the flow rate, ΔP is the pressure difference between the inlet and the outlet of the chip, μ is the fluid's viscosity, r is the inner radius and L is the length of the tubing.

The hydraulic resistance (R_h) of a channel is given by

$$R_h = \frac{8 \mu L}{\pi r^4} \tag{1.2}$$

Based on equations 1.1 and 1.2, equation 1.3 is deducted. It is simpler and provides a good estimate for microchannels whose $r << L$ [30].

$$Q = \frac{\Delta P}{R_h} \tag{1.3}$$

From equation 1.3, one understands that to diminish the flow rate without changing the fluid properties, either the resistance increases, which is feasible by increasing the length or reducing the inner radius of the channels, or ΔP decreases. The opposite thinking applies when an increased flow rate is desired.

1.1.3 Integration of Microfluidic Barrier Models Into Organ-on-a-Chip Systems

Microphysiological systems (MPS), encompassing organ-on-a-chip (OC) technologies, have rapidly evolved into groundbreaking platforms for drug discovery and biomedical research. They present highly predictive and human-relevant alternatives to both traditional *in vitro* culture methods and conventional *in vivo* animal models [19, 20, 31, 32]. By combining three-dimensional tissue architectures with microfluidic flow, finely tuned environmental control, and the coordinated growth of multiple cell types, these systems recreate critical aspects of the native *in vivo* milieu. This capability enables the investigation of complex physiological processes—including nutrient and metabolite transport, mechanical stimulation, cellular metabolism, and immune interactions—with a realism unattainable in static culture or animal testing [32–34].

A typical OC consists of 3D cell cultures embedded in a microfluidic chip, which acts as both the vascular and structural support of a natural organ, while also allowing real-time monitoring and experimental manipulation [26]. The chip connects to external systems through inlets and outlets and can be fabricated in different structural formats—including microchannels, culture chambers, membrane layers, or modular architectures [35].

Particularly important in drug screening applications are microfluidic barrier models, which typically consist of two or more channels separated by a semipermeable membrane, allowing researchers to investigate selective permeability, transport kinetics, and barrier integrity across physiological interfaces [11, 36]. Advanced designs have increasingly incorporated co-cultures of relevant cell types (e.g., astrocytes, neurons, and pericytes in

BBB models), ECM components (e.g., collagen, laminin, and fibronectin) and microfabricated features (e.g., perfusable microvessels and microchannels), in order to replicate the structural and functional complexity of human tissues [11, 21, 32]. Moreover, recognizing that drug toxicity often impacts multiple organs simultaneously has driven the evolution of OC technology toward multi-organ-on-a-chip systems [35]. These interconnected models provide a more systemic perspective on drug metabolism and toxicity.

The versatility of microfluidic barrier models is demonstrated across various organ systems. The following examples illustrate their diverse applications in simulating organ-specific pathophysiology and evaluating therapeutic interventions.

Kidney-on-a-chip models have been instrumental in studying renal injury and drug-induced nephrotoxicity. Kim et al. [37] developed a kidney-on-a-chip model to study glomerular filtration barrier dysfunction. By integrating tunable basement membrane deposition and a 3D co-culture of glomerular endothelial cells and podocytes, the model replicated the biphasic response of the barrier, showing how membrane thickness affects permeability. Additionally, nephrotoxic injury experiments revealed that damaged podocytes overproduce vascular endothelial growth factor A, contributing to barrier impairment. This kind of research studies will prove useful in further investigations into kidney pathologies and how to prevent/treat them.

OC microfluidic platforms have also been widely applied in respiratory research. Tan et al. [38] created a PDMS-based lung-on-a-chip to assess EGFR[2]-targeted drugs for non-small cell lung cancer. The chip featured two microfluidic channels separated by a porous membrane, allowing co-culture of lung cancer and endothelial cells under continuous perfusion to mimic physiological conditions, whose schematic is represented in Figure 1.5. Compared to 2D well-plates, the 3D lung chip provided more clinically relevant drug responses, reducing cancer cell viability across all tested compounds.

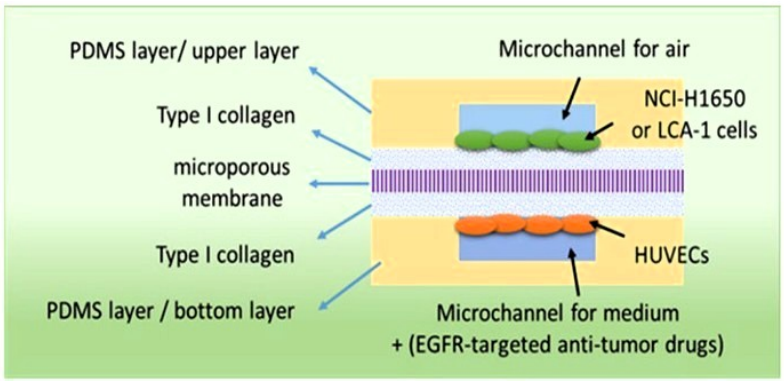

Figure 1.5: **Schematic of a lung-on-a-chip composition with a microporous membrane integrated.** Adapted from [38].

In order to study enteric coronavirus infection and drug responses in the gut, Bein

[2]Epidermal growth factor receptor is a protein involved in cell growth, survival, and proliferation often overexpressed or mutated in certain cancers.

et al. [39] developed a human immunocompetent intestine-on-a-chip. The microfluidic device, represented in Figure 1.6, lined with patient-derived intestinal epithelial cells and human vascular endothelium, mimics physiological conditions by incorporating fluid flow and peristalsis-like motions. Upon infection with NL63 coronavirus, the chip exhibited inflammation, cytokine secretion, immune cell recruitment, and barrier disruption, effectively recapitulating gastrointestinal pathology. Drug testing showed Nafamostat[3] reduced viral load, while Remdesivir[4] was ineffective and toxic to the endothelium. This platform provides a promising preclinical tool for studying viral gut infections and screening antiviral therapies.

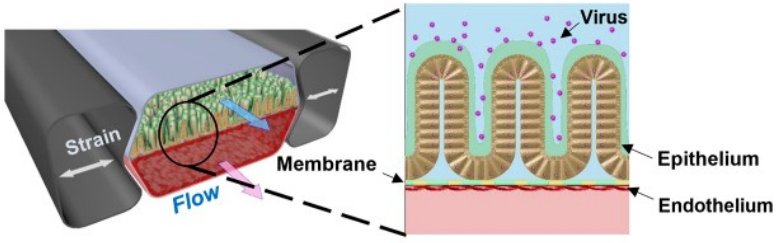

Figure 1.6: **Schematic of a intestine-on-a-chip to study viral infection.** Adapted from [39].

Extending the application of OCs to neurodevelopmental research, Wang et al. [40] introduced a human induced pluripotent stem cells (hiPSC)-derived brain organoid-on-a-chip to model prenatal nicotine exposure and its effects on early fetal brain development. As represented in Figure 1.7, the chip had five parallel channels and enabled 3D culture, neural differentiation, and self-organization of brain organoids under controlled microfluidic conditions. Nicotine exposure led to premature neuronal differentiation, disrupted brain regional organization, abnormal cortical development and neuronal outgrowth, mimicking neurogenesis defects observed in nicotine-exposed fetal brains.

Concerned by the adverse effects of caffeine on human placental function, Pemathilaka et al. [41] investigated caffeine transport across the placental barrier using high-performance liquid chromatography-mass spectrometry (HPLC-MS). Their microfluidic model, with trophoblast and endothelial cells on the maternal and fetal sides, respectively, separated by a porous membrane, confirmed caffeine permeability, as shown in Figure 1.8. The authors emphasized the need to study how varying caffeine concentrations impact transfer rates. The same placenta-on-a-chip (PoC) assembly was used by Zhu et al. [42] to study inflammatory responses to bacterial infections, focusing on *Escherichia coli* (*E. coli*). The bacteria-induced inflammation triggered cell death in both trophoblasts and endothelial cells and transplacental signaling induced an inflammatory response on the fetal side, even without direct bacterial transmission. Nevertheless, maternal macrophages adhered to the trophoblast layer following infection, indicating immune activation against inflammation.

[3]Membrane protease inhibitor. Drug approved for clinical use for pancreatitis and disseminated intravascular coagulation [39].

[4]Intravenous drug with emergency use authorization for COVID-19 [39].

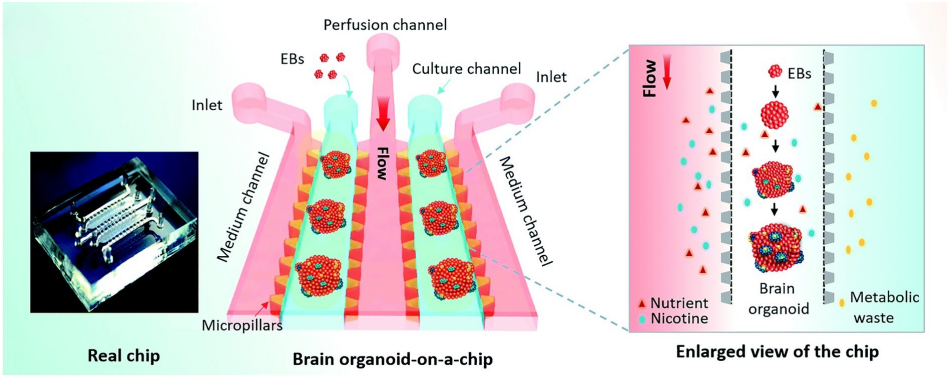

Figure 1.7: **Brain organoid-on-a-chip.** The organoid-on-a-chip device (left); schematic of the brain organoid-on-a-chip configuration (middle); engarged view of the organoid generation process (right). This system was established for embryoid bodies culture, neural differentiation and formation of brain organoids by integrating a 3D Matrigel and a constant fluid flow using a syringe pump, thus creating a controlled microenvironment for brain development. Adapted from [40].

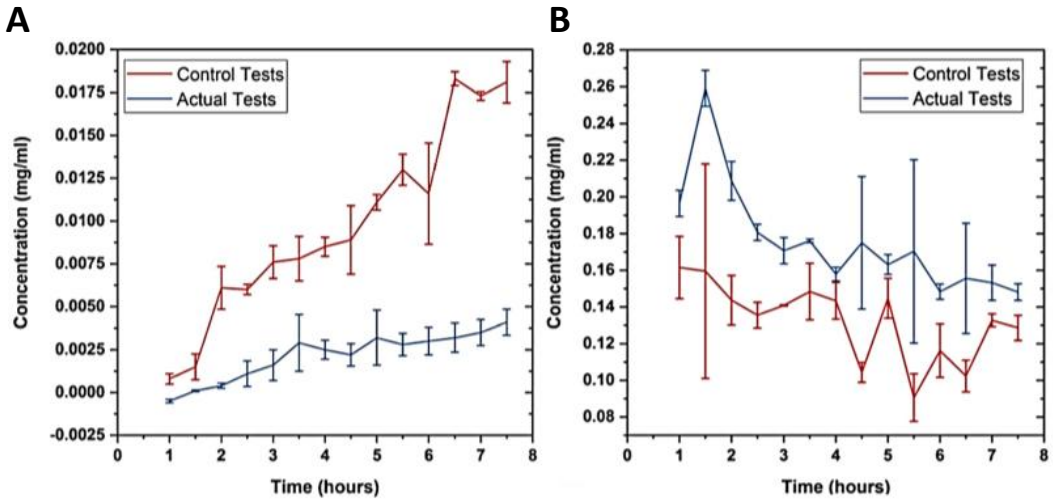

Figure 1.8: **Caffeine concentrations calculated for both fetal (A) and maternal (B) sides from HPLC-MS data.** A 0.25 mg/mL caffeine solution was introduced in the maternal channel and its diffusion into the fetal channel was monitored for 7.5 hours. A gradual increase in the fetal side's caffeine concentration was observed, while the maternal caffeine concentration decreased. Actual tests have both endothelial and trophoblast cells on the chip and the control tests have solely the membrane with media perfusing through the channels. Adapted from [41].

1.1.4 Advantages and Limitations of Current Microfluidic Barrier Models

Despite recent advancements in microfluidic technologies, widespread adoption and functional deployment of barrier-on-chip models are constrained by technical complexity, manual operation; including lack of automated fluid handling and feedback control, limited temporal resolution and capture of dynamic gradients, hindering reproducibility. A critical and unresolved challenge lies in accurately modeling and quantifying non-equilibrium molecular transport phenomena, which involve a complex interplay of passive diffusion, active transport, convective flows, and osmotic forces occurring simultaneously under heterogeneous fluid compositions and dynamic flow conditions. Table 1.1 adresses

the main advantages and limitations of recent microfluidic technologies.

Table 1.1: Comparison of main advantages and limitations of current microfluidic barrier models.

Advantages	Limitations
Physiological relevance: 3D tissue architecture, dynamic flow, and co-cultures.	**High complexity:** Requires multidisciplinary expertise and precision setup.
Versatility: Simulates key processes like nutrient transport, shear stress, metabolic activity, and immune responses.	**Manual operation:** Lacks automation and real-time feedback.
Co-culture integration: Supports ECM components and multiple cell types.	**Inability to fully simulate non-equilibrium molecular transport phenomena.**
Ethical advantage: Reduces need for animal testing.	**Low temporal resolution:** Difficult to track time-dependent biological gradients.
Pharmacological utility: Enables drug screening with predictive accuracy.	**Reproducibility issues:** Non-standard protocols across laboratories.
	Scalability issues: Not yet optimal for high-throughput testing.

1.2 Molecular Transport Across Semipermeable Barriers

The simplest and most fundamental semipermeable barrier in biology is the cellular plasma membrane, which surrounds individual cells and tightly regulates the exchange of molecules with their environment. As the primary interface between the cell and its surroundings, the plasma membrane serves as the archetype for understanding molecular transport across biological barriers. However, in multicellular organisms, additional and often more complex barriers exist, formed by the coordinated interaction of multiple cell layers and extracellular structures. In this section, the principles of transport across the plasma membrane will be outlined before extending the discussion to multicellular barriers, where transport becomes more specialized and tightly regulated.

Biological membranes are semipermeable—they permit the passage of certain molecules such as water, while restricting others. Transmembrane transport is governed by intricate interactions among membrane lipids, proteins, and carbohydrates, and is primarily determined by the size, charge, and solubility of the molecules attempting to cross (Fig. 1.9). This selectivity is essential for cellular homeostasis, allowing the plasma membrane to regulate its internal environment, sense external signals, and facilitate metabolic processes [43]. Importantly, membrane transport can occur via either active or passive mechanisms, with the fundamental distinction between them being whether or not energy input is required to move molecules across the membrane.

The movement of solutes across biological membranes is categorized into passive and active transport mechanisms. Passive transport operates without the need for external energy, relying solely on the inherent concentration or electrochemical gradients of the

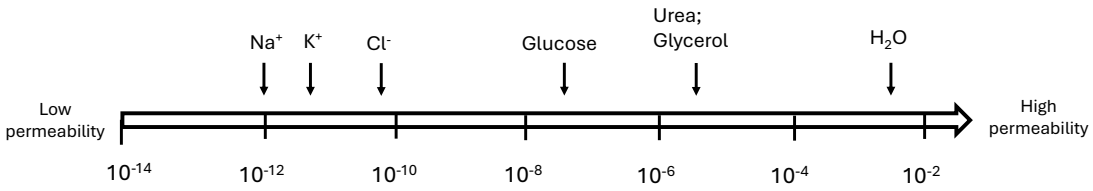

Figure 1.9: **Logarithm of permeability coefficient (in cm/s) across lipid bilayer membranes for common solutes.** Adapted from [43].

solutes. Under passive conditions, solutes distribute themselves until equilibrium is achieved on both sides of a membrane. Passive diffusion may occur directly, with molecules traversing the barrier unaided, or it can be facilitated by specific membrane proteins that selectively enhance the transport of certain solutes. In contrast, active transport requires an input of metabolic energy, typically provided by adenosine triphosphate (ATP), allowing solutes to move against their concentration gradients, using membrane proteins as pumps or carriers. As a result, active transport establishes and maintains non-equilibrium distributions of molecules, with accumulation of specific solutes on one side of the membrane [43, 44].

Osmosis, refering to the flow of water across a semipermeable barrier, is a specific type of diffusion. Water moves down its potential gradient until equilibrium is reached. The pressure required to inhibit water movement is referred to as the osmotic pressure. Even though biological barriers are not perfectly selective (that is, with a reflection coefficient (σ) equal to 1), some are highly effective semipermeable barriers with $\sigma \approx 0.75 - 1$ [43].

1.2.1 Equilibrium Molecular Transport

In equilibrium scenarios, no external driving forces act on the system—the concentration on both sides of the membrane changes until equilibrium is achieved. In static conditions, the net flow of molecules allways occurs down their concentration gradient, until equilibrium is reached and net movement stops [45]. Dyalisis membranes with a defined molecular weight cut-off (MWCO) exemplify equilibrium-controlled transport: molecules smaller than the MWCO can diffuse through, while larger species are retained [46].

Fick's First Law mathematically expresses the principle of diffusion and serves as a cornerstone for understanding molecular transport across barriers.

$$J = -DA\frac{dc}{dx}, \tag{1.4}$$

where J is the diffusion rate, D is the diffusion coefficient (dependent on solute size and molecular weight), A is the cross-sectional area for transport, and $\frac{dc}{dx}$ is the concentration gradient. However, this traditional Fick's First Law is based on the assumptions of local equilibrium and linear response. In non-equilibrium situations—particularly when the medium is heterogeneous or when transport coefficients vary, such as under applied pressure differentials—these assumptions may no longer hold, necessitating the

use of corrected formulations or alternative models to accurately describe molecular transport [47].

1.2.2 Non-equilibrium Molecular Transport

Living organisms are open, non-equilibrium, self-organizing, and dissipative systems that are sustained through the continuous exchange of matter, energy, and information with their surroundings. The processes that occur within molecular and cellular biological systems are inherently stochastic, span multiple spatial and temporal scales, and are governed by conservation principles, kinetic laws, and thermodynamic constraints—all of which must be considered in any attempt to model biological systems accurately [48, 49].

Non-equilibrium molecular transportunderpins the function of several critical organs—including the kidney, lung, and BBB—where tightly regulated and dynamic exchanges of solutes sustain key physiological processes such as filtration, absorption, and selective permeability [50, 51]. For instance, the glomerular filtration barrier in the kidney operates as a passive, charge- and size-selective filter, permitting only small molecules (approximately 15-30 kDa) to traverse into the urinary space. Accurately modeling or predicting filtration dynamics, however, remains challenging because large plasma proteins retained within the bloodstream create substantial osmotic gradients. These gradients generate solvent drag and may even reverse solute movement through interactions like hydrogen bonding and electrostatic attraction [52]. The inability to mimic such dynamic transport behaviors significantly limits the accuracy and translational relevance of *in vitro* experimental models [53–56].

Non-equilibrium transport occurs when external forces—such as pressure gradients or fluid flow—drive movement, creating constantly changing conditions. The fact that a continuous flow is present evidences that concentration might not reach an equilibrium on both sides of the membrane. Furthermore, transport is influenced by molecular motion, solvent-solute interactions, diffusion, solvent drag, among other variables.

1.2.2.1 Molecular Motion

In pure water, solute molecules exhibit Brownian motion, moving relatively freely. However, within the biological extracellular space—which contains salts, proteins, ECM components, and cellular debris—the molecular motion of solutes is influenced by random collisions with these structures. These interactions affect the time required for molecules to reach biological membranes [57]. Solute molecules exhibit both translational and rotational motions, which are modulated by temperature and resistance arising from molecular interactions, ultimately impacting their diffusion rates across membranes [58].

Intracellular environments present even greater complexity, as cells are densely packed with proteins, nucleic acids, membranes, and other macromolecules. This molecular crowding, together with the solvent's viscosity and binding interactions to cellular structures, significantly hinders solute mobility [59].

1.2.2.2 Solute-Solvent Intermolecular Forces

The attractive interactions between a solute and the solvent involving it play an important role in determining the diffusion coefficient of the solute across a semipermeable barrier. When the attractive forces between solvent and solute molecules increase, the solute's diffusion coeffient decreases significantly because the solute tends to be "pulled" by the surrounding solvent molecules, which increases the effective friction experienced by the solute, thus slowing its movement [60].

In this regard, it's worth mentioning some types of non-covalent intermolecular interactions: van der Waals, ionic froces and hydrogen bonding. Van der Waals interactions are non-directional, weak since they do not result from chemical bonds, and depend on the distance and polarizability of interacting atoms or molecules—the closer and more polarizable, the stronger the attraction [57, 61]. In biological systems and aqueous environments, these forces are always attractive and significantly influence protein–protein interactions, adsorption to surfaces, and aggregation [62]. During solvation, van der Waals forces stabilize solute molecules by promoting solvent molecules to surround and interact with the solute. Notably, they play a key role in hydrophobic interactions, where non-polar solutes aggregate in water to minimize disruption of water's hydrogen-bonding network, an energetically unfavorable process [63]. Ionic bonds form via electron transfer between atoms, creating charged ions. In solution, ions modify hydrogen-bond dynamics of water by slowing rearrangement processes [64]. Charged solvent molecules interact specifically with anions and cations, forming ion pairing—a common occurrence— which affects solution behavior [65]. Finally, hydrogen bonding is a type of dipole-dipole intermolecular interaction in which a hydrogen atom covalently bonded to a highly electronegative atom (such as oxygen) interacts with a lone pair of electrons on another electronegative atom [66]. These interactions enable water molecules to strongly associate with solutes, surrounding them, and influencing their transport.

1.2.2.3 Solvent Drag and the Mass-Balance Concept

Solvent drag refers to the phenomenon whereby solute molecules experience a force due to the movement of solvent relative to a membrane. This process occurs not only as a result of bulk solvent flow, but also in the context of ion transport whose movement generates a driving force for water transport, which in turn exerts a dragging effect on solute molecules, facilitating their movement across the membrane. With this in mind one can understand that in non-equilibrium systems involving semipermeable barriers, osmotic forces may arise that can reverse the transport of filtered solute molecules. In such scenarios, the transport of these solutes back across the membrane occurs in conjunction with water molecules, further illustrating the coupled dynamics of solute and solvent movement under osmotic gradients [52].

The pressure effects on microfluidic systems introduce an additional variable to account for in molecular transport. For instance, significant pressure changes can cause a shift

from diffusion-dominated to convection-dominated solute motion, causing solvent to wash through the membrane while dragging fewer solute along with it [67].

While assessing this topic, another one arises—the mass-balance concept. It states that the quantity of mass within a system or compartment is determined by its initial mass, the rate of mass entering, and the rate of mass exiting. This principle applies broadly across liquids, gases, solutes, and solids, providing a fundamental framework for quantifying material flow and accumulation in physiological systems. [68]. In general terms, in steady state, the amount of mass entering a compartment over a given time equals the amount of mass leaving it during the same period. Bearing that in mind, the mass-balance concept inside a compartment (C) can be described by equation 1.5, considering a certain period in time.

$$\text{Mass}_C = \text{Mass}_{C,\text{initial}} + \text{Mass}_{C,\text{in}} - \text{Mass}_{C,\text{out}} \tag{1.5}$$

If this equation is not met, it means that what goes inside the compartment isn't the same as what comes out in the same period of time, meaning that the system is not in steady-state, and the amount of mass in the region will change until a new steady-state is reached. In inherently dynamic systems, such as neural signaling, a steady-state may never be established, requiring modified forms of the mass-balance framework to capture transient behaviors [69].

The versatility of this principle is evident across physiology. In respiratory systems, it underlies calculations of oxygen uptake and carbon dioxide elimination at the alveolar level. In the cardiovascular system, it connects cardiac output to tissue oxygen delivery and metabolic gas exchange. Within the renal system, the same framework quantifies solute filtration, reabsorption, secretion, and clearance [70].

1.2.3 Passive and Active Transport In Biological Systems

Passive and active transport processes can be observed throughout biological systems, often adapted to the specific needs of each tissue or organ. A prominent example of passive diffusion is the glomerular filtration barrier in the kidney. This highly specialized structure enables the movement of plasma from the bloodstream into the urine without the direct expenditure of metabolic energy. As shown in Figure 1.10, filtration occurs in the Bowman's capsule of a nephron, where solutes and water diffuse across the barrier, providing an essential step in urine formation.

During nutrient absorption in the intestines, small molecules such as water, oxygen, and certain nutrients also passively diffuse across the intestinal epithelial cells into the bloodstream [72, 73]. Even at the BBB, which restricts approximately 98% of therapeutics, small lipid-soluble molecules below 400 Da can cross via passive diffusion through the transcellular lipophilic pathway, as illustrated in Figure 1.11 [74]. Moreover, protein- and vesicle-mediated facilitated diffusion pathways are also present, as well as through the use of tight junctions.

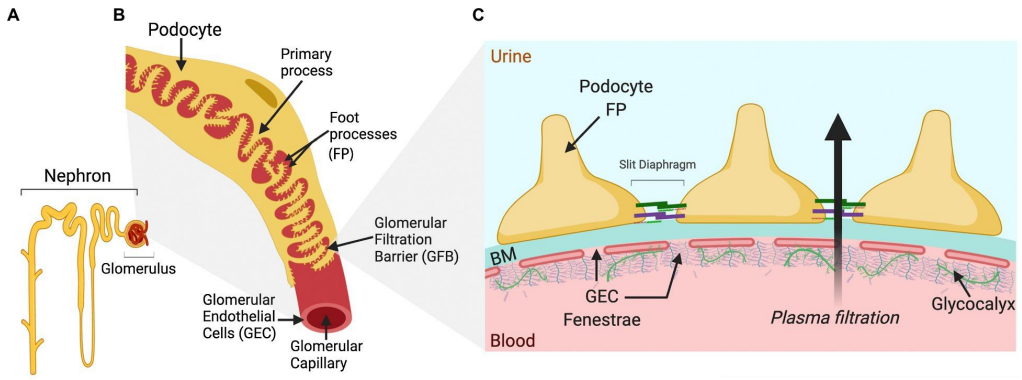

Figure 1.10: **Schematic drawing of a single nephron and glomerulus, a glomerular capillary vessel, and the glomerular filtration barrier (GFB). (A)** A nephron with its glomerulus. **(B)** the glomerular capillary, where glomerular endothelial cells (GEC) line the vessel and podocyte foot processes surround it. **(C)** a cross-section of the GFB, highlighting endothelial fenestrae, the basement membrane (BM), the glycocalyx layer, and podocyte foot processes linked by slit diaphragm proteins, which restrict albumin and direct plasma filtration into the nephron. Adapted from [71].

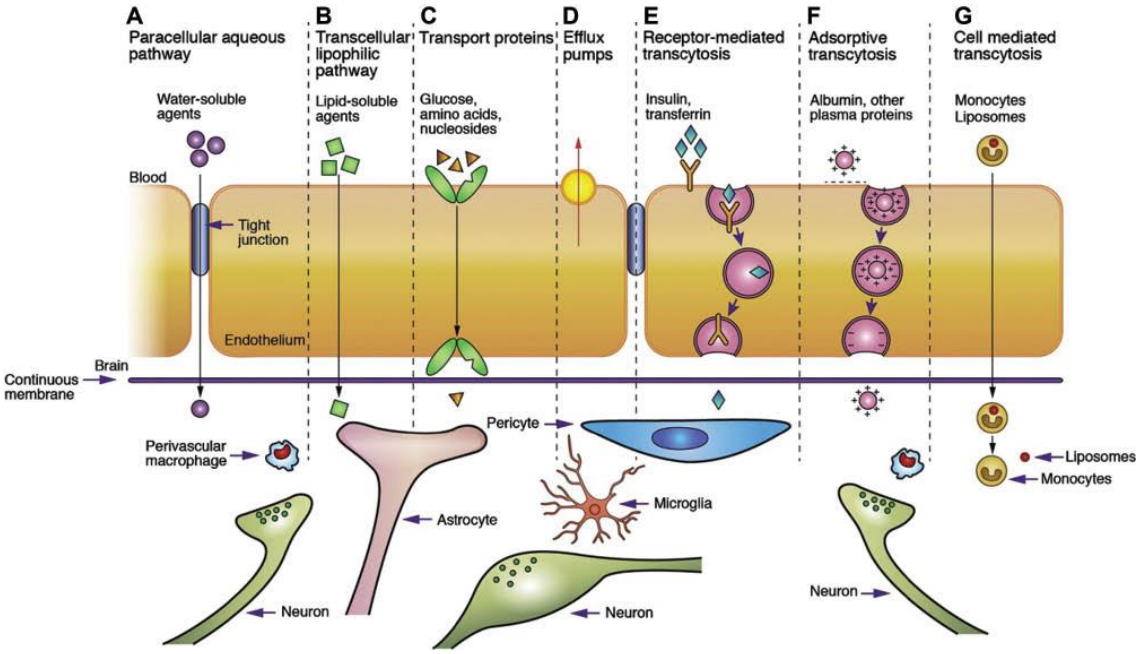

Figure 1.11: **Schematic representation of transport pathways across the BBB. (A)** Paracellular pathway. **(B)** Passive diffusion of lipid soluble molecules. **(C)** Carrier mediated transport. **(D)** Efflux pumps. **(E)** Receptor mediated transcytosis. **(F)** Adsorptive mediated transcytosis. **(G)** Cell mediated transcytosis. Adapted from [74].

However, most of the time passive transport in biological systems does not occur in isolation. It is frequently coupled with metabolic processes that consume energy in the form of ATP and mantain concentration gradients. Relevant examples include the sodium-potassium pumps located in the plasma membrane, which maintain the resting membrane potential and cellular ion balance [75]; hydrogen-ATPase pumps which transport hydrogen ions to acidify compartments like lysosomes, or create proton gradients used in processes

such as ATP synthesis; or the calcium pumps which actively transport calcium ions out of the cytoplasm to maintain low intracellular calcium levels, critical for cell signaling and muscle function [76]. Moreover, in Figure 1.11, efflux pumps are represented symbolizing the energy-dependent pathways caracteristic of active transport in the BBB.

A theoretical framework, combining passive diffusion and first-order metabolism in multi-compartment systems, showed how non-equilibrium conditions dynamically shape solute distributions over time [77]. This approach bridges physicochemical transport properties (e.g., lipophilicity, membrane permeability) with bioactivity patterns observed in complex tissues, offering predictive insights into drug distribution and cellular uptake in systems operating far from equilibrium. Beyond passive and pressure-driven mechanisms, in a foundational analysis, Guzmán-Lastra et al. [78] demonstrated that self-propelled particles organized into "active carpets" generate spontaneous, long-range flow fields, thereby enhancing non-equilibrium diffusion and significantly boosting molecular flux across membranes.

1.2.4 Non-Equilibrium Transport Simulations

To capture the complexity of non-equilibrium transport, non-equilibrium molecular dynamics (NEMD) simulations have become essential tools. These drive systems away from equilibrium and measure their response to perturbations, such as electric fields, thermal gradients, ATP hydrolysis, and the removal of ligands from their binding sites [79, 80]. By imposing controlled pressure and concentration gradients, NEMD simulations have revealed the molecular basis of transport through confined membranes and biological barriers. Those allow the computation of viscosity, diffusity, solvent drag, and coupled transport coefficients under realistic flow conditions [81]. These approaches have successfully informed reverse-osmosis models, revealing how pore size, free volume, and polymer chain mobility influence both water and solute flux [82].

Rankin and Huang [83] validated a novel NEMD algorithm to simulate concentration gradient-driven fluid transport through 2D membranes, where strong fluid–membrane interactions induced deviations from linear theoretical predictions. Similarly, boundary-driven NEMD simulations on polyamide and MXene nanochannels revealed that solvent permeance is more strongly governed by membrane–solvent friction than by pore size, and that pressure–flux relationships deviate in confined, high-viscosity environments [84].

Non-equilibrium thermodynamics in electrolytes relates diffusive fluxes to electrochemical potential gradients and osmotic pressure differences. Furthermore, advanced molecular kinetic modeling—including thermal fluctuations and thermoelectric coupling—has been applied to transport in confined fluids [85].

Collectively, these studies highlight that true non-equilibrium transport is governed not only by solute and solvent diffusion under gradients, as captured by traditional models [86, 87], but also by dynamic molecular interactions, fluctuating transport pathway, and interfacial friction. Realistic modeling demands multi-scale approaches that combine

macroscopic models (e.g. solution–diffusion phenomenology), mesoscopic insights (transient pore connectivity), and NEMD simulations to resolve friction-driven transport and kinetic coupling. Only through this integrative, dynamically-aware modeling framework can predictive, physiologically realistic OC and barrier systems be designed—especially when aiming to emulate organs' inherently non-equilibrium transport characteristics.

1.3 Overview of the Project

This work introduces a fully automated microfluidic perfusion platform engineered to enhance physiological relevance, operational stability, and analytical accuracy in investigations of molecular transport dynamics. The system provides precise, programmatic control and continuous monitoring of key physicochemical variables—such as pressure-driven flow, temperature, dissolved oxygen (DO) levels and fluid recirculation—all essential for recreating the concurrent mechanical and chemical forces that govern non-equilibrium transport across biological barriers.

The platform's capabilities were demonstrated through a proof-of-concept passive transport experiment employing bovine serum albumin (BSA) and fluorescein as tracer molecules. Under physiologically representative conditions mimicking glomerular filtration, the system enabled controlled, time-resolved quantification of solute flux across a semipermeable membrane. Notable design features include highly accurate pressure-based flow regulation, dual recirculation circuits equipped with failsafe volume sensors, unidirectional perfusion, automated programmable reagent delivery, synchronized multi-chamber sampling, and integrated sensors for real-time measurement of DO, flow rate, pressure, and temperature.

Through the integration of automated flow control and comprehensive sensing, the platform allows active manipulation and observation of the complex, time-dependent physicochemical environment underlying non-equilibrium molecular transport. This approach overcomes key limitations of current experimental models, ensuring reproducibility and deeper mechanistic insight. Ultimately, the system provides a powerful experimental tool for exploring the coupled transport mechanisms that sustain physiological homeostasis and drive barrier-associated pathologies.

1.4 Aims of the Project

This study was conducted within the framework of the European-funded initiative *Lifesaver* project, which aims to develop a microfluidic system for modeling placental function and predicting the transplacental transfer of drugs and environmental contaminants. The core of this system is a microfluidic perfusion platform designed to support OC models consisting of two independently pressure-driven circulation circuits separated by a cellular membrane [88]. The overarching goal of *Lifesaver* is to demonstrate the potential of advanced *in vitro* models to replace conventional testing methods, adressing both ethical

and scientific concerns and scientific limitations in drug development and chemical risk assessment, particularly under conditions of pathological placental dysfunction [89].

The specific objectives of this work included:

- Familiarization with handling of the microfluidic system hardware and software;
- Validation of platform performance with a proof-of-concept passive transport study using BSA and fluorescein as molecular tracers to demonstrate controlled, time-resolved quantification of molecular flux across a semipermeable nitrocellulose membrane under physiologically relevant conditions;
- UV-Vis and fluorescence spectroscopy analysis for molecular tracers detection;
- Data analysis and modulation of non-equilibrium molecular transport across the membrane system.

The work of this dissertation was carried out at the Institute for Research and Innovation in Health (i3S), in Porto.

1.5 Research Training and Outputs

- **Peer-reviewed Manuscript**

  Olivier Fournier, Miguel A. D. Neves, Théo Gavoille, Alan Morin, **Beatriz Pais**, Ivana Brenta, Justine Lereculey-Beaumanoir, Andrea Cruz, Denis Santos, Hugo Oliveira, Michael Gasik, Lisa D. Muiznieks, Inês Mendes Pinto. "Automated Microfluidic Platform for Molecular Transport Analysis Across Biomimetic Interfaces". *Advanced Sensor Research*. DOI: 10.1002/adsr.202500166. (*In Press*)

  A substantial part of this dissertation was adapted from the peer-reviewed manuscript referred above, co-authored by the candidate, which was already accepted for publication in the *Advanced Sensor Research* Journal, by Wiley (DOI: 10.1002/adsr.202500166). The text was adapted and all the work here described was carried out by the candidate, except where explicitly mentioned otherwise. In particular, the candidate's contribution to the scientific paper included the integration, testing and validation of the microfluidic platform and software, as well as conduction of molecular quantitative analysis using spectroscopic methods, mass balance data analysis and non-equilibrium transport modulation. The candidate also participated in the writing and editing of the draft and in the design of the figures present in the paper, whose manuscript can be found in appendix B.

- **Microfluidic Training, December 2024, in Paris**

  A training program at the Microfluidics Innovation Center (MIC), in Paris, was completed to gain expertise in microfluidic devices. It covered both theoretical principles

of microfluidics and practical skills for device handling and system operation. The candidate operated the system described throughout this dissertation prior to the formal commencement of the activities, acquiring hands-on experience to support subsequent research activities. This program at MIC was instrumental to train the candidate for microfluidic platform testing and proof-of-concept experimental validation described in this dissertation.

- **Lifesaver Annual Meeting, October 2025, in Brussels**

  The results described in this dissertation were presented at the last annual meeting of the Lifesaver Consortium, October 2025, in Brussels.

Declaration of Originality

The research work described in this dissertation was carried out in accordance with the norms established in the ethics code of Universidade Nova de Lisboa. The work described and the material presented in this dissertation, with the exceptions clearly indicated, constitute original work carried out by the author.

2

Materials and Methods

In this chapter are presented the methods for the microfluidic platform's modules fabrication, software development, chip fabrication, as well as the methods used in the integration, testing and validation of the platform and of the molecular transport assay that was conducted within the framework of the proposed work in this dissertation.

2.1 Microfluidic Hardware Components, Fabrication and Software

The fabrication and design of the microfluidic hardware components and programming of the dedicated software were developed by MIC. This section describes the methods and different materials used in that regard, which the candidate assembled, tested and used in her work.

The mechanical framework of the platform was modeled using Solidworks software. Most electronics were commercially sourced, including an OB1 MK4 four-channel pressure-driven flow controller (0-2000 mbar range; see Anex I.1), 12/1 MUX distribution unit, MUX Wire, 3/2-way valves, and MFS4 digital flow sensors (30-1000 µL/min range; Annex I.2) obtained from Elveflow (France). Custom level sensors were developed at the Microfluidics Innovation Center (France) by integrating Zisenisc ZCT-YOF07 capacitive elements (Farnell, France), while optical oxygen probes were acquired from Scientific Bioprocessing (Germany).

The system housing was fabricated using a fused deposition modeling 3D printer, Ultimaker S5 (Netherlands), employing both generic and tough polylactic acid (PLA). Fluidic connections between modules consisted of polytetrafluoroethylene (PTFE) tubing in two dimensions: outer diameter (OD) 1/16" and 1/32", and corresponding inner diameter (ID) 1/32" and 300 µm (Darwin Microfluidics, France). The pneumatic lines were constructed using polyurethane tubing (OD of 4 mm and ID of 2.5 mm; SMC, Japan). Interconnections between tubing and modules employed a range of fittings, including polyether ether ketone (PEEK) and perfluoroalkoxy (PFA) ¼"-28 male adaptors to 1/16" OD and 1/32" OD tubing connectors, ethylene tetrafluoroethylene (ETFE) ¼"-28 female to

Luer male connectors, polypropylene ¼"-28 swivel to barbed 3/32" ID connectors (Cluzeau Info Labo, France); as well as mini-Luer to 1/32" OD tubing tuck-in connectors and silicon sleeve tubing (Microfluidic ChipShop GmbH, Germany). All tubing connectors are evidenced in Annex I.4. Additional integrated elements included pressure caps (Elveflow, France), a heating unit (SADIJPR, China), and recirculation bridge modules (Microfluidics Innovation Center, France). System operation and user control were managed through custom software and a graphical interface developed in LabView (2022 Q3 release).

2.2 Microfluidic Chip Fabrication and Assembly

The microfluidic chip fabrication took place at the International Iberian Nanotechnology Laboratory, in Braga.

The chip was fabricated using a stereolithography 3D Printer (Form2 printer, FormLabs, USA) with BioMed Clear Resin (FormLabs). The design, created in AutoCAD comprised two identical open square chambers measuring 20 x 20 x 13 mm, corresponding to the top and bottom halves of the device. Each chamber incorporated a mini-Luer port on opposing sides, functioning as the respective fluidic inlet and outlet. Gaskets composed of ethylene propylene diene monomer (EPDM) rubber (1 mm thickness; Solutions Elastomeres, France) were cut to hold a semipermeable membrane between the two halves of the chip. Two squares (30 x 30 mm) were prepared to extend beyond the chip edges, and a central aperture of 15x15 mm was cut into each using an x-acto blade. A piece of nitrocellulose dialysis tubing membrane (25 x 25 mm; 10 kDa MWCO) was super-glued (Loctite) on both sides between the gaskets, and the assembly was flattened with a hard roller (Essdee) to ensure uniform contact. The resulting membrane-gasket composite (Fig. 2.1A) was subsequently positioned between the chip halves, and secured in place using a clamp (Fig. 2.1B, C). This assembly was performed by the candidate when conducting experiments using the microfluidic chip described. The two chambers of the chip were filled with phosphate buffered saline (PBS) (140 mM NaCl, 10 mM sodium/potassium phosphate, and 3 mM KCl, pH 7.4) by hand using a 10 mL syringe via tubing (300 μm ID) and mini-Luer connectors attached to the chip inlet.

2.3 Characterization of Microfluidic Modules

Individual functional tests of the microfluidic modules—including flow rate regulation, recirculation, injection, and collection—were carried out using two union connectors in place of the microfluidic chip (Fig. 2.2). System operation during these tests was manually managed through the Elveflow Smart Interface (ESI; Elveflow, France). Comprehensive characterization of the fully integrated platform was subsequently conducted using the assembled microfluidic chip in combination with custom control software, enabling automatic operation and synchronization of all components, which was performed in colaboration with MIC.

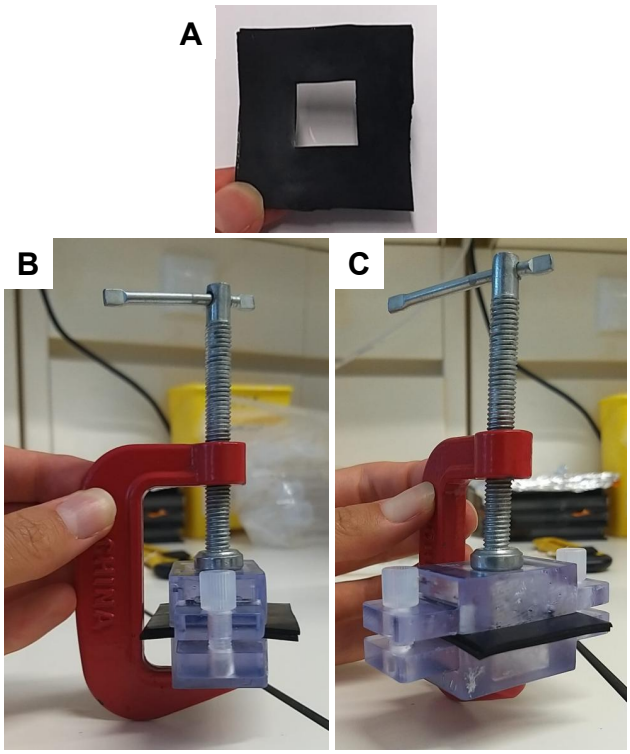

Figure 2.1: **Final chip assembly. (A)** Nitrocellulose membrane-gasket composite. **(B) and (C)** Final microfluidic chip assembly from two different perspectives.

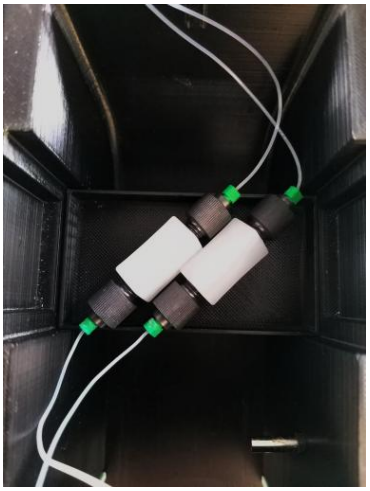

Figure 2.2: **Union connectors used in place of the microfluidic chip.** This configuration allowed individual testing of the microfluidic modules by applying pressures higher than those tolerable by a membrane.

2.4 Molecular Transport Assay

Transport experiments were carried out using fluorescein (Sigma Aldrich) as a low-molecular-weight tracer and BSA (Sigma Aldrich) as a model macromolecule, representative of abundant plasma albumin. The platform proof-of-concept assays were performed

with nitrocellulose dialysis tubing membranes with a 10 kDa MWCO (ThermoFisher Scientific), stored under humid conditions prior to use. The membrane was assembled in the microfluidic chip, and both chambers were filled with a 1×PBS buffer, as described above. Before chip integration, the entire fluidic system was filled with PBS. For each circuit, 70 mL of PBS were allocated between the two reservoirs (45 mL in R1, 25 mL in R2). During experiments, the chip was positioned vertically to align the membrane along the direction of transport. An aliquot for injection into circuit 1 (fluorescein and BSA; total volume of 1 mL) was prepared to result in a starting concentration after injection of 20 µg/mL fluorescein and 1 mg/mL BSA. The assembled chip was connected to the microfluidic platform and enclosed in a temperature-controlled chamber. Flow rates were set to 400 µL/min in circuit 1 and 200 µL/min in circuit 2 (400:200 ratio); or 400 µL/min in each circuit (400:400 ratio). Automated transport experiments were conducted in which one baseline and 19 subsequent samples (210 µL each) were collected from both circuits at 10-minute intervals. Fluorescein concentrations in the collected samples were quantified via fluorescence spectroscopy (excitation/emission: 485/528 nm), whereas BSA transport was determined by ultraviolet (UV) absorbance at 280 nm using a Synergy 2 HTX multi-mode microplate reader (BioTek). Transport analysis was performed according to integral-mass balance principles based on mass and flow conservation [90], under the assumption that neither the carrier medium (PBS) nor the tracer compounds (BSA and fluorescein) were subject to external sources or sinks. Under continuous-flow conditions with fixed tracer concentrations in the reservoirs of circuit 1, a system of differential equations [90] was established to balance the sum of inlet and outlet flows and the corresponding tracer mass fluxes. At steady state, net solute accumulation within the membrane and circuit compartments was assumed to be negligible, such that the time derivatives of tracer concentrations approached zero. Computational fluid dynamics (CFD) simulations were conducted in COMSOL Multiphysics to model the fluid pathways within the chip and assess the distribution of fluorescein, in case flux currents did not effectively reach the entire chamber volume, thus hindering the transport of fluorescein across the nitrocellulose membrane. Mass balance and CFD simulation analyses were performed in partnership with Seqvera (Finland).

2.4.1 UV-Vis Spectroscopy

Spectroscopy is a technique used to analyze how matter absorbs, emits, or interacts with electromagnetic radiation. The method varies depending on the specific range of wavelengths being examined. UV-Vis spectroscopy focuses on the UV and visible portions of the electromagnetic spectrum (from 190 to 800 nm). When electromagnetic radiation interacts with matter, various phenomena can take place, such as reflection, scattering, absorption, fluorescence or phosphorescence (where energy is absorbed and then re-emitted), and photochemical reactions involving absorption followed by bond breaking. This technique is particularly useful for qualitative and quantitative analysis,

allowing for identification and confirmation of molecules in a sample, determination of compound concentrations in solution, and monitoring of reaction kinetics and molecular interactions [91].

2.4.1.1 UV Absorbance

In a typical UV analysis, which spans from 190 to 400 nm, a spectrophotometer directs ultraviolet light through a sample and measures the amount of light absorbed at a given wavelength. The absorbance corresponds to the difference between the incident radiation (I_0) and the transmitted radiation (I) passing through the sample [91]. Therefore, absorbance is calculated as shown in equation 2.1.

$$A = -\log(T), \tag{2.1}$$

where T is the transmittance, defined in equation 2.2 as the ratio of transmitted to incident light.

$$T = \frac{I}{I_0} \tag{2.2}$$

2.4.1.2 Fluorescence Spectroscopy

In fluorescence spectroscopy, a sample is exposed to monochromatic light with an energy that can be absorbed by the sample's molecules. This absorption excites the molecules from their ground state to a higher electronic state. As the molecules return to the ground state, they release excess energy in the form of emitted photons, producing fluorescence [92].

One of the most important applications of absorbance and fluorescence spectroscopy is the determination of the concentration of an unknown sample. To do so, the relationship between the concentration of a sample and its absorbance/fluorescence signal intensity as to be assessed.

2.4.1.3 Synergy™ 2 Multi-Mode Microplate Reader (BioTek)

The BioTek Synergy 2, showed in Figure 2.3, is a flexible multi-mode microplate reader used in research and diagnostics, supporting detection modes such as UV-Vis absorbance, fluorescence, fluorescence polarization, time-resolved fluorescence, and luminescence [93].

For absorbance readings, Synergy 2 uses a super-quiet xenon flash lamp as light source. The light passes through a monochromator, which selects a specific wavelength between 200 and 999 nm (in 1-nm increments). The selected light then travels through the sample in the microplate well. A photodiode detector measures the intensity of light that passes through the sample [93]. The system calculates absorbance based on the difference between the incident and transmitted light, typically following the Beer-Lambert law, represented in equation 2.3, which depicts the same rationale of equation 2.1.

$$A = \varepsilon l C = -\log\left(\frac{I}{I_0}\right), \tag{2.3}$$

where ε is the molar absorption coefficient, l is the path lenght, and C is the concentration of the compound in solution.

In fluorescence mode, Synergy 2 uses either a tungsten-halogen lamp or a xenon flash lamp (depending on the fluorescence module in use). The system employs excitation and emission filters along with dichroic mirrors to direct and select specific wavelengths of light. A photomultiplier tube (PMT) detects the emitted fluorescence from the sample [93].

Figure 2.3: **Synergy™ 2 Multi-Mode Microplate Reader (BioTek)** used for experimental assays, with the microplate carrier open.

2.4.2 Calibration Curves Development

In order to quantify the concentrations of BSA and fluorescein from their respective absorbance and fluorescence measurements, two separate calibration curves were developed to identify the linear detection range of the Synergy 2 microplate reader. Performing quantification within this linear range ensures accurate determination of sample concentrations.

For the fluorescence calibration curve, the linear range was established from 0.00033 to 3 μg/mL. A series of fluorescein dilutions were prepared at the following concentrations: 0.00033, 0.0033, 0.0166, 0.08, 0.25, 0.5, 1 and 3 μg/mL in PBS. Fluorescence readings were performed using a black 384-Well Flat-Bottom Microplate (Corning), with each concentration aliquoted in triplicate at 25 μL per well.

For the absorbance calibration curve, BSA standard solutions were prepared at concentrations of 0.01, 0.1, 0.5, 1, 10 and 25 mg/mL in PBS. Absorbance measurements were carried out using a clear 96-well F-bottom Microplate (Greiner), with each concentration aliquoted in triplicate at 70 μL per well.

Fluorescence and absorbance measurements from the unknown samples were then interpreted using the respective calibration curves. Fluorescence intensity values were

plotted against known fluorescein concentrations, and absorbance values were plotted against BSA concentrations, as shown in Figure 2.4.

Each dataset was fit with a linear regression model within the validated linear range of Synergy 2. The resulting calibration equations are presented in equations 2.4 and 2.5, along with the respective standard errors.

$$\text{Fluorescence} = (5664 \pm 74) \cdot [\text{Fluorescein}]\ (\mu\text{g mL}^{-1}) + (94 \pm 93) \tag{2.4}$$

$$\text{Absorbance} = (0.078 \pm 0.002) \cdot [\text{BSA}]\ (\text{mg mL}^{-1}) + (0.01 \pm 0.02) \tag{2.5}$$

Using these equations, the concentrations of fluorescein and BSA in the experimental samples were calculated by inputting the measured fluorescence or absorbance values and solving for the unknown concentration.

When the compound's concentration used for an experiment was higher than the maximum concentration value in its calibration curve, a dilution step was performed in order to fit that concentration within the linear range of the calibration.

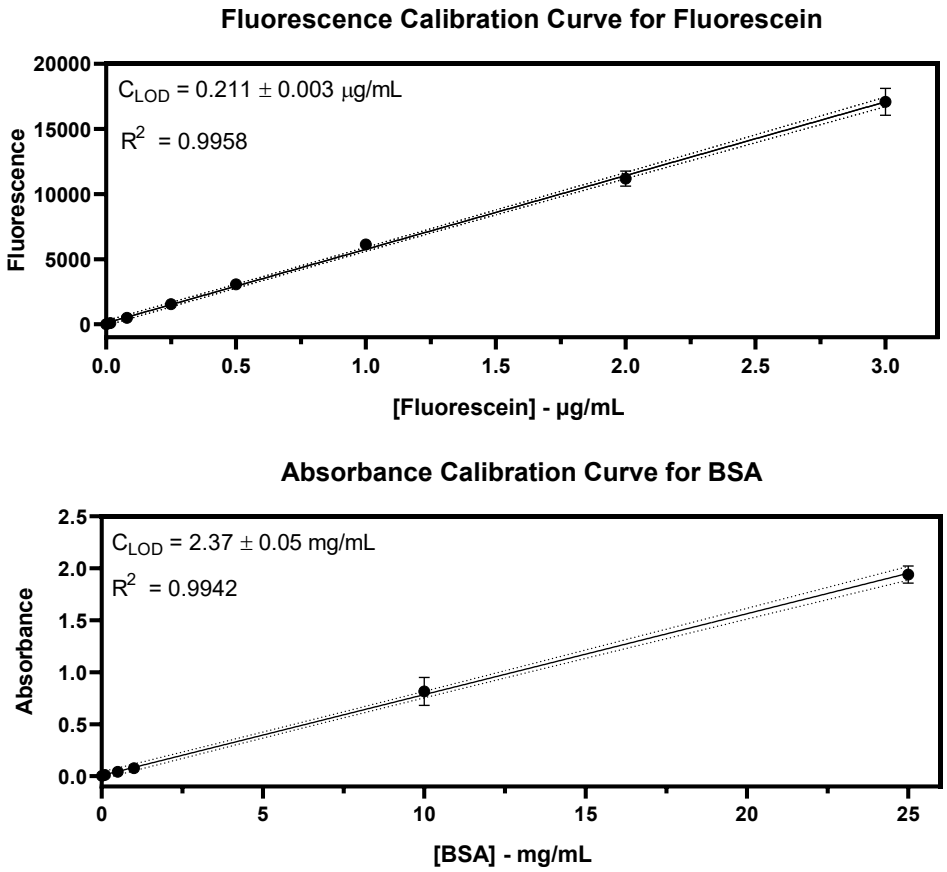

Figure 2.4: **Mean fluorescence (top) and absorbance (bottom) measurements for spiked concentrations of fluorescein and BSA**. Data presented as mean ± SD (n = 3) with 95% confidence intervals included. C_{LOD} respects to the Concentration Limit of Detection.

2.5 Statistical Analysis

GraphPad Prism 8 (GraphPad Software) was used for graphic development and statistical analysis. Statistical significance was determined using an unpaired Student's two-sample t-test for equal means, with p-values indicated accordingly. Differences between groups were considered statistically significant when $p < 0.05$. This test evaluates whether the means of two unrelated samples differ sufficiently to reject the null hypothesis of equality. The degree of difference is quantified by the p-value, with smaller p-values indicating stronger evidence of a true difference between groups [94].

3

Results

3.1 Design of an Automated Microfluidic Platform for Molecular Transport Assays

In this section, the candidate contributed for the testing and validation of the integrated microfluidic platform and for the testing of the dedicated software, in collaboration with MIC.

This study reports the design, development, and proof-of-concept validation of a modular microfluidic perfusion platform capable of automating transport assays—that is, experiments assessing compound translocation across a semipermeable membrane mimicking a biological barrier. The platform was conceived to promote both methodological and technological standardization while enabling automation, all without compromising versatility. Its architecture supports broad compatibility with diverse microfluidic chip geometries, membrane compositions, and cellular models, ensuring adaptability across multiple research and application contexts.

The central architecture of the platform consisted of two distinct fluidic pathways (circuit 1 and circuit 2) independently regulated by a primary fluidic control unit (Figs. 3.1A, B). These circuits were interfaced on opposite sides of a biomimetic barrier-integrated microfluidic chip positioned within a temperature-controlled chamber. This configuration fulfills the essential criteria for evaluating both the impact of tracer compounds on a biomimetic membrane and their transmembrane transport behavior. The platform incorporated a suite of modular components that enabled independent liquid recirculation in each circuit, automated compound injection and mixing within circuit 1, and time-resolved sample collection from both circuits1 and 2 (Figs. 3.1C-E). Instruments were color-coded to distinguish between the two fluidic pathways, thereby simplifying assembly, calibration, and operation. Continuous in-flow measurement of DO was implemented in each circuit. A thermal chamber was constructed to regulate the temperature of the molecular transport zone ranging from ambient temperature to 50°C, thus providing the option for co-culture of cells on a membrane in the microfluidic chip, thereby expanding the system's functionality for biologically integrated transport studies.

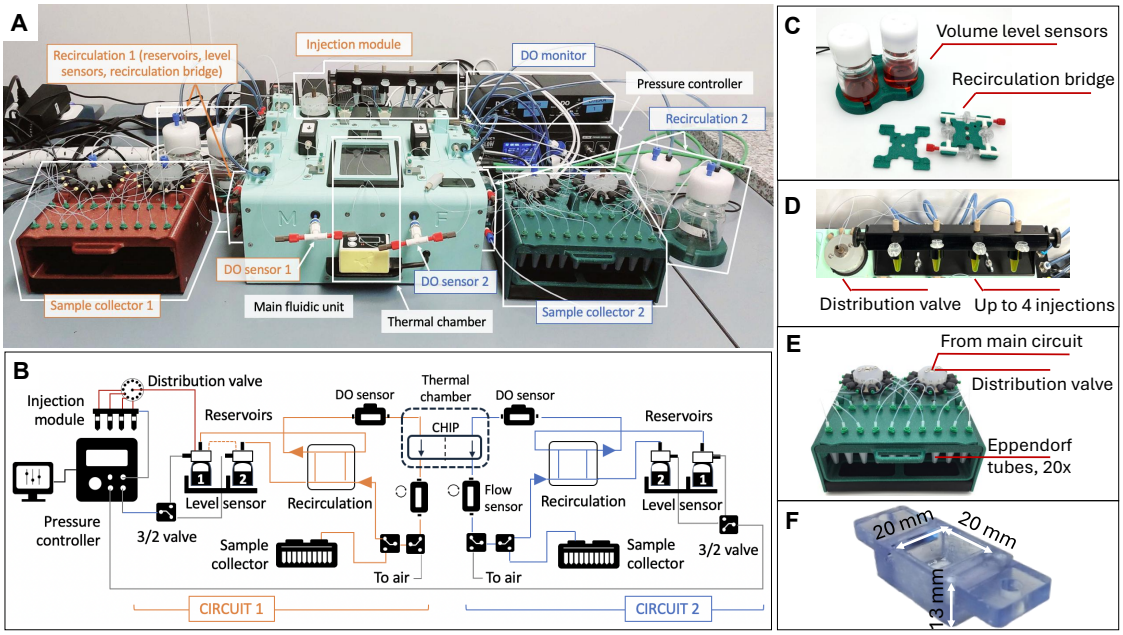

Figure 3.1: **Microfluidic platform for automated molecular transport assays. (A)** Complete view of the microfluidic platform, comprising different integrated modules (dark red: circuit 1, dark green: circuit 2, light blue: main fluidic unit). **(B)** Fluidic pathway schematic for both circuits (orange: circuit 1; blue: circuit 2). **(C)** Sensorized recirculation modules featuring flask holders with integrated volume-level sensors and unidirectional recirculation bridges. Detailed operating principle shown in Figure 3.3. **(D)** Injection module equipped with four Eppendorf tube holders and a multiplexed rotary distribution valve. Operating principle detailed in Figure 3.4. **(E)** Automated sample collection module supporting up to 20 sequential samples. **(F)** Schematic of one half of the chip.

Fluid flow was regulated using a pressure-driven flow controller (OB1 MK4, Elveflow) and two inline thermal flow sensors coupled to separate Proportional-Integral-Derivative (PID)[5] feedback loops for automated real-time regulation of flow rate. To ensure operational flexibility and independence from specific flow rates or perfusion durations, each circuit incorporated a dual-reservoir recirculation system (100 mL Schott bottles). During operation, one reservoir was actively pressurized to drive the flow, while the second served as the collection reservoir; their functions alternated automatically before the active reservoir was depleted. The recirculating fluid pathway of each circuit was directed through an array of 3/2-way valves configured to enable automated and independent switching between reservoirs (Fig. 3.1B). Custom 'failsafe' volume-level sensors were embedded within the system to signal the control unit when the active reservoir approached minimal volume, triggering automatic valve actuation to pressurize the replenished reservoir (Figs. 3.1B, C). To maintain unidirectional flow across the microfluidic chip, each circuit employed a recirculation bridge composed of four check valves and four T-junctions arranged in a square configuration.

A distribution valve was integrated into the system to enable automated, sequential

[5]Feedback-based control loop mechanism that automatically adjusts processes. It compares the target value with the actual value of the system and applies corrective actions to minimize the error between them.

injection of up to four distinct test compounds into reservoir 1 of circuit 1 (Figs. 3.1B, D). The injection rack was designed to accommodate standard Eppendorf tubes, allowing for flexible dosing volumes between 10 and 1500 µL. To support automated, time-resolved sampling, two dedicated sample modules were developed and installed inline, immediately downstream of the microfluidic chip. Each sample collector was equiped with two distribution valves, and contained a removable rack for up to 20 Eppendorf-sized tubes aligned under a snap-shut lid fitted with fluidic tubing connection ports for secure and sterile operation (Fig. 3.1E).

The platform architecture was engineered for broad compatibility with a variety of commercial and custom-fabricated membrane-integrated microfluidic chips, all housed within a temperature-controlled chamber. In the present study, the chip consisted of two identical rectangular chambers equipped with mini-Luer ports to facilitate fluidic connection to the microfluidic tubing (Fig. 3.1F).

Regarding the software system, which runs fully automatically, it responds according to the fluxogram in Figure 3.2B. An image of the user interface is represented in Figure 3.2A.

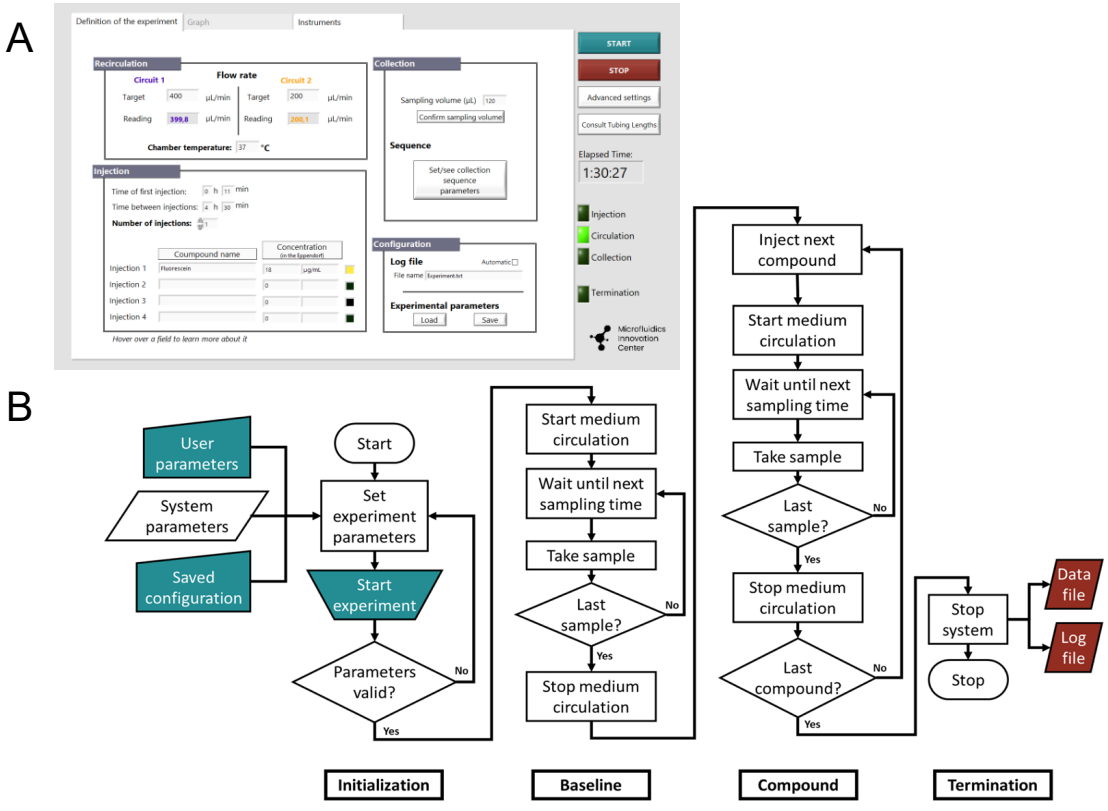

Figure 3.2: **Control software interface and operational workflow. (A)** Overview of user-configurable parameters within the "Definition of the experiment" interface tab. **(B)** Flowchart of the automated transport assay workflow. User inputs (blue shapes) and system outputs (red shapes) are indicated. The diagram illustrates the four principal experimental phases: system initialization, baseline data acquisition, compound injection and monitoring, and experiment termination. Software development was performed by MIC.

3.2 Characterization of Module Stability and Accuracy

In this section, the candidate contributed for the validation of each module's stability and accuracy by conducting data treatment and analysis of the different tests that were conducted in the microfluidic platform. The results in this section were accomplished in collaboration with MIC.

To maintain unidirectional flow through the microfluidic chip while employing pressure-driven control, a recirculation bridge was engineered and integrated inline upstream of the chip in each circuit. The flow direction within this bridge was determined by the orientation of two parallel pairs of check valves, which permitted fluid movement in only one direction (Fig. 3.3A). Opposite corners of the bridge were connected to the two liquid reservoirs, while the remaining corners were linked to the inlet and outlet of the microfluidic chip (Fig. 3.1B). At each T-junction allowing two potential flow routes, liquid preferentially passed through the check valve offering the lowest back pressure. This arrangement yielded two possible recirculation pathways within the bridge, corresponding to which reservoir (R1 or R2) was actively pressurized. Importantly, liquid flow from the bridge towards the chip was independent of reservoir origin, meaning that liquid exited the bridge from a single corner, regardless of which reservoir was pressurized (top left outlet in Figure 3.3A). Similarly, flow returning from the chip always re-entered the bridge at a single entrance (bottom right inlet in Figure 3.3A).

The fluid control modules exhibited consistent performance across all tested conditions, demonstrating stable flow regulation, reliable recirculation, and operational flexibility. The integrated pressure-driven flow controller, thermal flow sensors, volume-level sensors, and recirculation bridge were jointly employed to regulate two independent flow circuits over a continuous 4.5-hour operation (Figs. 3.3B-D). In both circuits, the flow remained steady and tightly maintained at the specified target rates. Normalized histograms of the recorded flow rates (1 Hz acquisition frequency) were generated for two flow rate configurations: 400:400 ratio (400 µL/min in both circuits; Fig. 3.3B) and 400:200 ratio (400 µL/min and 200 µL/min in circuits 1 and 2 respectively; Fig. 3.3C). Stabilized flow rates were measured at 400.0 ± 0.5 µL/min and 200.0 ± 0.4 µL/min (for 400:200 ratio), and 400.0 ± 1.1 µL/min and 400.0 ± 1.3 µL/min (for 400:400 ratio). The integrated level sensors successfully enabled alternating pressurization between the two reservoirs in each circuit. When a minimal liquid level was detected in the active reservoir, the control software automatically triggered the valve system to pressurize the replenished reservoir (Fig. 3.3D). Each reservoir switch produced a brief, expected drop in flow to near zero, followed by a transient overshoot corresponding to the PID feedback mechanism restoring the flow to its target rate. The intervals between successive switching events remained consistent—approximately 105 min at 200 µL/min and 50 min at 400 µL/min—verifying proper level-sensor function (Fig. 3.3D). Slight variations in the duration of the initial pressurization cycle relative to subsequent ones were attributed to the initial manual partitioning of liquid between the two reservoirs.

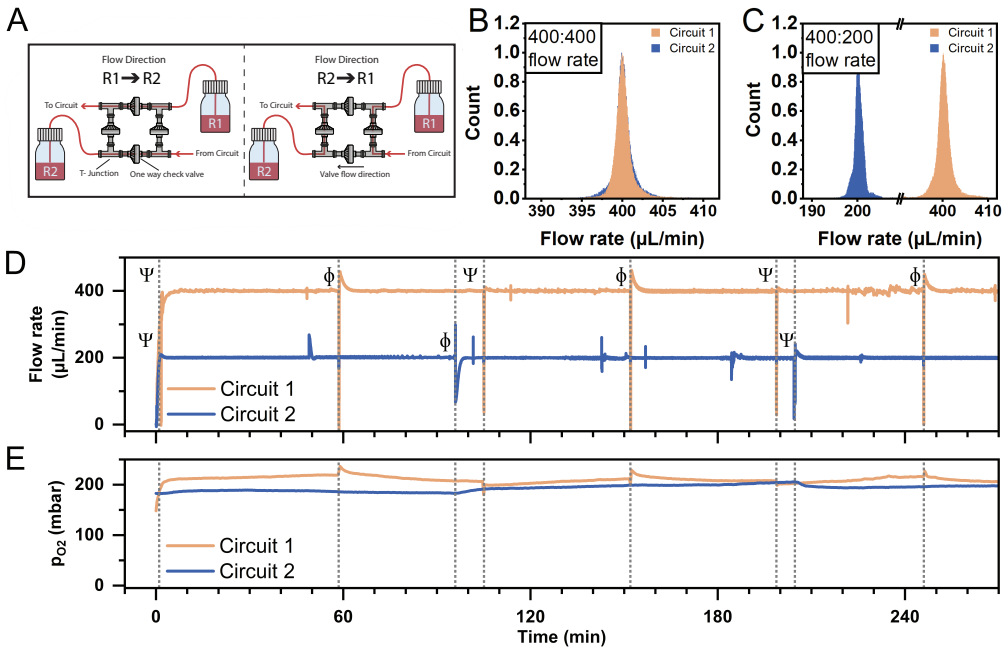

Figure 3.3: **Flow control and monitoring system performance. (A)** Recirculation bridge configuration enabling two flow pathways. Liquid flows from R1 or R2 depending on active pressurization, maintaining unidirectional flow to the circuit (top-left exit) and return from the circuit (bottom-right entrance). **(B)** Normalized flow rate histograms using ESI software at 400 µL/min in both circuits (circuit 1, orange; circuit 2, blue). **(C)** Normalized flow rate histograms using ESI software at 400 µL/min in circuit 1 and 200 µL/min in circuit 2. **(D)** Temporal flow rate profile using ESI software (400 µL/min in circuit 1 and 200 µL/min in circuit 2). Alternating reservoir pressurization events are indicated: R1 (Ψ) or R2 (Φ). **(E)** Temporal oxygen partial pressure profile using ESI software (400 µL/min in circuit 1 and 200 µL/min in circuit 2).

The evolution of the oxygen partial pressure (pO_2) was monitored in both circuits throughout the 4.5-hour experiment (Fig. 3.3E), in synchronization with the recorded flow rates (Fig. 3.3D). Oxygen levels remained steady within the range of 180 to 220 mbar for the entire duration of the experiment. Minor, gradual fluctuations in pO_2 were observed in both circuits, corresponding to the alternating pressurization of reservoirs R1 and R2, indicated by the symbols Ψ and Φ, respectively (Fig. 3.3D).

An essential parameterization step in automating a microfluidic transport assay involves the controlled introduction of a test compound into one of the flow circuits. The microfluidic platform was configured to enable up to four automated compound injections per experiment. The injection sequence was programmed to deliver the compound into R1 of circuit 1, initiate mixing between the two reservoirs off-line from the main flow path, and subsequently reconnect the mixture to the complete circuit and the microfluidic chip (Figs. 3.1B, 3.4A). Prior to each injection, the liquid contained in R1 was first transfered to R2. The compound was then injected into R1 (Fig. 3.4A, i), after which the contents of R1 and R2 were circulated bidirectionally at a high flow rate (2000 µL/min) to achieve

complete homogenization (Fig. 3.4A, ii).

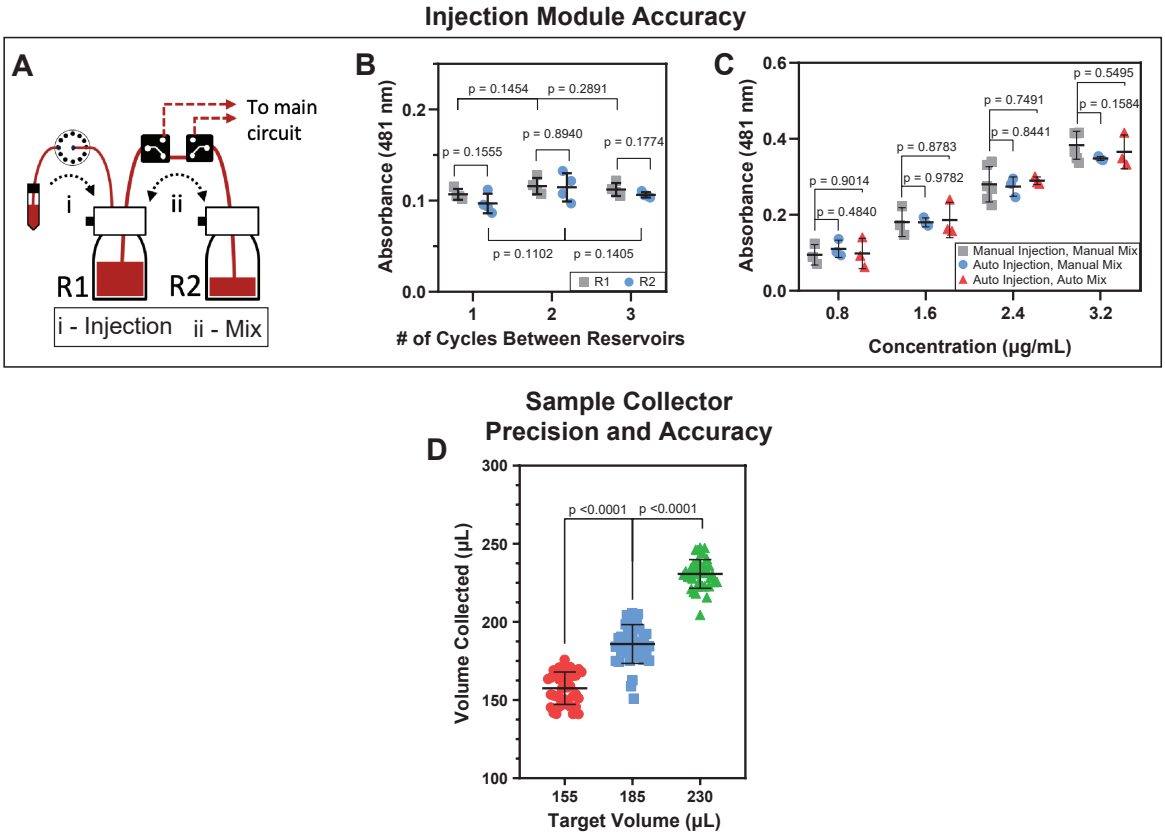

Figure 3.4: **Performance of injection and collection modules. (A)** working principle of injection module: i) The compound is injected into R1 of circuit 1. ii) The medium and the compound are circulated between R1 and R2 until homogenized. **(B)** Mixing efficiency of injected compound in R1 (grey squares) and R2 (blue circles) as a function of the number of back-and-forth cycles. **(C)** Platform versatility for sequential injections: absorbance (mean ± SD, n=3-5) in R1 for four successive fluorescein injections via manual injection and shaking (grey squares), automated injection with subsequent manual shaking (blue circles), or automated injection and three automated mixing cycles (red triangles). **(D)** Accuracy of automated sample-collection volumes for three independent targeted sample sizes (155 µL, 185 µL, 220 µL; n=40 per condition).

A series of validation tests were conducted to evaluate the efficiency of compound homogenization following successive cycles of automated back-and-forth mixing, using fluorescein dissolved in PBS as the model tracer. Rapid and uniform mixing of fluorescein with buffer was achieved in reservoirs R1 and R2 of circuit 1 after a single mixing cycle, as evidenced by equivalent absorbance values in both reservoirs (Fig. 3.4B). The performance of the automated injection and mixing procedures was further compared with manual injection followed by manual shaking. Four sequential injections of fluorescein were performed under identical conditions, and absorbance values in R1 were recorded after each injection (Fig. 3.4C). The results demonstrated comparable absorbance responses between automated and manual methods, with signal intensity increasing linearly across successive injections. These findings confirm the precision and reproducibility of the automated injection and mixing functions implemented within the platform.

Two automated sample modules were integrated into the platform, allowing operator-defined control of sampling intervals and collection volumes from both flow circuits. The precision and flexibility of the collection system were evaluated through fully automated experiments targeting three different sample volumes. Prior to and following each collection event, tubes were weighed, and the corresponding sample volume was calculated from the measured mass using the density of PBS at 20°C (1.005584 g/mL; [95]). cross all tests, the measured sample volumes deviated by less than 1.5% from their respective target values (157 ± 10 µL, target 155 µL; 185 ± 12 µL, target 185 µL; 231 ± 9 µL, target 230 µL; mean ± SD, n=40 in each condition) confirming the high precision of the automated collection process (Fig. 3.4D).

3.3 Proof-of-Concept: Automated Microfluidic System for Analyzing Transport Dynamics Across a Semipermeable Barrier

All results reported in this section derive exclusively from the candidate's own work.

A proof-of-concept transport assay was conducted to validate platform's capacity to monitor tracer movement across a semipermeable barrier. The experiments were designed to simulate passive diffusion processes occurring across physiological interfaces such as the GFB, employing a nitrocellulose dialysis membrane with a 10 kDa MWCO. In addition, the assay served to assess the synchronization of compound injection and sample collection with integrated flow rate and fluid recirculation control (Fig. 3.6). Two flow-rate configurations were investigated: 400:400 µL/min and 400:200 µL/min for circuit 1 and circuit 2, respectively. The injected solution consisted of a mixture containing BSA (66 kDa) and fluorescein (0.33 kDa). Based on their molecular sizes, fluorescein was expected to permeate the membrane from circuit 1 to circuit 2 (Fig. 3.5), while BSA was anticipated to remain retained, thereby establishing an osmotic gradient in the reverse direction, from circuit 2 toward circuit 1.

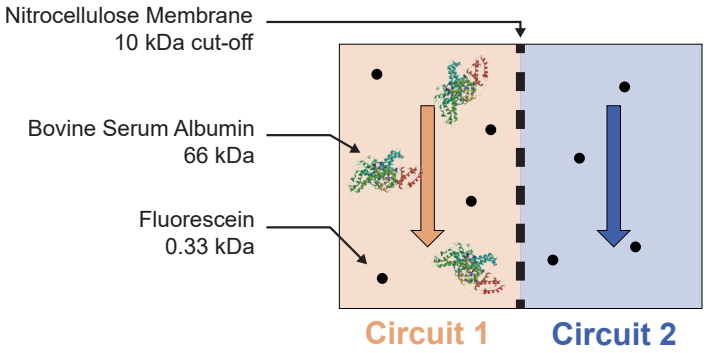

Figure 3.5: **Schematic of flow directionality inside the chip.** BSA is unable to cross the nitrocellulose membrane, but fluorescein is a much smaller molecule, therefore being permeable to the barrier.

The recorded flow rates (Figs. 3.6A, E), reservoir pressures (Figs. 3.6B, F), and event sequence (compound injection and sample collection; Figs. 3.6C, G) were synchronized throughout a 4.5-hour experiment comprising a single compound injection into circuit 1 and 20 sample collections from each circuit. Following a 10-minute recirculation period, a baseline sample was collected from both circuits. Immediately thereafter (t = 11 min), the test solution containing fluorescein and BSA (final concentrations: 20 µg/mL fluorescein and 1 mg/mL BSA) was injected into circuit 1, after which the system resumed recirculation with the loaded medium. The 38 subsequent samples (19 per circuit) were collected at 10-minute intervals. During each collection event, flow in both circuits was independently regulated to prime the collection lines, withdraw the designated sample volume, and purge residual fluid. These operations produced transient fluctuations in pressure and flow rate, detectable as rapid oscillations. Following each sampling event, the PID algorithm quickly restored the target flow rates in both circuits, maintaining stable operation until the next collection. It is worth noting that sampling events momentarily disturbed flow stability, generating brief decaying pressure oscillations (Figs. 3.6A, B and E, F). However, given the relatively long intervals between samples, these perturbations did not meaningfully alter the shear rate along the membrane surface—as corroborated by CFD modelling (data not shown)—nor did they significantly influence the cumulative transport kinetics of either compound.

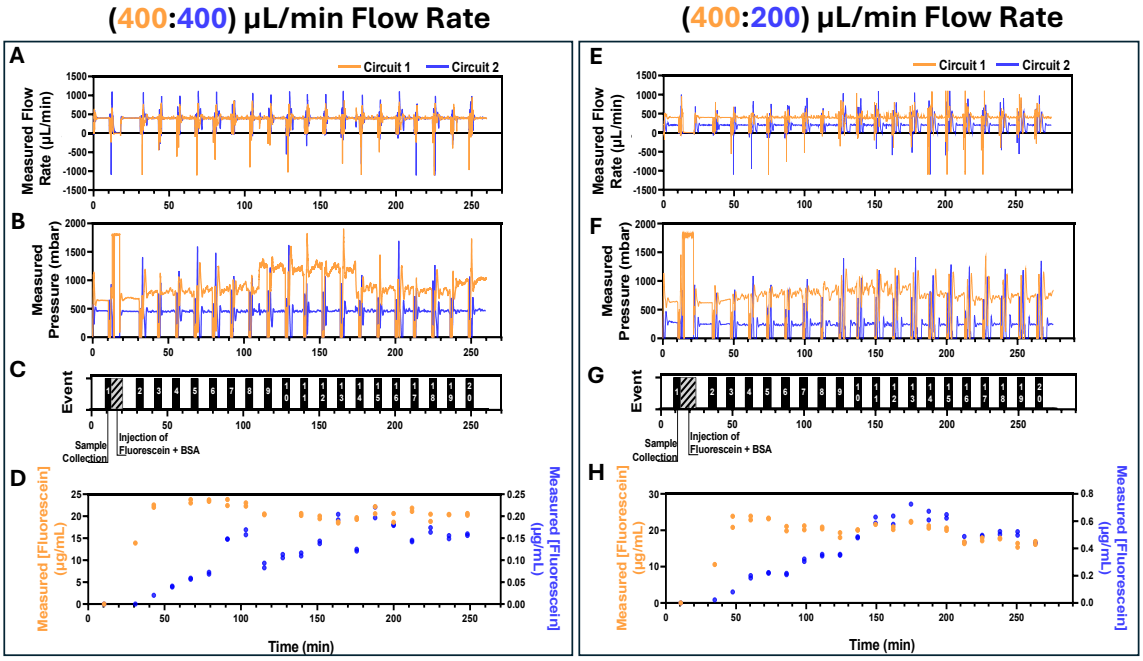

Figure 3.6: **Analysis of molecular transport in a non-equilibrium system under different flow rates.** Demonstration of full platform performance and proof-of-concept of its automation for molecular transport dynamics across a semipermeable barrier at **(A-D)** (400:400) µL/min and **(E-H)** (400:200) µL/min flow rate ratios. Synchronized measured flow rate, pressure, timing of injection and sample collection, and measured fluorescein concentration in circuit 1 and circuit 2 at different flow rates.

The concentration of BSA and fluorescein in each of the 20 collected samples were quantified by UV-Vis and fluorescence spectroscopy, respectively (Figs. 3.6D, H). For both tested flow rate configurations, fluorescein concentrations in circuit 1 gradually decreased over time, while those in circuit 2 increased, reflecting directional transmembrane transport. However, the measured values suggest that fluorescein concentration decreased more rapidly in circuit 1 than it increased in circuit 2. This behavior aligns with the fundamental principles of non-equilibrium passive transport, wherein solute movement across a semipermeable barrier is governed by a combination of factors—such as osmotic pressure, solvent drag, and electrostatic interactions—rather than solely by concentration-driven diffusion (Fig. 3.7).

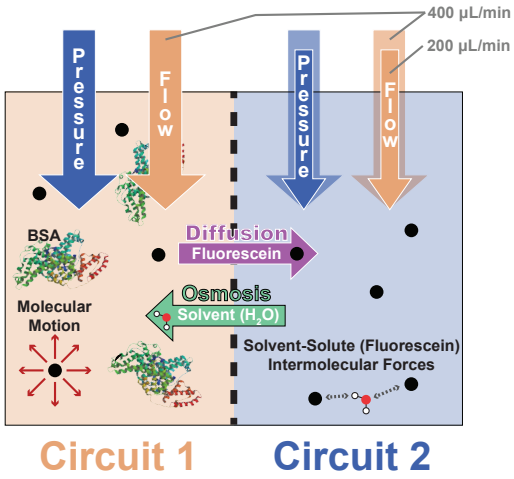

Figure 3.7: **Diagram depicting the different forces affecting the passive transport of fluorescein from circuit 1 to circuit 2.** Passive diffusion, molecular motion, solvent-solute intermolecular forces and osmosis causing solvent drag.

This behavior is consistent with thermodynamic principles, whereby differences in chemical potential between the two fluid compartments drive both the transmembrane transport of the permeable tracer and an opposing osmotic solvent flow. The latter effect is further influenced by fluctuations in pressure and flow rate within the system. Consequently, an accurate determination of the overall transport rate across the membrane requires accounting for the net mass transfer in both directions.

Since CFD evidenced full turn-over of molecules going in and out of the microfluidic chip, the principle of integral mass balance [90] was possible to be employed, in order to precisely characterize the kinetics of fluorescein transport (Fig. 3.8). Analysis of transport kinetics demonstrated that fluorescein accumulation in circuit 2 was significantly higher at a flow rate ratio of 400:200 µL/min compared to 400:400 µL/min, suggesting that the reduced flow rate in circuit 2 relative to circuit 1 increased residence time and favorable transport forces, thereby promoting more efficient transport. Additional data on the rate of changing fluorescein concentration in time in circuit 2 are available in Appendix A, further supporting the consistency of the transport kinetics observed in Figure 3.8.

It is worth noting that no BSA was detected in circuit 2, suggesting that, as expected,

BSA did not cross the membrane (Fig. 3.9).

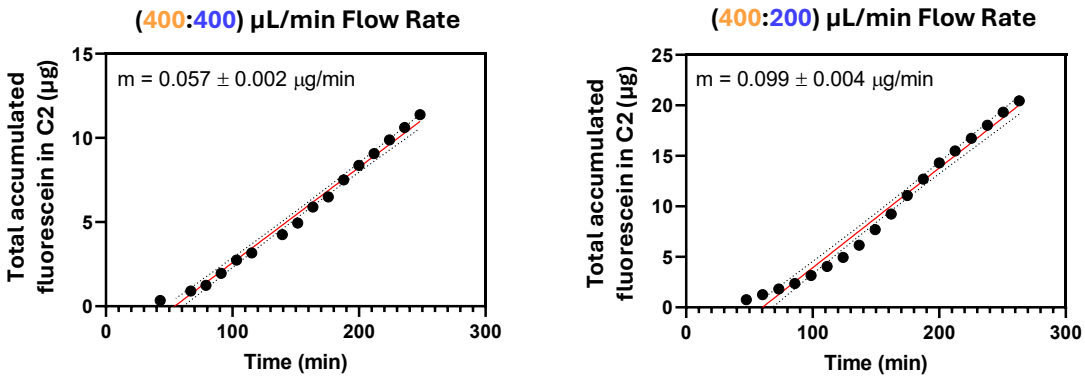

Figure 3.8: **Fluorescein transport rates from circuit 1 to circuit 2 (C2) calculated from the flow rate and fluorescein concentration data in Figure 3.6.** Total fluorescein transport from circuit 1 into circuit 2 over time at the different flow rates evaluated. 95% confidence intervals are indicated.

The observed selective passage of small solutes demonstrates that the microfluidic platform supports controlled, size-dependent, and flow-sensitive molecular transport, validating its utility for modeling barrier functions and solute exchange in tissue-mimetic systems.

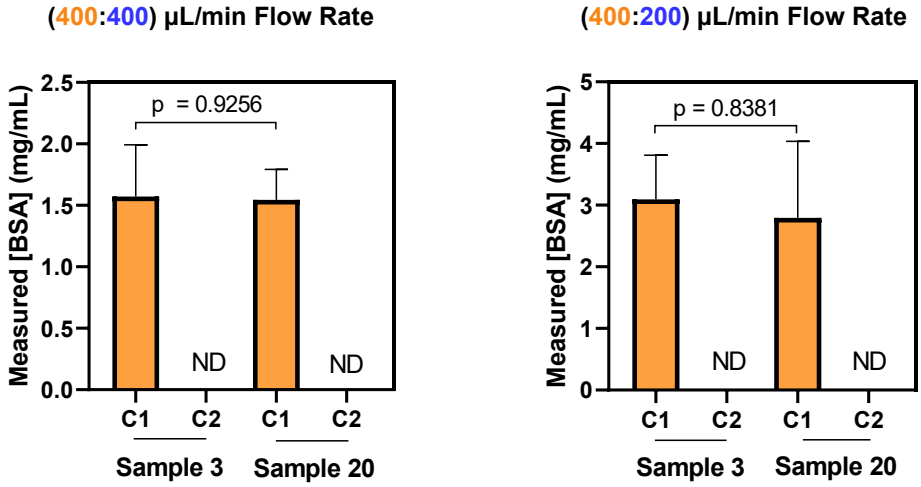

Figure 3.9: **BSA measured concentrations in circuit 1 (C1) and in circuit 2 (C2).** Mean ± SD concentrations of BSA (n = 3–6) in circuits 1 and 2 at various flow rates, measured at the beginning (sample 3) and end (sample 20) of the experiments.

4

Discussion

This work reported the development of a fully automated microfluidic platform integrating high-precision, pressure-driven flow control with dual recirculation loops featuring failsafe volume monitoring, programmable multi-reagent injection (10-1500 µL), synchronized multi-chamber sample collection, real-time DO monitoring, and temperature regulation. This integrated design addresses critical limitations of existing OC and microfluidic barrier models, including complex operation, operator-induced variability, and limited temporal resolution in transport studies. Pressure-driven flow was selected for its superior stability, responsiveness, and programmability, enabling generation of both steady and pulsatile flow regimes that emulate physiological microenvironments. Automated actuation and programmable sequence scheduling substantially reduces manual handling, thereby enhancing experimental reproducibility and facilitating inter-laboratory standardization. The thermal chamber accommodates both commercial and custom-fabricated chips with standard microscope-slide dimensions, while the main control module is designed to fit within standard biosafety cabinets—ensuring sterile operation for future live-cell applications. Flow rate distributions exhibited non-normal characteristics, attributed primarily to transient overshoot and undershoot events occurring during system initialization and stabilization. Occasional deviations were further linked to thermal flow-sensor sensitivity, mechanical perturbations, or the presence of air bubbles. Nevertheless, the platform maintained stable and reproducible flow profiles under steady-state conditions. The integrated DO enabled real-time monitoring of oxygenation levels, closely reflecting the pO_2 and the absolute pressure (p_{abs}) in the working fluid, as described by the relation DO (%) = 100 x pO_2/p_{abs}. The slow pO_2 fluctuations observed during continuous operation were thus attributed to gradual variations in p_{abs} as the reservoirs emptied [96].

A key feature of the system lies in its incorporation of capacitive level sensors, which maintain fluid volumes remain above a defined threshold within each reservoir and thereby prevent air ingress and interruptions in flow. These sensors enable real-time adjustment of reservoir-switching intervals based on measured, rather than theoretical, liquid volumes. This adaptive control compensates for small deviations caused by factors such as sensor

drift, entrained air bubbles, minor leakage, or gradual biofouling. The measured switching intervals scaled proportionally with flow rate, confirming the accuracy and reliability of the implemented volume-tracking logic. For example, a 50% reduction in flow rate led to an approximately twofold increase in the switching interval, consistent with the expected linear relationship. In addition to their volume-monitoring function, the sensors also contribute to the automated injection subsystem, which performed comparably to manual injection and mixing while offering significant advantages in reproducibility and user safety. The absence of vigorous mixing or agitation prevented foam formation, a particularly beneficial characteristic when handling viscous fluids or protein-rich media, such as cell culture medium supplemented with fetal bovine serum (FBS). The modular sampling architecture of the platform further enables precise, time-resolved analyses of molecular transport and retention within and across barrier compartments. This configuration allows for quantitative assessment of solute transfer, compound retention, and material losses arising from membrane adsorption or tubing interactions. The ability to capture such high-resolution kinetic data represents an essential advancement for characterizing pharmacokinetics and barrier functionality *in vitro*.

The results and mass balance analysis confirm that molecular transport across a semipermeable barrier depends on multiple interacting forces, not solely on concentration gradients (Fig. 3.7). This underscores the need for synchronized, dual-point concentration measurements to distinguish advective and osmotic effects. The platform is particularly suited for studying non-equilibrium systems, such as the human kidney, where dynamic flow conditions prevail. Solvent drag, arising from osmotic forces and solute-solvent interactions, can significantly afect transport behavior in OC and MPS models. Neglecting this phenomenon risks misinterpreting the physiological relevance of *in vitro* data. Thus, accurate quantification of transport dynamics under non-equilibrium conditions requires tightly controlled flow and synchronized sampling from both sides of the biomimetic barrier.

5

Conclusions

This work introduces a fully automated microfluidic platform designed for time-resolved and physiologically relevant analysis of molecular transport across barrier membrane models. The system overcomes major limitations of current microfluidic and OC technologies, including the reliance on manual fluid handling, limited reproducibility, and insufficient temporal resolution. Through the integration of pressure-driven flow regulation, dual recirculation loops with level-based volume sensing, programmable multi-reagent injection, synchronized multi-chamber sampling, real-time DO monitoring, and temperature stabilization, the platform enables long-term, precisely controlled perfusion experiments with minimal user intervention. The automated operation enhances experimental consistency and facilitates methodological standardization across laboratories. The work developed emphasizes the importance of implementing automated, high-precision flow control with real-time monitoring to ensure reliable and repeatable measurements. Comprehensive characterization of molecular transport—including the contribution of concurrent forces, such as solvent drag—is essential for translating microfluidic data to physiological contexts. The proof-of-concept validation, performed using a semipermeable biomimetic membrane model simulating processes akin to glomerular filtration, confirmed the platform's ability to capture dynamic molecular transport behavior. The system reliably captured dynamic transport kinetics and distinguished molecular permeability as a function of solute size. This technology marks a significant advancement in the field of MPS, effectively bridging the gap between benchtop microfluidics and physiologically representative *in vitro* models. With its high degree of automation, real-time sensing, and modular design, the platform provides a robust and versatile tool for preclinical drug screening, toxicological assessment, and mechanistic studies of barrier transport under controlled and reproducible conditions.

5.1 Future Work

Following the validation of system's automation and its suitability for dynamic molecular transport assays, future work will focus on biologically relevant cell models seeded

onto a bioprinted placental membrane to further evaluate system performance. Once membrane fabrication and cell seeding are successfully established, the permeability of two representative compounds—bisphenol A (a synthetic chemical associated with endocrine disruption) and doxycycline (a widely used antibiotic)—will be systematically investigated. Assessing their diffusion across the engineered membrane will provide valuable insights into placental barrier function and the potential risks these compounds pose during pregnancy, as exposure among pregnant women is common while their effects remain insufficiently understood. This model will enable evaluation of whether such exposures compromise placental integrity in ways that may contribute to maternal complications or adverse fetal development. Ultimately, the system is envisioned as a physiologically relevant *in vitro* platform for studying placental chemical transfer and its implications in maternal-fetal health.

Bibliography

[1] J. M. Lourenço. *The NOVAthesis LaTeX Template User's Manual*. NOVA University Lisbon. 2021. URL: https://github.com/joaomlourenco/novathesis/raw/main/template.pdf (cit. on p. i).

[2] H. Dowden and J. Munro. "Trends in clinical success rates and therapeutic focus". In: *Nat Rev Drug Discov* 18.7 (2019), pp. 495–496. DOI: 10.1038/d41573-019-00074-z (cit. on p. 1).

[3] O. J. Wouters, M. McKee, and J. Luyten. "Estimated research and development investment needed to bring a new medicine to market, 2009-2018". In: *Jama* 323.9 (2020), pp. 844–853. DOI: 10.1001/jama.2020.1166 (cit. on p. 1).

[4] J. W. Scannell et al. "Diagnosing the decline in pharmaceutical R&D efficiency". In: *Nature reviews Drug discovery* 11.3 (2012), pp. 191–200. DOI: 10.1038/nrd3681 (cit. on p. 1).

[5] D. Huh, G. A. Hamilton, and D. E. Ingber. "From 3D cell culture to organs-on-chips". In: *Trends in cell biology* 21.12 (2011), pp. 745–754. DOI: 10.1016/j.tcb.2011.09.005 (cit. on p. 1).

[6] F. Pampaloni, E. G. Reynaud, and E. H. Stelzer. "The third dimension bridges the gap between cell culture and live tissue". In: *Nature reviews Molecular cell biology* 8.10 (2007), pp. 839–845. DOI: 10.1038/nrm2236 (cit. on p. 1).

[7] S. N. Bhatia and D. E. Ingber. "Microfluidic organs-on-chips". In: *Nature biotechnology* 32.8 (2014), pp. 760–772. DOI: 10.1038/nbt.2989 (cit. on p. 1).

[8] L. A. Low et al. "Organs-on-chips: into the next decade". In: *Nature Reviews Drug Discovery* 20.5 (2021), pp. 345–361. DOI: 10.1038/s41573-020-0079-3 (cit. on p. 1).

[9] Y. I. Wang et al. "Multiorgan microphysiological systems for drug development: strategies, advances, and challenges". In: *Advanced healthcare materials* 7.2 (2018). DOI: 10.1002/adhm.201701000 (cit. on p. 1).

[10] D. E. Ingber. "Human organs-on-chips for disease modelling, drug development and personalized medicine". In: *Nature Reviews Genetics* 23.8 (2022), pp. 467–491. DOI: 10.1038/s41576-022-00466-9 (cit. on p. 1).

[11] A. Chramiec et al. "Integrated human organ-on-a-chip model for predictive studies of anti-tumor drug efficacy and cardiac safety". In: *Lab on a Chip* 20.23 (2020), pp. 4357–4372. DOI: 10.1039/d0lc00424c (cit. on pp. 1, 5, 6).

[12] H. Hammer et al. "Cross-species analysis of hepatic cytochrome P450 and transport protein expression". In: *Archives of toxicology* 95.1 (2021), pp. 117–133. DOI: 10.1007/s00204-020-02939-4 (cit. on p. 1).

[13] Y. Mai et al. "Quantification of P-glycoprotein in the gastrointestinal tract of humans and rodents: methodology, gut region, sex, and species matter". In: *Molecular Pharmaceutics* 18.5 (2021), pp. 1895–1904. DOI: 10.1021/acs.molpharmaceut.0c00574 (cit. on p. 1).

[14] J. C. Chaves et al. "Blood-brain barrier transporters: An overview of function, dysfunction in Alzheimer's disease and strategies for treatment". In: *Biochimica et Biophysica Acta (BBA)-Molecular Basis of Disease* 1870.2 (2024). DOI: 10.1016/j.bbadis.2023.166967 (cit. on p. 1).

[15] S. Zhang et al. "The barrier and interface mechanisms of the brain barrier, and brain drug delivery". In: *Brain Research Bulletin* 190 (2022), pp. 69–83. DOI: 10.1016/j.brainresbull.2022.09.017 (cit. on p. 1).

[16] C. Chelakkot, J. Ghim, and S. H. Ryu. "Mechanisms regulating intestinal barrier integrity and its pathological implications". In: *Experimental & molecular medicine* 50.8 (2018), pp. 1–9. DOI: 10.1038/s12276-018-0126-x (cit. on p. 1).

[17] L. Yang et al. "Biotransformation and transplacental transfer of the anti-viral remdesivir and predominant metabolite, GS-441524 in pregnant rats". In: *EBioMedicine* 81 (2022). DOI: 10.1016/j.ebiom.2022.104095 (cit. on p. 1).

[18] B. Fuenzalida et al. "Modelling the maternal-fetal interface: An in vitro approach to investigate nutrient and drug transport across the human placenta". In: *Journal of Cellular and Molecular Medicine* 28.20 (2024). DOI: 10.1111/jcmm.70151 (cit. on pp. 1, 2).

[19] R. Booth and H. Kim. "Permeability analysis of neuroactive drugs through a dynamic microfluidic in vitro blood–brain barrier model". In: *Annals of biomedical engineering* 42 (2014), pp. 2379–2391. DOI: 10.1007/s10439-014-1086-5 (cit. on pp. 2, 5).

[20] M. Esch, T. King, and M. Shuler. "The role of body-on-a-chip devices in drug and toxicity studies". In: *Annual review of biomedical engineering* 13.1 (2011), pp. 55–72. DOI: 10.1146/annurev-bioeng-071910-124629 (cit. on pp. 2, 5).

[21] M. W. van Der Helm et al. "Microfluidic organ-on-chip technology for blood-brain barrier research". In: *Tissue barriers* 4.1 (2016). DOI: 10.1080/21688370.2016.1142493 (cit. on pp. 2, 6).

[22] M. A. Deli et al. "Lab-on-a-chip models of the blood–brain barrier: evolution, problems, perspectives". In: *Lab on a Chip* 24.5 (2024), pp. 1030–1063. DOI: 10.1039/d3lc00996c (cit. on p. 2).

[23] A. Veiga-Lopez et al. "Current approaches and advances in placental toxicology". In: *Trends in Endocrinology & Metabolism* (2025). DOI: 10.1016/j.tem.2025.05.001 (cit. on p. 2).

[24] J. R. C. European Commission. *European 3Rs Centres*. [Accessed on July 15th 2025]. 2024. URL: https://joint-research-centre.ec.europa.eu/projects-and-activities/reference-and-measurement/european-union-reference-laboratories/eu-reference-laboratory-alternatives-animal-testing-eurl-ecvam/knowledge-sharing-three-rs/knowledge-networks/european-3rs-centres_en (cit. on p. 2).

[25] G. M. Whitesides. "The origins and the future of microfluidics". In: *Nature* 442.27 (2006-07), pp. 368–373. DOI: 10.1038/nature05058 (cit. on p. 2).

[26] *Microfluidics: A general overview of microfluidics*. [Accessed on January 26th 2025]. URL: https://www.elveflow.com/microfluidic-reviews/general-microfluidics/a-general-overview-of-microfluidics/ (cit. on pp. 3, 5).

[27] *Microfluidics definition: experimental advantages*. [Accessed on January 26th 2025]. URL: https://www.elveflow.com/microfluidic-reviews/general-microfluidics/microfluidics-definitions/ (cit. on p. 3).

[28] L. Muiznieks, C. Chidiac, and I. Ferraboschi. *A comparative review of medium recirculation system setups*. [Accessed on January 27th 2025]. URL: https://microfluidics-innovation-center.com/reviews/comparative-review-medium-recirculation-system-setups/ (cit. on pp. 3, 4, 78).

[29] F. Zhang et al. "Pump-less platform enables long-term recirculating perfusion of 3D printed tubular tissues". In: *Advanced Healthcare Materials* 12.27 (2023-10). DOI: 10.1002/adhm.202300423 (cit. on p. 4).

[30] N. Mavrogiannis et al. "Microfluidics made easy: A robust low-cost constant pressure flow controller for engineers and cell biologists". In: *Biomicrofluidics* 10.3 (2016). DOI: 10.1063/1.4950753 (cit. on pp. 4, 5).

[31] H. Kimura et al. "Advancements in Microphysiological Systems: Exploring Organoids and Organ-on-a-Chip Technologies in Drug Development-Focus on Pharmacokinetics Related Organs". In: *Drug Metabolism and Pharmacokinetics* (2024). DOI: 10.1016/j.dmpk.2024.101046 (cit. on p. 5).

[32] D. Soto Veliz, K.-L. Lin, and C. Sahlgren. "Organ-on-a-chip technologies for biomedical research and drug development: A focus on the vasculature". In: *Smart medicine* 2.1 (2023). DOI: 10.1002/SMMD.20220030 (cit. on pp. 5, 6).

[33] Y. Fan et al. "Understanding drug nanocarrier and blood–brain barrier interaction based on a microfluidic microphysiological model". In: *Lab on a Chip* 23.7 (2023), pp. 1935–1944. DOI: 10.1039/d2lc01077a (cit. on p. 5).

[34] C. A. Fois et al. "Dynamic flow and shear stress as key parameters for intestinal cells morphology and polarization in an organ-on-a-chip model". In: *Biomedical Microdevices* 23.4 (2021). DOI: 10.1007/s10544-021-00591-y (cit. on p. 5).

[35] J. Yan et al. "Organ-on-a-chip: A New Tool for in vitro Research". In: *Biosensors and Bioelectronics* 216 (2022). DOI: 10.1016/j.bios.2022.114626 (cit. on pp. 5, 6).

[36] N. C. Peterson et al. "Application of microphysiological systems in biopharmaceutical research and development". In: *Lab on a Chip* 20.4 (2020), pp. 697–708. DOI: 10.1039/c9lc00962k (cit. on p. 5).

[37] J. Kim et al. "Glomerular filtration barrier modeling on a chip with tunable basement membrane deposition and 3D cultured podocytes". In: *Lab on a Chip* 23.15 (2023), pp. 3501–3517. DOI: 10.1039/d3lc00147d (cit. on p. 6).

[38] J. Tan et al. "Exploratory evaluation of EGFR-targeted anti-tumor drugs for lung cancer based on lung-on-a-chip". In: *Biosensors* 12.8 (2022). DOI: 10.3390/bios12080618 (cit. on p. 6).

[39] A. Bein et al. "Enteric coronavirus infection and treatment modeled with an immunocompetent human intestine-on-a-chip". In: *Frontiers in pharmacology* 12 (2021). DOI: 10.3389/fphar.2021.718484 (cit. on p. 7).

[40] Y. Wang et al. "Human brain organoid-on-a-chip to model prenatal nicotine exposure". In: *Lab Chip* 18 (6 2018), pp. 851–860. DOI: 10.1039/C7LC01084B (cit. on pp. 7, 8).

[41] R. L. Pemathilaka et al. "Placenta-on-a-Chip: In Vitro Study of Caffeine Transport across Placental Barrier Using Liquid Chromatography Mass Spectrometry". In: *Global Challenges* 3.3 (2019-02). DOI: 10.1002/gch2.201800112 (cit. on pp. 7, 8).

[42] Y. Zhu et al. "Placental Barrier-on-a-Chip: Modeling Placental Inflammatory Responses to Bacterial Infection". In: *ACS Biomaterials Science & Engineering* 4.9 (2018), pp. 3356–3363. DOI: 10.1021/acsbiomaterials.8b00653 (cit. on p. 7).

[43] W. Stillwell. "Chapter 14 - Membrane Transport". In: *An Introduction to Biological Membranes*. Ed. by W. Stillwell. Elsevier, 2013, pp. 305–337. ISBN: 978-0-444-52153-8 (cit. on pp. 9, 10).

[44] L. C. Craig and H.-C. Chen. "On a theory for the passive transport of solute through semipermeable membranes". In: *Proceedings of the National Academy of Sciences* 69.3 (1972), pp. 702–705. DOI: 10.1073/pnas.69.3.702 (cit. on p. 10).

[45] N. J. Yang and M. J. Hinner. "Getting across the cell membrane: an overview for small molecules, peptides, and proteins". In: *Site-Specific Protein Labeling: Methods and Protocols* (2014), pp. 29–53. DOI: 10.1007/978-1-4939-2272-7_3 (cit. on p. 10).

[46] P. Haney, K. Herting, and S. Smith. *Separation Characteristics of Dialysis Membranes*. Thermo Fisher Scientific Protein Biology Application Notes. [Accessed on August 16th 2025]. 2013. URL: https://www.thermofisher.com/pt/en/home/life-science/protein-biology/protein-biology-learning-center/protein-biology-resource-library/protein-biology-application-notes/separation-characteristics-dialysis-membranes.html (cit. on p. 10).

[47] Y.-Y. Won and D. Ramkrishna. "Addition to "Revised Formulation of Fick's, Fourier's, and Newton's Laws for Spatially Varying Linear Transport Coefficients"". In: *ACS omega* 5.51 (2020), pp. 33484–33487. DOI: 10.1021/acsomega.0c02856 (cit. on p. 11).

[48] Y. Demirel. "Nonequilibrium thermodynamics modeling of coupled biochemical cycles in living cells". In: *Journal of Non-Newtonian Fluid Mechanics* 165.17-18 (2010), pp. 953–972. DOI: 10.1016/j.jnnfm.2010.02.006 (cit. on p. 11).

[49] X. Fang et al. "Nonequilibrium physics in biology". In: *Reviews of Modern Physics* 91.4 (2019). DOI: 10.1103/RevModPhys.91.045004 (cit. on p. 11).

[50] C. Åberg et al. "A theoretical study of diffusional transport over the alveolar surfactant layer". In: *Journal of the royal society interface* 7.51 (2010), pp. 1403–1410. DOI: 10.1098/rsif.2010.0082 (cit. on p. 11).

[51] H. Fan, Q. Cai, and Z. Qin. "Measurement and Modeling of Transport Across the Blood–Brain Barrier". In: *Journal of Biomechanical Engineering* 145.8 (2023). DOI: 10.1115/1.4062737 (cit. on p. 11).

[52] D. Günzel. "Is there a molecular basis for solvent drag in the renal proximal tubule?" In: *Pflügers Archiv-European Journal of Physiology* 475.2 (2023), pp. 277–281. DOI: 10.1007/s00424-022-02773-w (cit. on pp. 11, 12).

[53] D. Singh et al. "Journey of organ on a chip technology and its role in future healthcare scenario". In: *Applied Surface Science Advances* 9 (2022). DOI: 10.1016/j.apsadv.2022.100246 (cit. on p. 11).

[54] U. A. Gurkan et al. "Next generation microfluidics: fulfilling the promise of lab-on-a-chip technologies". In: *Lab on a Chip* 24.7 (2024), pp. 1867–1874. DOI: 10.1039/d3lc00796k (cit. on p. 11).

[55] L. R. Soenksen et al. "Closed-loop feedback control for microfluidic systems through automated capacitive fluid height sensing". In: *Lab on a Chip* 18.6 (2018), pp. 902–914. DOI: 10.1039/c7lc01223c (cit. on p. 11).

[56] H. Zhu et al. "Portable and integrated microfluidic flow control system using off-the-shelf components towards organs-on-chip applications". In: *Biomedical microdevices* 25.2 (2023). DOI: 10.1007/s10544-023-00657-z (cit. on p. 11).

[57] D. Leckband and J. Israelachvili. "Intermolecular forces in biology". In: *Quarterly reviews of biophysics* 34.2 (2001), pp. 105–267. DOI: 10.1017/s0033583501003687 (cit. on pp. 11, 12).

[58] J. A. Dix, D. Kivelson, and J. M. Diamond. "Molecular motion of small nonelectrolyte molecules in lecithin bilayers". In: *The Journal of Membrane Biology* 40.4 (1978), pp. 315–342. DOI: 10.1007/BF01874162 (cit. on p. 11).

[59] A. S. Verkman. "Solute and macromolecule diffusion in cellular aqueous compartments". In: *Trends in biochemical sciences* 27.1 (2002), pp. 27–33. DOI: 10.1016/s0968-0004(01)02003-5 (cit. on p. 11).

[60] T. Yamaguchi and Y. Kimura. "Effects of solute-solvent and solvent-solvent attractive interactions on solute diffusion". In: *Molecular Physics* 98.19 (2000), pp. 1553–1563. DOI: 10.1080/00268970009483361 (cit. on p. 12).

[61] R. Kayal et al. "Understanding and quantifying the impact of solute–solvent van der Waals interactions on the selectivity of asymmetric catalytic transformations". In: *Chemical Science* 16.6 (2025), pp. 2700–2709. DOI: 10.1039/d4sc04329d (cit. on p. 12).

[62] C. M. Roth, B. L. Neal, and A. M. Lenhoff. "Van der Waals interactions involving proteins". In: *Biophysical journal* 70.2 (1996), pp. 977–987. DOI: 10.1016/S0006-3495(96)79641-8 (cit. on p. 12).

[63] R. L. Baldwin. "Weak interactions in protein folding: hydrophobic free energy, van der Waals interactions, peptide hydrogen bonds, and peptide solvation". In: *Protein folding handbook* (2005), pp. 127–162. DOI: 10.1002/9783527619498.ch6 (cit. on p. 12).

[64] M. D. Fayer. "Dynamics of water interacting with interfaces, molecules, and ions". In: *Accounts of chemical research* 45.1 (2012), pp. 3–14. DOI: 10.1021/ar2000088 (cit. on p. 12).

[65] J. R. Pliego. "The role of intermolecular forces in ionic reactions: the solvent effect, ion-pairing, aggregates and structured environment". In: *Organic & Biomolecular Chemistry* 19.9 (2021), pp. 1900–1914. DOI: 10.1039/d0ob02413a (cit. on p. 12).

[66] T. L. Brown et al. *Chemistry: the central science*. Vol. 13. Prentice Hall Englewood Cliffs, NJ, 1997 (cit. on p. 12).

[67] N. Ferrell et al. "Effects of pressure and electrical charge on macromolecular transport across bovine lens basement membrane". In: *Biophysical journal* 104.7 (2013), pp. 1476–1484. DOI: 10.1016/j.bpj.2013.01.062 (cit. on p. 13).

[68] J. Michael and J. McFarland. "Another look at the core concepts of physiology: revisions and resources". In: *Advances in Physiology Education* 44.4 (2020), pp. 752–762. DOI: 10.1152/advan.00114.2020 (cit. on p. 13).

[69] H. I. Modell. "How to help students understand physiology? Emphasize general models." In: *Advances in Physiology Education* 23.1 (2000), pp. 101–107. DOI: 10.1152/advances.2000.23.1.S101 (cit. on p. 13).

[70] J. Michael and H. Modell. "Validating the core concept of "mass balance"". In: *Advances in Physiology Education* 45.2 (2021), pp. 276–280. DOI: 10.1152/advan.00235.2020 (cit. on p. 13).

[71] K. Ebefors et al. "Modeling the glomerular filtration barrier and intercellular crosstalk". In: *Frontiers in Physiology* 12 (2021). DOI: 10.3389/fphys.2021.689083 (cit. on p. 14).

[72] S. Guandalini. "Intestinal ion and nutrient transport in health and infectious diarrhoeal diseases". In: *Drugs* 36 (1988), pp. 26–38. DOI: 10.2165/00003495-198800364-00006 (cit. on p. 13).

[73] P. R. Kiela and F. K. Ghishan. "Physiology of Intestinal Absorption and Secretion". In: *Best Practice & Research Clinical Gastroenterology* 30.2 (2016), pp. 145–159. DOI: 10.1016/j.bpg.2016.02.007 (cit. on p. 13).

[74] L. M. Herda et al. "Designing the future of nanomedicine: current barriers to targeted brain therapeutics". In: *European Journal of Nanomedicine* 6.3 (2014), pp. 127–139. DOI: 10.1515/ejnm-2014-0022 (cit. on pp. 13, 14).

[75] G. M. Cooper and K. Adams. *The cell: a molecular approach*. Oxford University Press, 2022 (cit. on p. 14).

[76] I. Chen and F. Lui. *Physiology, Active Transport*. StatPearls Publishing, Treasure Island (FL), 2022 (cit. on p. 15).

[77] S. Balaz, E. Sturdík, and J. Augustin. "Kinetics of non-equilibrium metabolism-coupled passive transport in biosystems". In: *General physiology and biophysics* 6 (1987), pp. 65–77. DOI: 10.1016/0301-4622(86)80006-0 (cit. on p. 15).

[78] F. Guzmán-Lastra, H. Löwen, and A. J. Mathijssen. "Active carpets drive non-equilibrium diffusion and enhanced molecular fluxes". In: *Nature communications* 12.1 (2021). DOI: 10.1038/s41467-021-22029-y (cit. on p. 15).

[79] P. T. Cummings and D. J. Evans. "Nonequilibrium Molecular Dynamics Approaches to Transport Properties and Non-Newtonian Fluid Rheology". In: *Industrial & Engineering Chemistry Research* 31 (1992), pp. 1237–1252. DOI: 10.1021/ie00005a001 (cit. on p. 15).

[80] A. S. F. Oliveira et al. "Dynamical nonequilibrium molecular dynamics reveals the structural basis for allostery and signal propagation in biomolecular systems". In: *The European Physical Journal B* 94.7 (2021). DOI: 10.1140/epjb/s10051-021-00157-0 (cit. on p. 15).

[81] M. Fayaz-Torshizi et al. "Use of boundary-driven nonequilibrium molecular dynamics for determining transport diffusivities of multicomponent mixtures in nanoporous materials". In: *The Journal of Physical Chemistry B* 126.5 (2022), pp. 1085–1100. DOI: 10.1021/acs.jpcb.1c09159 (cit. on p. 15).

[82] L. Wang et al. "Water transport in reverse osmosis membranes is governed by pore flow, not a solution-diffusion mechanism". In: *Science Advances* 9.15 (2023). DOI: 10.1126/sciadv.adf8488 (cit. on p. 15).

[83] D. J. Rankin and D. M. Huang. "Non-equilibrium molecular dynamics of steady-state fluid transport through a 2D membrane driven by a concentration gradient". In: *The Journal of Chemical Physics* 159.21 (2023-12). DOI: 10.1063/5.0178576 (cit. on p. 15).

[84] A. Güvensoy-Morkoyun et al. "Guide for Nonequilibrium Molecular Dynamics Simulations of Organic Solvent Transport in Nanopores: The Case of 2D MXene Membranes". In: *Journal of Chemical Theory and Computation* 20.21 (2024), pp. 9642–9654. DOI: 10.1021/acs.jctc.4c00693 (cit. on p. 15).

[85] B. Shan et al. "Molecular kinetic modelling of non-equilibrium transport of confined van der Waals fluids". In: *Journal of Fluid Mechanics* 976 (2023). DOI: 10.1017/jfm.2023.893 (cit. on p. 15).

[86] J. Wijmans and R. Baker. "The solution-diffusion model: a review". In: *Journal of Membrane Science* 107.1 (1995), pp. 1–21. ISSN: 0376-7388. DOI: 10.1016/0376-7388(95)00102-I (cit. on p. 15).

[87] J. He et al. "Molecular simulations of organic solvent transport in dense polymer membranes: Solution-diffusion or pore-flow mechanism?" In: *Journal of Membrane Science* 708 (2024). ISSN: 0376-7388. DOI: 10.1016/j.memsci.2024.123055 (cit. on p. 15).

[88] O. Fournier, T. Gavoille, and L. D. Muiznieks. "A user's guide to barrier model perfusion: An automated microfluidic platform for ease of multi-functional control". In: *EUROoCS Conference*. 2024-07 (cit. on p. 16).

[89] *LIFESAVER Project*. [Accessed on January 24th 2025]. URL: https://lifesaverproject.eu/ (cit. on p. 17).

[90] M. B. Wolf, P. D. Watson, and D. Scott 2nd. "Integral-mass balance method for determination of solvent drag reflection coefficient". In: *American Journal of Physiology-Heart and Circulatory Physiology* 253.1 (1987). DOI: 10.1152/ajpheart.1987.253.1.H194 (cit. on pp. 22, 35).

[91] Agilent Technologies. *The Basics of UV–Vis Spectroscopy*. Publication No. 5980-1397EN. Agilent Technologies. 2021-07. URL: https://www.agilent.com/cs/library/primers/public/primer-uv-vis-basics-5980-1397en-agilent.pdf (cit. on p. 23).

[92] Agilent Technologies. *An Introduction to the Fundamentals of Fluorescence Spectroscopy—Including Fluorescence, Phosphorescence, Bioluminescence & Chemiluminescence*. [Accessed on July 23rd 2025]. Agilent Technologies. URL: https://www.agilent.com/en/support/molecular-spectroscopy/fluorescence-spectroscopy/what-is-fluorescence-spectroscopy-faqs (cit. on p. 23).

[93] BioTek® Instruments, Inc. *Synergy™ 2 Multi-Mode Microplate Reader: Operator's Manual*. Revision E. Part Number 7131000. BioTek Instruments, Inc. Winooski, Vermont, USA, 2010 (cit. on pp. 23, 24).

[94] D. Stone and J. Ellis. *Stats Tutorial - Instrumental Analysis and Calibration*. https://sites.chem.utoronto.ca/chemistry/coursenotes/analsci/stats/ttest.html. [Accessed on August 18th 2025]. 2006-08 (cit. on p. 26).

[95] P. H. Brown et al. "Density contrast sedimentation velocity for the determination of protein partial-specific volumes". In: *PloS one* 6.10 (2011). DOI: 10.1371/journal.pone.0026221 (cit. on p. 33).

[96] H. Bittig et al. *SCOR WG 142: Quality Control Procedures for Oxygen and Other Biogeochemical Sensors on Floats and Gliders. Recommendations on the conversion between oxygen quantities for Bio-Argo floats and other autonomous sensor platforms*. Report. 2018. DOI: 10.13155/45915 (cit. on p. 37).

[97] Elveflow. *Microfluidic Flow Controller*. [Accessed on January 27th 2025]. URL: https://www.elveflow.com/microfluidic-products/microfluidics-flow-control-systems/ob1-pressure-controller/ (cit. on p. 77).

[98] Elveflow. *Standard flow rate sensor*. [Accessed on January 27th 2025]. URL: https://www.elveflow.com/microfluidic-products/microfluidics-flow-measurement-sensors/microfluidic-liquid-mass-flow-sensor/ (cit. on p. 78).

A

Fluorescein Transport Rate

This appendix presents additional graphs (Fig. A.1) detailing fluorescein mass transport from circuit 1 into circuit 2, providing further support for the results presented in Section 3.3. The data shown correspond to successful experiments. Notably, only one graph is provided for the 400:400 μL/min flow rate condition due to the limited detection of accumulated fluorescein in circuit 2 across multiple trials. As previously discussed, the extended residence time in the 400:200 μL/min flow rate experiments facilitated observable fluorescein transport across the membrane, leading to its consistent measurable accumulation in circuit 2.

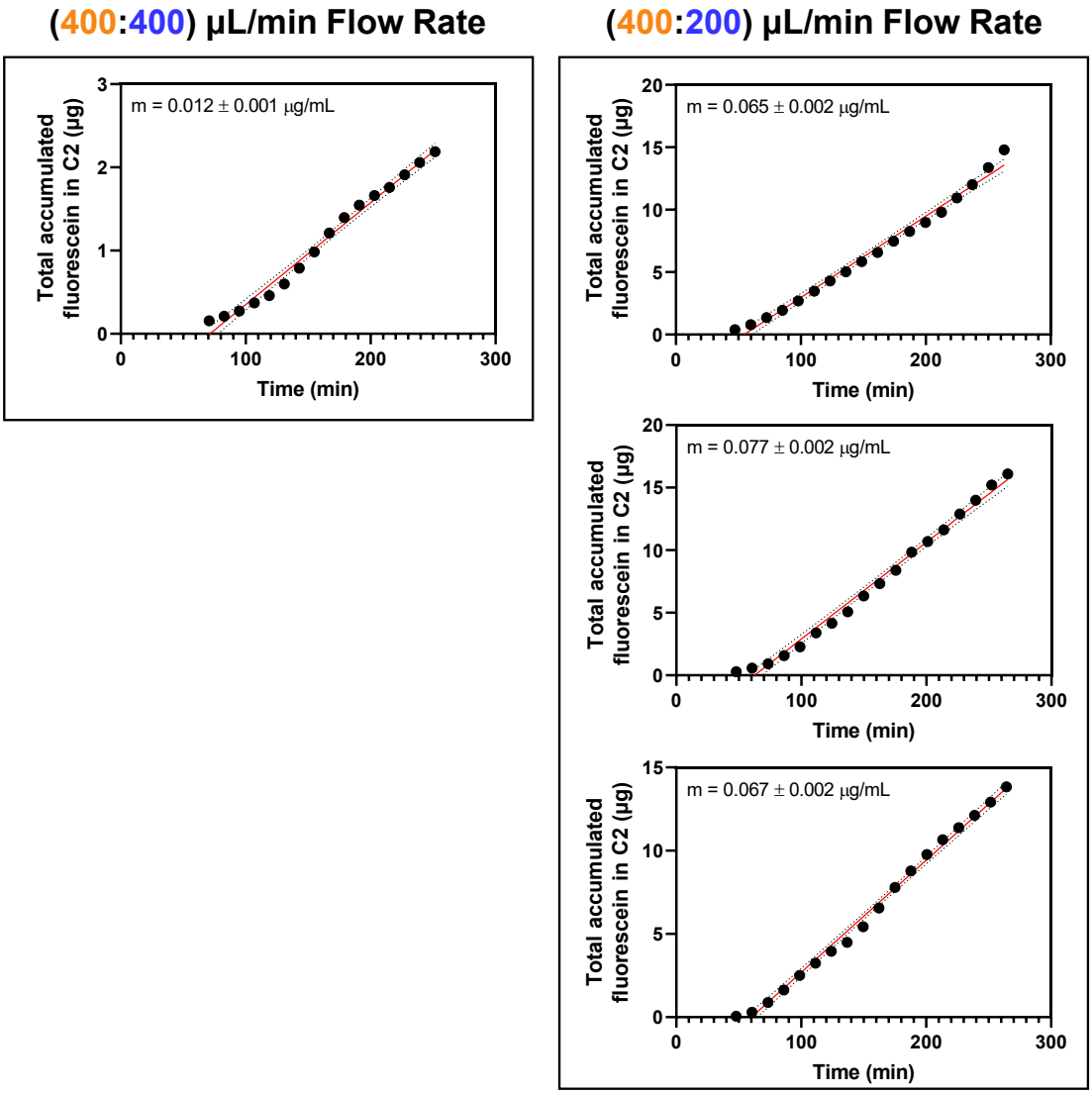

Figure A.1: **Different outcomes of fluorescein transport rates from circuit 1 to circuit 2 (C2) at the different flow rates studied.** 95% confidence intervals are indicated.

B

Co-authorship in a Scientific Paper

This appendix contains the full version of the manuscript that has been accepted for publication in the *Advanced Sensor Research* Journal.

Automated Microfluidic Platform for Molecular Transport Analysis Across Biomimetic Interfaces

Olivier Fournier[1], Miguel A.D. Neves[2,3], Théo Gavoille[1], Alan Morin[1], Beatriz Pais[2,3,4], Ivana Brenta[1], Justine Lereculey-Beaumanoir[1], Andrea Cruz[5], Denis Santos[5], Hugo Oliveira[5], Michael Gasik[6], Lisa D. Muiznieks[1,*], Inês Mendes Pinto[2,3,*]

[1] Microfluidics Innovation Center, 172 rue de Charonne 75011 Paris, France;
[2] Institute for Research and Innovation in Health (i3S), University of Porto, 4200-135 Porto, Portugal;
[3] Molecular and Analytical Medicine Laboratory, Department of Biomedicine, Faculty of Medicine, University of Porto, 4200-319 Porto, Portugal;
[4] NOVA School of Science and Technology, Physics Department, NOVA University of Lisbon, 2829-516 Caparica, Portugal;
[5] International Iberian Nanotechnology Laboratory (INL), 4715-330 Braga, Portugal;
[6] Seqvera Ltd. Oy, 00290 Helsinki, Finland.

*Co-corresponding authors: Lisa D. Muiznieks (lisa.muiznieks@microfluidic.fr) and Inês Mendes Pinto (ines.pinto@i3s.up.pt)

Abstract

Advancing drug development and disease modeling requires physiologically relevant *in vitro* systems capable of accurately reproducing the dynamic and selective transport functions of human tissue barriers. In line with ongoing regulatory initiatives (e.g., those by the European Union) aimed at reducing reliance on animal models, there is a growing need for standardized, scalable, and sensor-integrated microphysiological systems. Although microfluidic technologies—such as organ-on-chip platforms—have significantly improved *in vitro* biomimicry, many existing systems remain limited by technical complexity and a lack of integrated sensing for real-time, quantitative analysis, particularly under non-equilibrium conditions. Non-equilibrium molecular transport is a defining feature of several transport-active biological barriers (e.g., renal tubule, intestinal epithelium, blood–brain barrier, and placenta), which rely on coordinated active and passive transport mechanisms, directional fluid flow, and dynamic concentration gradients—features that are poorly captured by static or overly simplified models. In this manuscript, we present a fully automated microfluidic platform that integrates oxygen and flow sensors to enable dynamic, quantitative characterization of molecular transport across biomimetic interfaces. The system is designed to emulate critical biophysical features of physiological barriers—including flow directionality, controlled gradient formation, and tunable shear stress—using synthetic, cell-free architectures. Integrated oxygen sensors ensure the maintenance of physiologically relevant oxygen levels, a key determinant of metabolic activity and transport function. Complementary flow sensors enable closed-loop control of fluid dynamics, allowing precise modulation of solute delivery and hydrodynamic stress. Together, these sensing capabilities provide dynamic experimental control and support time-resolved analysis of molecular transport under non-equilibrium conditions. Although the current system is validated using acellular, biomimetic models, it is engineered for future integration with living cells. Furthermore, the platform establishes a foundation for real-time molecular sensorization within the microfluidic environment, offering potential for multiplexed molecular monitoring and high-resolution analysis of transport phenomena in organ-on-chip systems. Proof-of-concept studies demonstrate the platform's

ability to replicate key transport dynamics, underscoring its potential as a robust and scalable tool for pharmacokinetic modeling, organ-on-chip research, and preclinical drug development.

Introduction

Our mechanistic understanding of human pathophysiology, and consequently advancements in drug development and testing, faces a critical challenge: translating promising *in vitro* results into successful clinical outcomes. The high attrition rate in drug development, with an average R&D cost per approved drug estimated at least $2.8 billion with a success rate of only ~6.7% of candidates progressing from Phase I to regulatory approval, highlights a significant translational gap.[1–3] This challenge is largely attributed to the limitations of traditional preclinical models. Conventional 2D static cell cultures, while ubiquitous in initial drug screening, lack the intricate structural, mechanical, and biochemical cues of native tissues, as demonstrated in numerous studies.[4–6] Physiologically relevant extracellular matrix (ECM) interactions, cellular heterogeneity, dynamic biochemical gradients, mechanical strain, shear stress, and dynamic interstitial transport are crucial determinants of accurate *in vivo* drug responses.[6–10] Animal models, intended to bridge this gap, often introduce species-specific differences in drug metabolism (e.g., cytochrome P450 enzyme variations), transporter expression (e.g., P-glycoprotein), immune responses, and signaling pathways, limiting the translational relevance of animal testing to human physiology.[11,12] These limitations become particularly pronounced when assessing molecular transport across biological barriers.

Biological barriers—such as the blood-brain barrier (BBB), intestinal epithelium, alveolar capillary interface, placental barrier, and glomerular filtration barrier—are dynamic, selectively permeable interfaces that precisely regulate the bidirectional transport of ions, small molecules, and biomacromolecules between tissue compartments and the systemic circulation.[13–17] Physiologically relevant models of these barriers are essential for advancing our understanding of pharmacokinetic processes, including drug absorption, distribution, metabolism, and excretion, as well as for elucidating the mechanistic basis of broad spectrum of pathological conditions such as neurodegenerative diseases, cancer metastasis, and maternal-foetal disorders, among others.[17–20] Traditional *in vitro* models often fail to replicate the complex interplay of cellular and structural components of these dynamic interfaces, leading to inaccurate predictions of drug permeability, efficacy, and potential toxicities. For instance, static BBB models lacking relevant cell-cell interactions (e.g., astrocyte-endothelial cell interactions) and physiological shear stress can overestimate drug penetration and fail to capture the active efflux mechanisms mediated by transporters.[18–21] Furthermore, several *in vivo* animal models, including placental models, fail to emulate key human physiological and molecular features due to species-specific differences, limiting translational relevance. Simultaneously, ethical and regulatory guidelines—such as the European Union's 'Three Rs' initiative—advocate reduction, refinement and replacement of animal use in preclinical research, highlighting the need for advanced human-relevant *in vitro* platforms.

Microphysiological systems (MPS) including organ-on-a-chip (OoC) have emerged as a transformative technology in drug development and biomedical research, providing more accurate and physiologically relevant alternatives to conventional *in vitro* cultures and even *in vivo* animal models.[18,22–24] These models recreate *in vivo*-like microenvironments by incorporating 3D tissue architectures, dynamic fluid flow, controlled microenvironments, and the integration of multiple cell types, allowing for the simulation of key physiological processes, such as nutrient transport, shear stress, metabolic activity, and immune cell interactions.[23,25,26] Specifically, microfluidic barrier models typically consist of two or more channels separated

by a semipermeable membrane, allowing researchers to investigate selective permeability, transport kinetics, and barrier integrity across physiological interfaces.[10,27] Advanced designs have increasingly incorporated co-cultures of relevant cell types (e.g., astrocytes, neurons, and pericytes in BBB models), ECM components (e.g., collagen, laminin, and fibronectin) and microfabricated features (e.g., perfusable microvessels and microchannels), in order to replicate the structural and functional complexity of human tissues.[10,20,23]

Recent efforts have begun to integrate automation and sensing into OoC platforms, including electrochemical sensors for transepithelial electrical resistance, oxygen, and metabolite monitoring, as well as optical sensors for fluorescence-based tracking of molecular transport and dissolved gases.[28,29] While these approaches represent important advances, most systems remain limited by partial automation, single-parameter sensing, manual fluid handling, and the absence of closed-loop feedback control. Moreover, sensing and sampling are often restricted to one side of the barrier, limiting time-resolved analysis of transport under dynamic, non-equilibrium conditions.

Despite recent advancements in microfluidic technologies, widespread adoption and functional deployment of barrier-on-chip models are constrained by technical complexity, manual operation; including lack of automated fluid handling and feedback control, limited temporal resolution and capture of dynamic gradients, hindering reproducibility. A critical and unresolved challenge lies in accurately modeling and quantifying non-equilibrium molecular transport phenomena, which involves a complex interplay of passive diffusion, active transport, convective flows, and osmotic forces occurring simultaneously under heterogeneous fluid compositions and dynamic flow conditions. Importantly, non-equilibrium transport is a fundamental characteristic of several vital organs—such as the kidney, lung, and blood-brain barrier—where precisely regulated, dynamic molecular exchange governs essential physiological functions including filtration, absorption, and selective permeability. For example, the kidney's glomerular filtration barrier acts as a size- and charge-selective passive filter, permitting molecules smaller than ~15–30 kDa to pass into the urine. Although the effective cutoff of the native glomerular barrier is dynamic and context-dependent, this size range provides a useful physiological reference for in vitro filtration models. Accurately predicting filtration rates remains challenging due to strong osmotic forces generated by retained plasma proteins, which induce solvent drag and can reverse solute transport through molecular interactions such as hydrogen bonding and ionic forces.[30]

Generally, barrier-on-chip models are built within specifically designed microfluidic devices and lack sensing and sampling capabilities on both sides of the barrier. Without these sensing capabilities, it is almost impossible to predict and quantify non-equilibrium molecular transport across the barrier, thereby failing to replicate dynamic transport phenomena and compromising the predictive power and translational relevance of these models.[31–34]

To address these challenges, we present a fully automated microfluidic perfusion platform designed to improve physiological fidelity, operational robustness, and analytical precision in molecular transport studies. The system enables precise, automated regulation and time-resolved monitoring of key physicochemical parameters-including pressure-controlled flow rate, temperature, dissolved oxygen (DO) concentration and liquid recirculation-that are critical to reproducing the simultaneous interplay of different forces governing non-equilibrium molecular transport across barrier interfaces.

We validate platform performance with a proof-of-concept passive transport study using bovine serum albumin (BSA) and fluorescein as molecular tracers, demonstrating controlled, time-resolved quantification of molecular flux across a semipermeable membrane under physiologically relevant conditions that mimic glomerular filtration. Key features include high-precision pressure-driven flow control; dual recirculation loops with failsafe volume sensors; unidirectional perfusion; automated, programmable multi-reagent injection; synchronized

sample collection on both sides of the barrier; and integrated sensors for continuous monitoring of dissolved oxygen, flow rate, pressure, and temperature.
By integrating automation with multimodal sensing, this platform enables reproducible, closed-loop control of complex physicochemical environments and advances sensor-enabled microphysiological models for studying non-equilibrium transport and barrier dysfunction.

Experimental

Microfluidic hardware components, fabrication and software

The mechanical design of the platform was constructed using Solidworks. Electronics were commercially sourced (OB1 MK4 pressure-driven flow controller with 4 channels 0-2000 mbar, 12/1 MUX Distribution, MUX Wire, 3/2-way valves, MFS4 digital flow sensors range 30-1000 µL/min; Elveflow, France), except for the level sensors that were designed in house by integrating Zisenisc ZCT-YOF07 capacitive sensors (Farnell, France), and optical oxygen (O_2) sensors that were commercialized by Scientific Bioprocessing (Germany). The casing of the platform was printed using a FDM Printer (fused deposition modeling) Ultimaker S5 (Netherlands) with generic and tough polylactic acid (PLA). The fluidic path between the modules was made of polytetrafluoroethylene (PTFE) tubing, outer diameter (OD) 1/16″ and 1/32″, and inner diameter (ID) 1/32″ and 300 µm respectively (Darwin Microfluidics, France). The pneumatic path was made of polyurethane tubing, 4 mm OD, 2.5 mm ID (SMC, Japan). Tubing and modules were connected using polyether ether ketone (PEEK) and perfluoroalkoxy (PFA) ¼″-28 male to 1/16″ OD and 1/32″ OD tubing connectors, ethylene tetrafluoroethylene (ETFE) ¼″-28 female to Luer male connectors, polypropylene ¼″-28 swivel to barbed 3/32″ ID connectors (Cluzeau Info Labo, France), mini-Luer to 1/32″ OD tubing tuck-in connectors and silicon sleeve tubing (Microfluidic ChipShop GmbH, Germany). To complete the platform, pressure caps (Elveflow, France), heating unit (SADIJPR, China), and recirculation bridge units (Microfluidics Innovation Center, France) were used. The integrated platform control software and user interface were developed using LabVIEW (2022 Q3 release).

Microfluidic chip fabrication and assembly

The microfluidic chip was fabricated using a Stereolithography 3D Printer (Form2 printer, FormLabs, USA) with BioMed Clear Resin (FormLabs). The resin-based chip was designed in AutoCAD as two individual open square chambers of 20 x 20 x 13 mm, i.e. identical top and bottom halves. The chambers included a mini-Luer port on either side to serve as fluidic inlets/ outlets. Gaskets of ethylene propylene diene monomer (EPDM) rubber (1 mm thick; Solutions Elastomeres, France) were cut to secure a membrane between the two halves of the chip. Two squares (30 x 30 mm) were cut to overhang the edges of the chip. A smaller square (15 x 15 mm) was cut from the center of both gaskets with an X-acto cutter. A piece of nitrocellulose membrane (25 x 25 mm; 10 kDa molecular weight cut-off, MWCO) was super-glued (Loctite) on both sides between the gaskets, and a hard roller (Essdee) was used to firmly press the assembly flat. The membrane-gasket sandwich was then positioned between the two halves of the chip, and the whole assembly was secured with a clamp. The two chambers of the chip were filled with phosphate buffered saline (PBS, 140 mM NaCl, 10 mM sodium/potassium phosphate, and 3 mM KCl, pH 7.4) by hand using a 10 mL syringe via tubing (300 µm inner diameter) and mini-Luer connectors attached to the chip inlet.

Characterization of microfluidic modules

The individual tests of the microfluidic modules (flow rate control, recirculation, oxygen sensing, injection, collection) were performed using two union connectors instead of the chip,

and the Elveflow Smart Interface software (ESI, Elveflow, France) to control the system. The characterization of the complete platform with the integrated modules was performed using the microfluidic chip and the dedicated software to control and synchronize the system.

Molecular transport assay

Transport assays were performed using fluorescein (Sigma Aldrich) as a small-molecule tracer and bovine serum albumin (BSA; Sigma Aldrich) as a representative macromolecule, given its high abundance in blood. The platform proof-of-concept experiments were conducted using nitrocellulose dialysis tubing with a 10 kDa MWCO (ThermoFisher Scientific), stored under humid conditions. The membrane was assembled in the resin chip and the chambers were filled with a 1×PBS buffer, as described above. Prior to connecting the chip, the entire fluidic system was filled with PBS and for each circuit, 70 mL of PBS was split between the two reservoirs (45 mL in reservoir 1, 25 mL in reservoir 2). The chip was positioned with the membrane in a vertical orientation for transport assays. An aliquot for injection into circuit 1 (fluorescein and BSA; 1 mL) was prepared to result in a starting concentration (i.e. after injection) of 20 µg/mL fluorescein and 1 mg/mL BSA. The assembled chip was connected to the microfluidic platform and placed in a thermalized enclosure. Flow rates were set to 400 µL/min, circuit 1 and 200 µL/min, circuit 2 (400:200 ratio) or 400 µL/min in each circuit (400:400 ratio). An automated transport assay was initiated, during which 1 baseline sample and 19 transport samples were collected from both circuits (120 µL; 10-min intervals). Fluorescein concentrations in each collected sample were quantified via fluorescence spectroscopy (excitation/emission: 485/528 nm), while BSA transport was monitored by UV absorbance at 280 nm using a Synergy 2 HTX plate reader (BioTek).

The analysis of transport was based on integral-mass balance principles[35] (mass and flow conservation), assuming no additional sources or sinks for either the carrier fluid (PBS) or tracer compounds (BSA and fluorescein). Under continuous flow, with fixed tracer concentrations in the reservoirs of circuit 1, a system of differential equations[35] was established to balance the sum of inlet and outlet flows and the corresponding tracer mass fluxes. At steady state, it was assumed that no net accumulation of the tracer occurs within the membrane or circuits; therefore, the time derivatives of the tracer concentrations within the microfluidic chip compartments are approximately zero.

Statistical analysis

Statistical significance was determined using a Student's two-sample t-test for equal means; p-values are indicated accordingly.

Results

Design of an automated microfluidic platform for molecular transport assays

This work describes the development and proof of concept testing of a microfluidic perfusion platform from modular components to automate a transport assay, i.e. to enable the testing of compound transport across a semipermeable membrane resembling a biomimetic barrier. The platform was designed to address the need for protocol and technology standardization and automation, while maintaining general usability and adaptability for a range of applications, i.e., being independent of microfluidic chip geometry, membrane properties and specific cell model.

The core of the platform was designed as two fluidic pathways (circuit 1 and circuit 2) independently controlled by a main fluidic unit (Figs. 1A, B). These circuits were connected to each side of a biomimetic barrier-containing microfluidic chip that was housed within an integrated thermal chamber (Figs. 1A, B). This configuration meets the key requirements for monitoring the effect of a tracer compound on the biomimetic membrane and/or its transport across the membrane. The microfluidic platform featured an integrated set of functional modules to control independent liquid recirculation in each circuit, compound injection and mixing into circuit 1, and time-resolved sample collection from circuits 1 and 2 (Figs. 1C-E). Instrument modules were color-coded to indicate the two fluidic pathways and to aid assembly and operation. Dissolved oxygen was continuously monitored in-flow in each circuit. A thermal chamber was constructed to control the temperature of the molecular transport zone (between ambient temperature and 50 °C), e.g. providing the option for concurrent culture of cells on a membrane in the microfluidic chip, if desired.

Fluid flow was controlled by a pressure-driven flow controller (OB1 MK4, Elveflow) and two inline thermal flow sensors coupled to separate proportional-integral-derivative (PID) feedback loops for automated flow rate control. To maximize platform versatility and remain independent of flow rate and length of perfusion time, liquid handling pathways were integrated to recirculate between two reservoirs per circuit (here, 100 mL Schott bottles). One reservoir was pressurized (flowing) while the other was unpressurized (collecting) at any one time, alternating before the active reservoir ran dry (i.e. the reservoir from which liquid was being pushed). The recirculating flow path of each circuit was directed by a series of 3/2-way valves compatible with automated independent switching between the two reservoirs (Fig. 1B). Volume 'failsafe' level sensors were designed to signal the main control unit when a minimal volume of liquid remained in the active reservoir. This actuated an automated switch of active reservoir by switching the position of the valves to start pressurizing the now full reservoir (Figs. 1B, C). Fluidic routing used a recirculation bridge made from four check valves and four T-junctions in a square configuration that ensured liquid flow was always unidirectional through the microfluidic chip.

A distribution valve was used to enable the programmed sequential injection of up to four separate test compounds into reservoir 1 of circuit 1 (Figs. 1B, D). The test compound rack was compatible with Eppendorf tubes and thus, with injection volumes ranging from 10-1500 µL. Two automated sample collection units were developed to enable the time-resolved collection of up to 40 samples, positioned inline just after the microfluidic chip. Each sample collector was fitted with two integrated distribution valves and contained a removable rack for up to 20 Eppendorf-sized tubes aligned under a snap-shut lid fitted with fluidic tubing connection ports. The platform was designed to be compatible with a range of different commercial or home-made membrane chips, housed inside a thermal chamber. The microfluidic chip used here was composed of two identical rectangular chambers with mini-Luer ports for fluidic connection to microfluidic tubing (Fig. 1F).

Software design and function

Dedicated software was developed in LabVIEW to enable sequence scheduling and programming of the flow profile for full experiment automation (Fig. 2A). The user interface divided the required user inputs of experiment parameters (user parameters and saved configuration) and system parameters into separate tabs and fields. The software synchronized communication with all instruments controlling the flow (pressure controller, rotary valves and 3/2-way valve controller) to automate integrated functions, i.e., unidirectional circulation of medium in two circuits (through two separate chambers of the chip), injection and mixing of compounds into circuit 1, and timed collection of samples from both circuits 1 and 2.

The software controlled the instruments following a decision tree (Fig. 2B). A run initialization step was designed to identify and not accept nonsensical experiment parameters and instead alert the operator, e.g. incoherent timing of steps and lack of information on the compounds used. Upon launch of an experiment the sequence was programmed to commence a baseline phase. This was defined as perfusion of the microfluidic chip according to the input flow parameters of both fluidic circuits without a test compound, and the collection of a user-defined number of samples, e.g. one or more from each circuit to serve as baseline references. After baseline sample collection, the system was programmed to stop the flow, automatically inject the first compound and homogenize the contents of the two fluid reservoirs of circuit 1. Circulation was then reactivated and the software programmed to collect samples at time intervals set by the user. After taking the last sample for a given injected compound, the system was programmed to proceed with injection of the next compound, if relevant, or close all communication with the instruments and generate a data file and log file.

Characterization of module stability and accuracy

In order to preserve unidirectional flow through the microfluidic chip while using pressure-driven flow control, a recirculation bridge was designed and connected inline before the chip in each circuit. The flow pathway was directed by the specific orientation of two parallel pairs of check valves, based on the one-way passage of liquid through the valves (Fig. 3A). Opposite corners of the bridge were connected to the two liquid reservoirs, and the remaining corners were connected to and from the microfluidic chip (Fig. 1B). In cases where one T-junction offered two possible flow directions, flow circulated through the check valve with the lowest counter-pressure. This configuration allowed two different flow pathways inside the bridge, depending on which of the two reservoirs (R1 or R2) was being pressurized. Specifically, liquid flow from the bridge towards the chip was independent of reservoir origin, i.e., liquid exited the bridge from a single corner, regardless of which reservoir was pressurized (i.e. top left corner in orientation shown; Fig. 3A). Similarly, flow returning from the chip always re-entered the bridge at a single corner (bottom right; Fig. 3A).

The fluid control modules demonstrated stable and accurate flow regulation, consistent recirculation performance, and operational adaptability across diverse system conditions. The pressure-driven flow controller, flow sensors, volume level sensors and recirculation bridge modules were integrated to control the flow rates of the two independent circuits for 4.5 h (Fig. 3 B-D). For both circuits, the flow rate was stable and maintained at the target value. Normalized histograms of recorded flow rates (1 Hz acquisition frequency) were computed for experiments performed at different flow rate ratios: 400:400 ratio (400 µL/min in both circuits; Fig. 3B) and a 400:200 ratio (400 µL/min and 200 µL/min in circuits 1 and 2 respectively; Fig. 3C). Stabilized flow rates were measured at 400.0 ± 0.5 µL/min, 200.0 ± 0.4 µL/min (in circuit 1 and circuit 2 for 400:200 ratio), and 400.0 ± 1.1 µL/min, 400.0 ± 1.3 µL/min (in circuit 1 and circuit 2 for 400:400 ratio). As described, integrated reservoir volume level sensors were designed to enable the alternate pressurization of one reservoir per fluid circuit at a time, automatically triggering the pneumatic system to switch when a minimum liquid level was sensed,

and their function was demonstrated (Fig. 3D). Switches in reservoir pressurization were observed as a momentary drop in flow rate to near zero in the flow profiles of both circuits, as expected. A small peak was associated with every switch, indicating the feedback loop acting to stabilize the flow rate at the target value, consistent with a PID-controlled system. Intervals between successive switches were constant (105 min at 200 µL/min, 50 min at 400 µL/min), illustrating the working function of the level sensors (Fig. 3D). For both fluidic circuits, the length of the first reservoir pressurization was slightly different from the subsequent cycles, corresponding to the initial partition of liquid between the two reservoirs by the operator.
The evolution of the partial pressure of O_2 (p_{O2}) was measured in both circuits during the same 4.5 h-long experiment (Fig. 3E), synchronized with the flow rates (Fig. 3D) and remained stable over the course of the experiment (between 180 and 220 mbar). In both circuits, slow and small changes in p_{O2} were observed in synchrony with the alternating switch between reservoir 1 and reservoir 2, denoted by symbols Ψ and Φ, respectively (Fig. 3D).
A key parametrization step for an automated microfluidic transport assay is the addition of a compound into one circuit. The platform described here was designed to automate up to four separate injections of compound. Specifically, the injection sequence was programmed to add the compound into one of the two reservoirs of circuit 1, then to mix the contents of both reservoirs out of line with the main circuit, and finally to direct the liquid in line with the full circuit and microfluidic chip (Figs. 1B, 4A). Immediately before each injection, the contents of reservoir 1 (R1) were emptied into reservoir 2 (R2), after which, the compound was injected into R1 (step 1, Fig. 4A). The liquid was then circulated back and forth at high flow rate (> 100 mL/min) between R1 and R2, homogenizing the contents (step 2, Fig. 4A).
A series of tests were performed to assess the effectiveness of compound homogenization after successive cycles of back-forth mixing using fluorescein in water as the injected compound. Fluorescein was rapidly homogenized with the buffer in R1 and R2 of circuit 1 after one back-forth cycle, as demonstrated by comparable absorbances in both reservoirs (Fig. 4B). Efficiency of automated injection and mixing as compared to manual injection and shaking was tested for four identical sequential injections of fluorescein and reported for reservoir 1 (Fig. 4C). Absorbances were comparable for both automated and manual injection and mixing methods, and increased linearly with successive injections, indicating the effectiveness of the automated injection and mixing functions.
Two sample collection modules were integrated into the platform to enable automated collection at intervals and sample volumes as defined by the operator from both circuits. Performance and versatility were tested by the collection of three different target volumes in separate fully automated experiments. Collection tubes were weighed before and after sample collection and sample mass was expressed as volume after density correction (1.005584 g/mL for PBS at 20°C [36]). The average sample volumes collected were all within 1.5% of the target value (157 ± 10 µL, target 155 µL; 185 ± 12 µL, target 185 µL; 231 ± 9 µL, target 230 µL; mean ± SD, n=40 in each case; Fig. 4D).

Proof-of-concept: automated microfluidic system for analyzing transport dynamics across a semi-permeable barrier

A proof-of-concept assay was performed to demonstrate the system's capacity to monitor tracer transport across a semipermeable barrier. The assay was designed to mimic passive transport across barriers such as the glomerular filtration barrier, using a semipermeable nitrocellulose dialysis membrane with a nominal 10 kDa molecular weight cut-off (MWCO) as a proof-of-concept barrier. Nitrocellulose membranes offer well-defined porosity, low thickness, and reproducible transport characteristics, making them suitable for studying size-selective filtration and osmotic transport under pressure-driven perfusion. The selected MWCO provides

a conservative approximation of glomerular size selectivity while enabling systematic investigation of passive transport and solvent drag effects. Importantly, the platform architecture is membrane-agnostic, allowing future adaptation to alternative MWCOs and barrier configurations relevant to different organ systems.

The experiment also tested the synchronization of compound injection and sample collection with integrated flow rate and fluid recirculation control (Fig. 5). Two flow-rate combinations were evaluated: 400:400 µL/min and 400:200 µL/min (circuit 1: circuit 2). The compounds injected were a mixture of BSA (66 kDa) and fluorescein (0.33 kDa). Fluorescein is expected to diffuse across the membrane (circuit 1 to circuit 2; Fig. 5A), whereas BSA should not, thereby creating an osmotic gradient in the opposite direction (circuit 2 to circuit 1).

The recorded flow rates (Fig. 5B and F), working reservoir pressures (Fig. 5C and G), and event sequence (injection, collections; Fig. 5D and H) were synchronized over the span of a 4.5 h-long experiment that included one compound injection into circuit 1 and 20 collections of samples from each circuit. One sample was collected from both circuits as a baseline after 10 min of recirculation. Right after (t = 11 min), the compounds of interest were injected and mixed into circuit 1 (20 µg/mL fluorescein and 1 mg/mL BSA final reservoir concentrations) and the system was put to recirculation with the loaded medium. The 38 subsequent samples (19 per circuit) were collected at 10-min intervals. During a collection event, the flow was monitored separately in each circuit to prime the collection line, draw out the sample volume and clean the lines, characterized by the fast variations in pressure and flow rate. After each collection event, the PID algorithm drove the pressure to reach fast stabilization of the target flow rate in either circuit until the next collection event. It is noteworthy that at the moment of sampling the flow is instantly disturbed resulting in decayed oscillatory pressure changes (Fig. 3D and Fig. 5B-C and F-G). As the time interval between sampling is much larger than these perturbated events, this does not have a significant effect on shear rate along the membrane as observed in computational fluid dynamics (CFD) modelling (data not shown) as well as on the cumulative compounds transfer kinetics.

The concentrations of BSA and fluorescein in each of the 20 collected samples were determined using UV-Vis and fluorescence spectroscopy, respectively (Fig. 5E and I). For both flow rate ratios, fluorescein levels in circuit 1 progressively decreased while concentrations in circuit 2 increased, indicating directional transmembrane transport. However, the measured values suggest that fluorescein concentration decreased more rapidly in circuit 1 than it increased in circuit 2. These results are consistent with principles of non-equilibrium passive transport across the semipermeable barrier, driven by multiple forces beyond a simple diffusion concentration gradient of the permeable compound (Fig. 6A). This behavior is expected from thermodynamic principles: differences in chemical potentials between fluids drive not only the permeable tracer across the membrane but also counteracting osmotic and pressure-difference driven solvent flow (carry-over) — an effect exacerbated by fluctuations in pressure and flow rate. Therefore, to calculate an accurate transport rate across the membrane, the transported mass in both directions must be taken into account. The principle of integral mass balance[35,38] was employed to precisely characterize the kinetics of fluorescein transport (Fig. 6B and C). Analysis of transport kinetics showed that fluorescein accumulation in circuit 2 was significantly higher at a flow rate ratio of 400:200 µL/min than at 400:400 µL/min. This difference is consistent with the increased residence time in circuit 2 at the lower flow rate; however, under the present conditions it is not possible to distinguish whether the enhanced accumulation reflects flow-limited transport or simply the effect of prolonged residence time. These results indicate that transport efficiency is sensitive to flow asymmetry and residence time, but further studies are required to decouple these contributions. It is worth noting that no BSA was detected in circuit 2, suggesting that, as expected, BSA did not cross the membrane (Supplementary Figure 2).

The observed selective passage of small solutes demonstrates that the microfluidic platform supports controlled, size-dependent, and flow-sensitive molecular transport, validating its utility for modeling barrier functions and solute exchange in tissue-mimetic systems.

Discussion

We developed a fully automated microfluidic platform that integrates high-precision pressure-driven flow control, dual recirculation loops with failsafe volume monitoring, programmable multi-reagent injection (10–1500 µL), synchronized multi-chamber sample collection, real-time DO monitoring, and a temperature-controlled chamber. This integrated system addresses key limitations of current OoCs and microfluidic barrier models, including technical complexity, operator-induced variability, and restricted time-resolved analysis of transport. Pressure-driven flow was selected for its high stability, responsiveness, and programmability, enabling generation of both steady and pulsatile flow profiles to mimic physiological micro-environments. The implementation of automated actuation and programmable sequence scheduling minimizes manual intervention, improving reproducibility and supporting inter-laboratory standardization. The thermal chamber is compatible with both commercial and custom chips (standard microscope slide dimensions) and the main control module is designed to fit inside standard biosafety cabinets, enabling sterile operation in future live-cell applications. Flow rate distributions exhibited non-normal characteristics, which are attributed to inclusion of the system's initialization and stabilization phases. During these transitions, overshoot and undershoot events contributed to the skewness of the distribution. Isolated transient deviations were attributed to thermal flow sensor sensitivity to mechanical shocks or gas bubbles. Despite these perturbations, the system maintained stable flow profiles during steady-state operation. DO sensors were successfully integrated and allowed for real-time monitoring thereof. Since DO is related to p_{O2} and to the absolute pressure in the working fluid (p_{abs}) using the relation DO (%) = 100 x p_{O2}/p_{abs}, the observed slow p_{O2} fluctuations under continuous operation were ascribed to slow variation of p_{abs} as the reservoirs were emptying.[37]

A critical feature of the system is its use of capacitive level sensors to ensure fluid volumes remain above a defined threshold in each reservoir, preventing air ingress and flow disruption. These sensors allow real-time correction of reservoir switch timing based on measured rather than theoretical fluid volumes. This compensates for minor flow deviations arising from sensor drift, bubbles, leaks, or gradual biofouling. The measured switch intervals scaled appropriately with flow rate, confirming the accuracy of volume-tracking logic. For instance, halving the flow rate approximately doubled the interval between switching events, consistent with the expected linear relationship. They also contribute to the integrated injection system which proved as efficient as manual injection and homogenization of compound, with the added benefits of improving reproducibility and preventing the formation of foam (no bubbling or aggressive stirring involved). This is a valuable asset when working with viscous liquids and protein-rich solutions such as cell culture medium supplemented with fetal bovine serum (FBS). The modular sampling architecture supports time resolved analysis of molecular distribution and retention within and across barrier compartments. This design facilitates quantification of transport, compound retention, and potential losses due to membrane adsorption or tubing interaction. Such high-resolution kinetic data are essential for evaluating pharmacokinetics and barrier function *in vitro*.

The results and mass balance analysis are consistent with well-known physiological principles that molecular transport across a semipermeable barrier is not solely governed by concentration gradients but by a complex interplay of forces (Fig 6A). This highlights the critical importance of synchronized, dual-point concentration measurements on both sides of the membrane to

resolve advective and osmotic contributions. This platform is highly relevant for modeling non-equilibrium biological systems, such as the human kidney, where dynamic and heterogeneous flow conditions prevail—unlike static models, where fluid volume and solute mass are fixed. Solvent drag, arising from osmotic forces and solute-solvent interactions, can significantly influence transport behavior in OoC and MPS models. Neglecting this phenomenon risks misinterpreting the physiological relevance of *in vitro* data. Thus, accurate quantification of transport dynamics under non-equilibrium conditions requires tightly controlled flow and synchronized sampling from both sides of the biomimetic barrier. Importantly, while the current platform uses acellular membranes, the architecture is fully compatible with future integration of living cells, which will allow investigation of active transport, cellular barrier function, and mechanosensitive responses. Flow perturbations during sampling are expected to be minimal; however, their potential impact on shear-sensitive cell layers should be considered in future biological validation studies.

Conclusions

This study presents a fully automated microfluidic platform for time-resolved and physiologically relevant analysis of molecular transport across barrier membrane models. The system overcomes key limitations of existing microfluidic and organ-on-chip technologies, including manual fluid handling, low reproducibility, and limited temporal resolution. By integrating pressure-driven flow control, dual recirculation loops with level-based volume sensing, programmable multi-reagent injection, synchronized multi-chamber sampling, real-time dissolved oxygen monitoring, and thermal stabilization, the platform enables tightly controlled, long-term perfusion experiments with minimal user intervention. The automated operation enhances experimental consistency, supporting standardization across laboratories. Accurate characterization of molecular transport taking into account all the different forces involved, such as solvent drag, are essential for translating microfluidic data to physiological contexts. Proof-of-concept validation using a semipermeable biomimetic membrane model that mimics biological transport processes, such as glomerular filtration, demonstrated the system's suitability for dynamic molecular transport assays. Through the advanced and robust sampling capability on both sides of the barrier, the platform reliably captured dynamic transport kinetics and enabled quantitative discrimination of passive molecular transport. Future versions of the platform aim to include real-time inline sensors, such as aptamer-based electrochemical sensors, to further increase the resolution of quantitative molecular transport. This technology represents a significant advance in the field of MPS by bridging the gap between benchtop microfluidics and physiologically relevant *in vitro* models. Its robust automation, real-time monitoring capabilities, and modular architecture make it a powerful tool for preclinical drug screening, toxicology, and mechanistic studies of barrier function under controlled and reproducible conditions.

Data availability

Data supporting this article have been included as part of the ESI. Further data will be made available upon reasonable request to the corresponding authors.

Author contributions

Conceptualization, OF, MADN, MG, LDM, IMP; Methodology, OF, MADN, TG, AM, LDM, IMP; Software: OF; Validation: BP, IB, JLB; Formal Analysis: OF, MADN, MG, LDM, IMP; Investigation, OF, MADN, BP, IB, JLB, AC, DS, HO, MG, LDM, IMP; Resources: LDM and IMP; Data Curation: OF, MADN, LDM, IMP; Writing – original draft, OF, MADN, LDM,

IMP; Writing – review & editing, all authors; Supervision, OF, MADN, MG, LDM, IMP; Project Administration: LDM, IMP; Funding acquisition, MG, LDM, IMP.

Conflicts of interest
The authors declare no conflict of interest.

Acknowledgements
This work was financed by national funds through FCT – Fundação para a Ciência e a Tecnologia, I.P., and by the European Regional Development Fund (FEDER), under the COMPETE2030 Programme, project no. 15801 (FEDER-00691000), within the scope of Grant Call No. MPr-2023-12.- This research has received funding from the European Union under Horizon2020 programme through the LIFESAVER project (H2020-LC-GD-2020-3, grant agreement no. 101036702) and Micro4Nano (H2020-MSCA-RISE-2020, grant agreement no. 101007804).

References

1. Dowden, H. & Munro, J. Trends in clinical success rates and therapeutic focus. *Nat Rev Drug Discov* **18**, 495–496 (2019).
2. Wouters, O. J., McKee, M. & Luyten, J. Estimated Research and Development Investment Needed to Bring a New Medicine to Market, 2009-2018. *JAMA - Journal of the American Medical Association* **323**, 844–853 (2020).
3. Scannell, J. W., Blanckley, A., Boldon, H. & Warrington, B. Diagnosing the decline in pharmaceutical R&D efficiency. *Nat Rev Drug Discov* **11**, 191–200 (2012).
4. Pampaloni, F., Reynaud, E. G. & Stelzer, E. H. K. The third dimension bridges the gap between cell culture and live tissue. *Nat Rev Mol Cell Biol* **8**, 839–845 (2007).
5. Bhatia, S. N. & Ingber, D. E. Microfluidic organs-on-chips. *Nat Biotechnol* **32**, 760–772 (2014).
6. Huh, D., Hamilton, G. A. & Ingber, D. E. From 3D cell culture to organs-on-chips. *Trends Cell Biol* **21**, 745–754 (2011).
7. Low, L. A., Mummery, C., Berridge, B. R., Austin, C. P. & Tagle, D. A. Organs-on-chips: into the next decade. *Nat Rev Drug Discov* **20**, 345–361 (2021).
8. Wang, Y. I., Carmona, C., Hickman, J. J. & Shuler, M. L. Multiorgan microphysiological systems for drug development: strategies, advances, and challenges. *Adv Healthc Mater* **7**, (2018).
9. Ingber, D. E. Human organs-on-chips for disease modelling, drug development and personalized medicine. *Nat Rev Genet* **23**, 467–491 (2022).
10. Chramiec, A. *et al.* Integrated human organ-on-a-chip model for predictive studies of anti-tumor drug efficacy and cardiac safety. *Lab Chip* **20**, 4357–4372 (2020).
11. Hammer, H., Schmidt, F., Marx-Stoelting, P., Pötz, O. & Braeuning, A. Cross-species analysis of hepatic cytochrome P450 and transport protein expression. *Arch Toxicol* **95**, 117–133 (2021).
12. Mai, Y. *et al.* Quantification of P-Glycoprotein in the Gastrointestinal Tract of Humans and Rodents: Methodology, Gut Region, Sex, and Species Matter. *Mol Pharm* **18**, 1895–1904 (2021).
13. Chaves, J. C. S., Dando, S. J., White, A. R. & Oikari, L. E. Blood-brain barrier transporters: An overview of function, dysfunction in Alzheimer's disease and strategies for treatment. *Biochimica et Biophysica Acta (BBA) - Molecular Basis of Disease* **1870**, (2024).
14. Zhang, S. *et al.* The barrier and interface mechanisms of the brain barrier, and brain drug delivery. *Brain Res Bull* **190**, 69–83 (2022).
15. Chelakkot, C., Ghim, J. & Ryu, S. H. Mechanisms regulating intestinal barrier integrity and its pathological implications. *Exp Mol Med* **50**, (2018).
16. Yang, L., Lin, I.-H., Lin, L.-C., Dalley, J. W. & Tsai, T.-H. Biotransformation and transplacental transfer of the anti-viral remdesivir and predominant metabolite, GS-441524 in pregnant rats. *EBioMedicine* **81**, (2022).
17. Fuenzalida, B. *et al.* Modelling the maternal-fetal interface: An in vitro approach to investigate nutrient and drug transport across the human placenta. *J Cell Mol Med* **28**, (2024).
18. Booth, R. & Kim, H. Permeability analysis of neuroactive drugs through a dynamic microfluidic in vitro blood–brain barrier model. *Ann Biomed Eng* **42**, 2379–2391 (2014).
19. Esch, M. B., King, T. L. & Shuler, M. L. The role of body-on-a-chip devices in drug and toxicity studies. *Annu Rev Biomed Eng* **13**, 55–72 (2011).
20. van Der Helm, M. W., Van Der Meer, A. D., Eijkel, J. C. T., van den Berg, A. & Segerink, L. I. Microfluidic organ-on-chip technology for blood-brain barrier research. *Tissue Barriers* **4**, (2016).
21. Deli, M. A. *et al.* Lab-on-a-chip models of the blood-brain barrier: evolution, problems, perspectives. *Lab Chip* **24**, 1030–1063 (2024).
22. Kimura, H. *et al.* Advancements in Microphysiological systems: Exploring organoids and organ-on-a-chip technologies in drug development -focus on pharmacokinetics related organs-. *Drug Metab Pharmacokinet* **60**, (2025).
23. Soto Veliz, D., Lin, K. & Sahlgren, C. Organ-on-a-chip technologies for biomedical research and drug development: A focus on the vasculature. *Smart Medicine* **2**, (2023).
24. Esch, M. B., King, T. L. & Shuler, M. L. The role of body-on-a-chip devices in drug and toxicity studies. *Annu Rev Biomed Eng* **13**, 55–72 (2011).
25. Fan, Y. *et al.* Understanding drug nanocarrier and blood-brain barrier interaction based on a microfluidic microphysiological model. *Lab Chip* **23**, 1935–1944 (2023).

26. Fois, C. A. M., Schindeler, A., Valtchev, P. & Dehghani, F. Dynamic flow and shear stress as key parameters for intestinal cells morphology and polarization in an organ-on-a-chip model. *Biomed Microdevices* **23**, (2021).
27. Peterson, N. C., Mahalingaiah, P. K., Fullerton, A. & Di Piazza, M. Application of microphysiological systems in biopharmaceutical research and development. *Lab Chip* **20**, 697–708 (2020).
28. Izadifar, Z. *et al.* Organ chips with integrated multifunctional sensors enable continuous metabolic monitoring at controlled oxygen levels. *Biosens Bioelectron* **265**, 1-14 (2024).
29. Marrero, D. *et al.* Organ-on-a-chip with integrated semitransparent organic electrodes for barrier function monitoring. *Lab Chip* **23**, 1825–1834 (2023).
30. Günzel, D. Is there a molecular basis for solvent drag in the renal proximal tubule? *Pflugers Arch* **475**, 277–281 (2023).
31. Singh, D., Mathur, A., Arora, S., Roy, S. & Mahindroo, N. Journey of organ on a chip technology and its role in future healthcare scenario. *Applied Surface Science Advances* **9**, (2022).
32. Gurkan, U. A. *et al.* Next generation microfluidics: fulfilling the promise of lab-on-a-chip technologies. *Lab Chip* **24**, 1867–1874 (2024).
33. Soenksen, L. R., Kassis, T., Noh, M., Griffith, L. G. & Trumper, D. L. Closed-loop feedback control for microfluidic systems through automated capacitive fluid height sensing. *Lab Chip* **18**, 902–914 (2018).
34. Zhu, H., Özkayar, G., Lötters, J., Tichem, M. & Ghatkesar, M. K. Portable and integrated microfluidic flow control system using off-the-shelf components towards organs-on-chip applications. *Biomed Microdevices* **25**, (2023).
35. Wolf, M. B., Watson, P. D. & Scott 2nd, D. R. Integral-mass balance method for determination of solvent drag reflection coefficient. *American Journal of Physiology-Heart and Circulatory Physiology* **253**, H194-H204 (1987).
36. Brown, P. H., Balbo, A., Zhao, H., Ebel, C. & Schuck, P. Density contrast sedimentation velocity for the determination of protein partial-specific volumes. *PLoS One* **6**, (2011).
37. Bittig, H. *et al. SCOR WG 142: Quality Control Procedures for Oxygen and Other Biogeochemical Sensors on Floats and Gliders. Recommendations on the Conversion between Oxygen Quantities for Bio-Argo Floats and Other Autonomous Sensor Platforms*. (2018) doi:10.13155/45915.
38. Gasik, M., Bilotsky, B. Model-free time-invariant evaluation of transport and efficacy of chemicals and drugs. *US Pat. Appl.* 2024/0047019 (2022).

Figures:

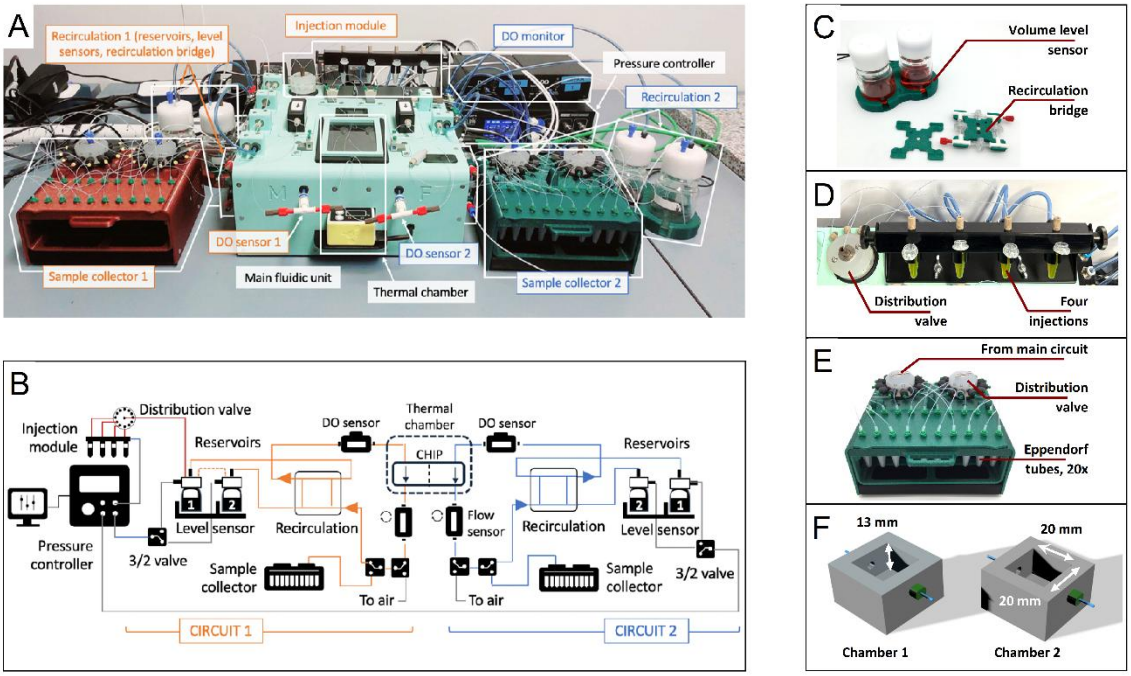

Figure 1. Microfluidic platform for automated molecular transport assays. (A) View of the whole microfluidic platform, composed of several modules (dark red: circuit 1, dark green: circuit 2, light green: main fluidic circuit module). (B) Scheme of the fluidic path in the two circuits (orange, blue). (C) Sensorized recirculation modules consist of flask holders with integrated volume level sensors and unidirectional recirculation bridge. The working principle of these modules is detailed in Figure 3. (D) Injection module composed of four Eppendorf holders and a MUX distribution rotary valve. The working principle of this module is further detailed in Figure 4. (E) Sample collection module adapted to up to 20 samples. (F) Schematic of the chip.

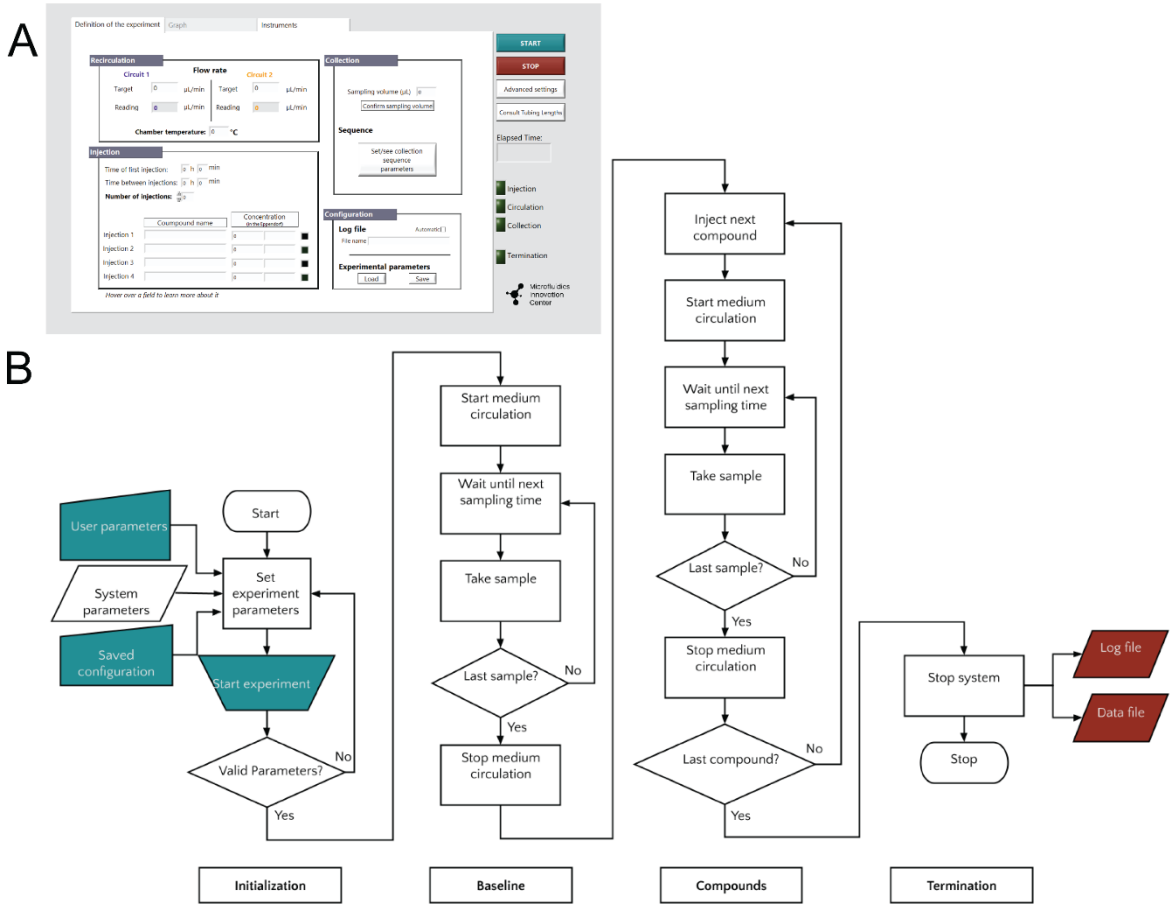

Figure 2. Software for platform operation. (A) Overview of parameters for user input in the "Definition of the experiment" tab. (B) Transport assay decision tree. User inputs (green shapes) and outputs (red shapes) of the software are indicated. The flowchart outlines the four experiment phases: initialization, acquisition of the baseline, acquisition of a given compound/ concentration (repeated as many times as requested) and termination.

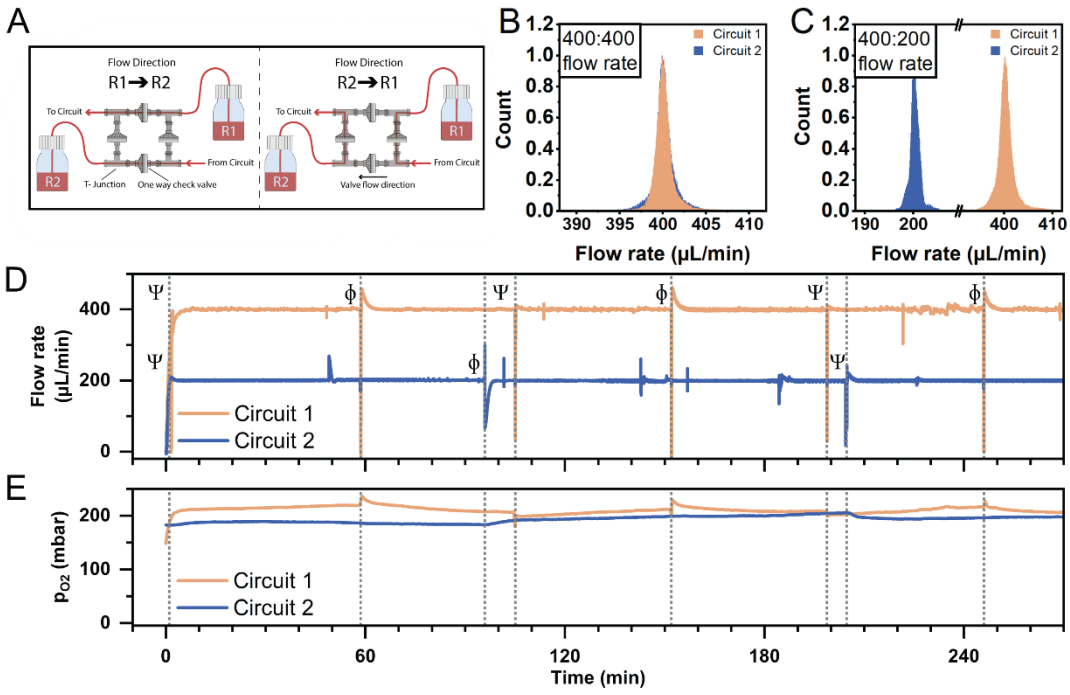

Figure 3. Performance of flow control and monitoring modules. (A) Two flow paths are possible in the recirculation bridge. Liquid flows from reservoir 1 (R1) or reservoir 2 (R2) depending on which is being pressurized. In both cases, the liquid is guided unidirectionally into the circuit from the top left corner and returns from the circuit to the bottom right corner of the bridge. (B) Normalized histograms of the flow rate values using the pressure controller software at set flow rates of 400 µL/min in both circuits (circuit 1, orange; circuit 2, blue). (C) Normalized histograms of the flow rate values using the pressure controller software (400 µL/min circuit 1, orange; 200 µL/min circuit 2, blue). (D) Flow rate profile over time using pressure controller software (400 µL/min circuit 1, orange; 200 µL/min circuit 2, blue). The alternating pressurization of reservoir 1 (Ψ) or 2 (ϕ) is indicated. (E) O_2 partial pressure measurement profile over time using pressure controller software (400 µL/min circuit 1, orange; 200 µL/min circuit 2, blue).

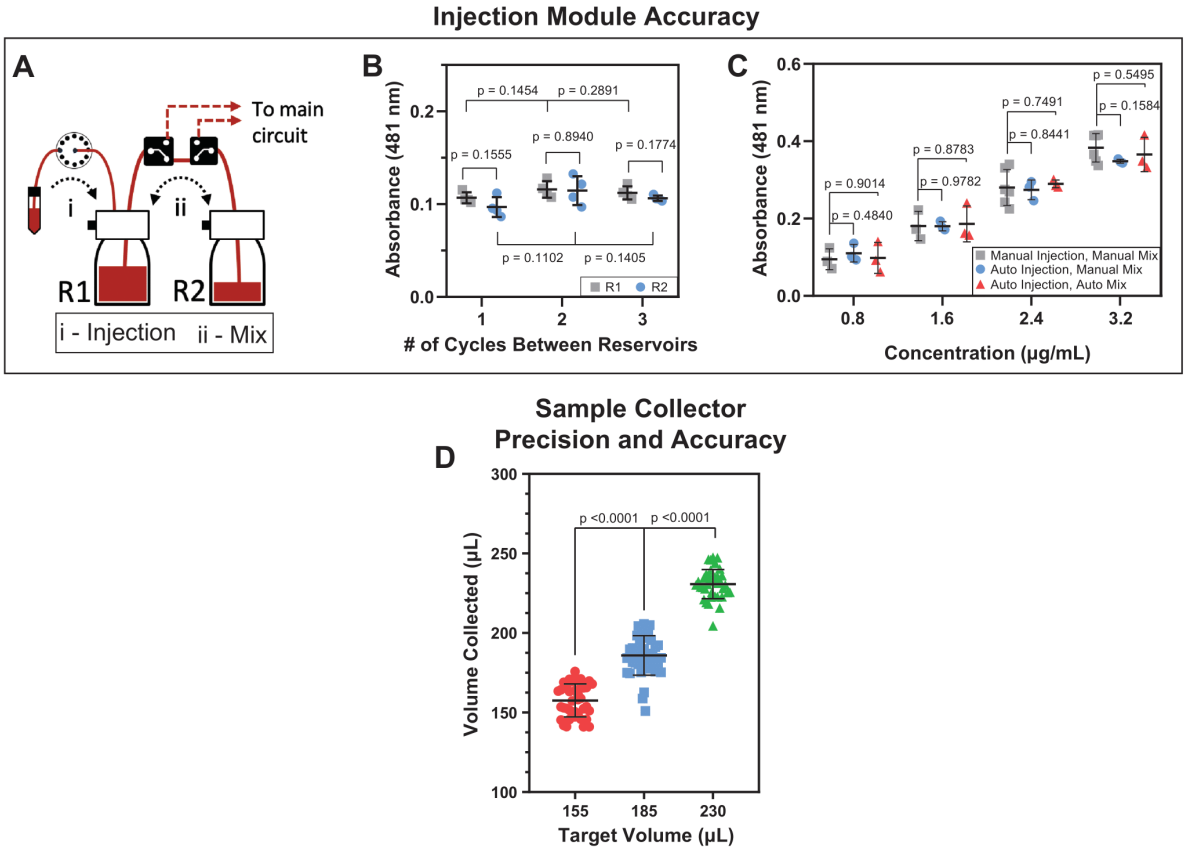

Figure 4. Performance of injection and collection modules. (A) Injection module working principle: i) The compound is injected into reservoir 1 of circuit 1. ii) The medium and the compound are circulated back and forth between reservoirs 1 and 2 of circuit 1 until homogenized. (B) Mixing efficiency of injected compound in reservoir 1 (black squares) and reservoir 2 (blue circles) as a function of the number of back-forth cycles. (C) Platform versatility for sequential injections: absorbance (mean ± SD, n=3-5) in reservoir 1 for four sequential injections of fluorescein in the case of manual injection and shaking (black squares), automated injection with the microfluidic platform and manual shaking (blue circles) or automated injection and three automated back-forth mixing cycles (red triangles). (D) Volume consistency during sample collection for three independent target sample volumes, 155 µL, 185 µL, 220 µL (n=40 for each case). p values were calculated using an unpaired t-test.

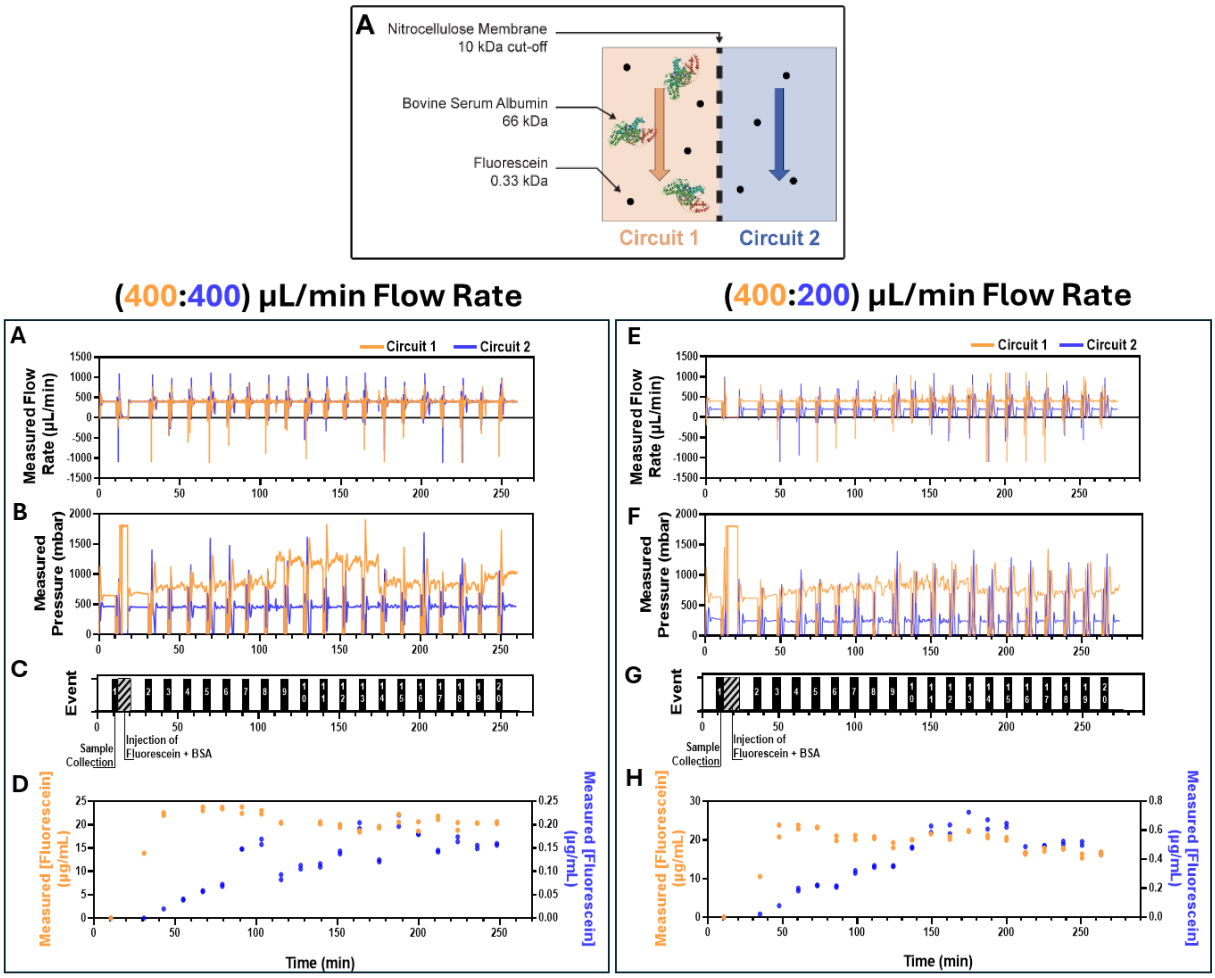

Figure 5. Automated microfluidic platform analysis of molecular transport in a non-equilibrium system under different flow rates. (A) Schematic of flow directionality inside the chip. (B-I) Demonstration of full platform performance and proof of concept of its automation for molecular transport dynamics across a semipermeable barrier at (400:400) µL/min (B-E) and (400:200) µL/min (F-I) flow rate ratios. Synchronized measured flow rate, pressure, timing of injection and sample collection and, measured fluorescein concentration in circuit 1 and circuit 2 at different flow rates.

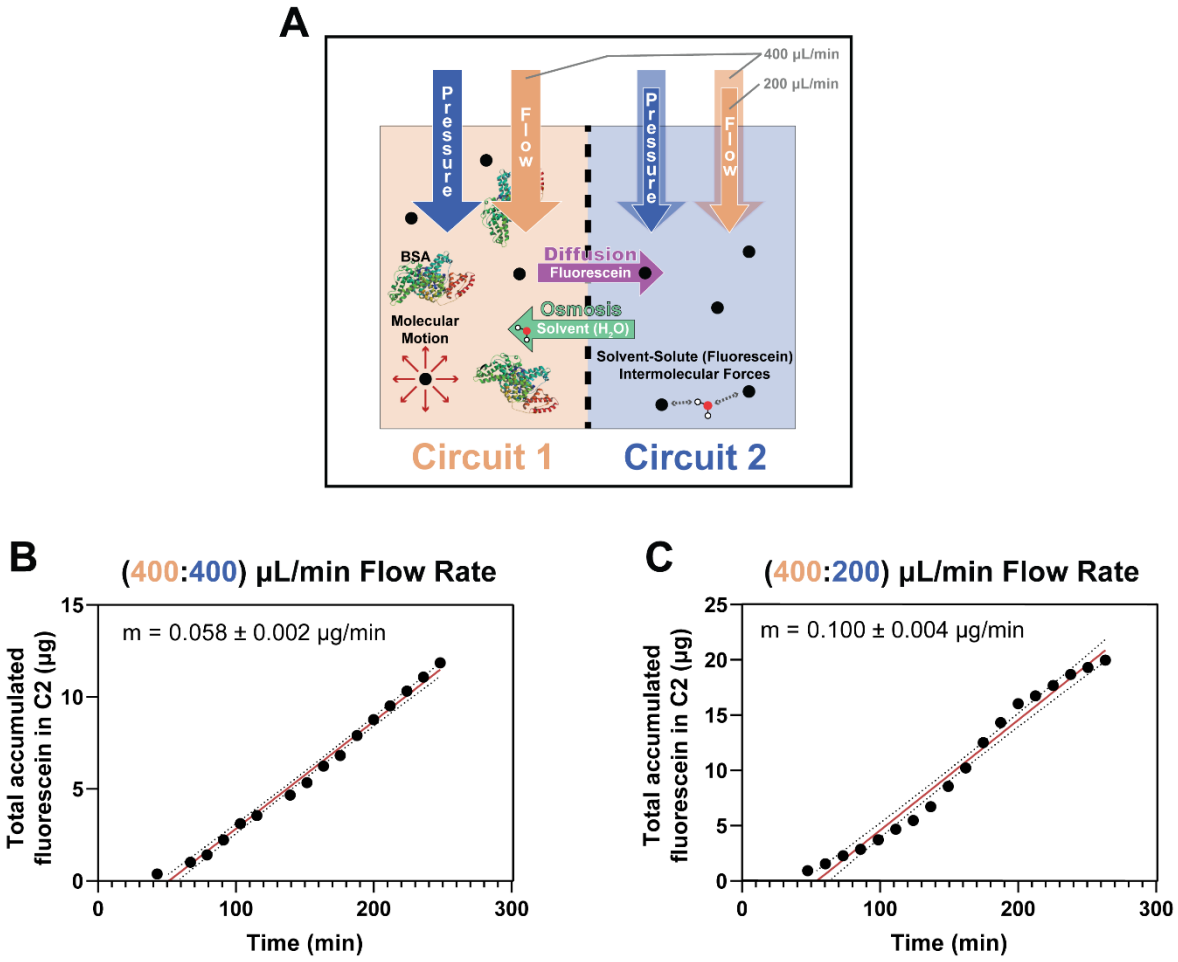

Figure 6. Fluorescein transport rates from circuit 1 to circuit 2 calculated from the flow rate and fluorescein concentration data in Fig 5. (A) Diagram depicting the different forces affecting the passive transport of fluorescein from circuit 1 to circuit 2. (B and C) Total fluorescein transport from circuit 1 into circuit 2 over time at the different flow rates evaluated.

Supplementary Information

Automated Microfluidic Platform for Molecular Transport Analysis Across Biomimetic Interfaces

Olivier Fournier[1], Miguel A.D. Neves[2,3], Théo Gavoille[1], Alan Morin[1], Beatriz Pais[2,3,4], Ivana Brenta[1], Justine Lereculey-Beaumanoir[1], Andrea Cruz[5], Denis Santos[5], Hugo Oliveira[5], Michael Gasik[6], Lisa D. Muiznieks[1,*], Inês Mendes Pinto[2,3,*]

[1] Microfluidics Innovation Center, 172 rue de Charonne 75011 Paris, France;
[2] Institute for Research and Innovation in Health (i3S), University of Porto, 4200-135 Porto, Portugal;
[3] Molecular and Analytical Medicine Laboratory, Department of Biomedicine, Faculty of Medicine, University of Porto, 4200-319 Porto, Portugal;
[4] NOVA School of Science and Technology, Physics Department, NOVA University of Lisbon, 2829-516 Caparica, Portugal;
[5] International Iberian Nanotechnology Laboratory (INL), 4715-330 Braga, Portugal;
[6] Seqvera Ltd. Oy, 00290 Helsinki, Finland.

*Co-corresponding authors: Lisa D. Muiznieks (lisa.muiznieks@microfluidic.fr) and Inês Mendes Pinto (ines.pinto@i3s.up.pt)

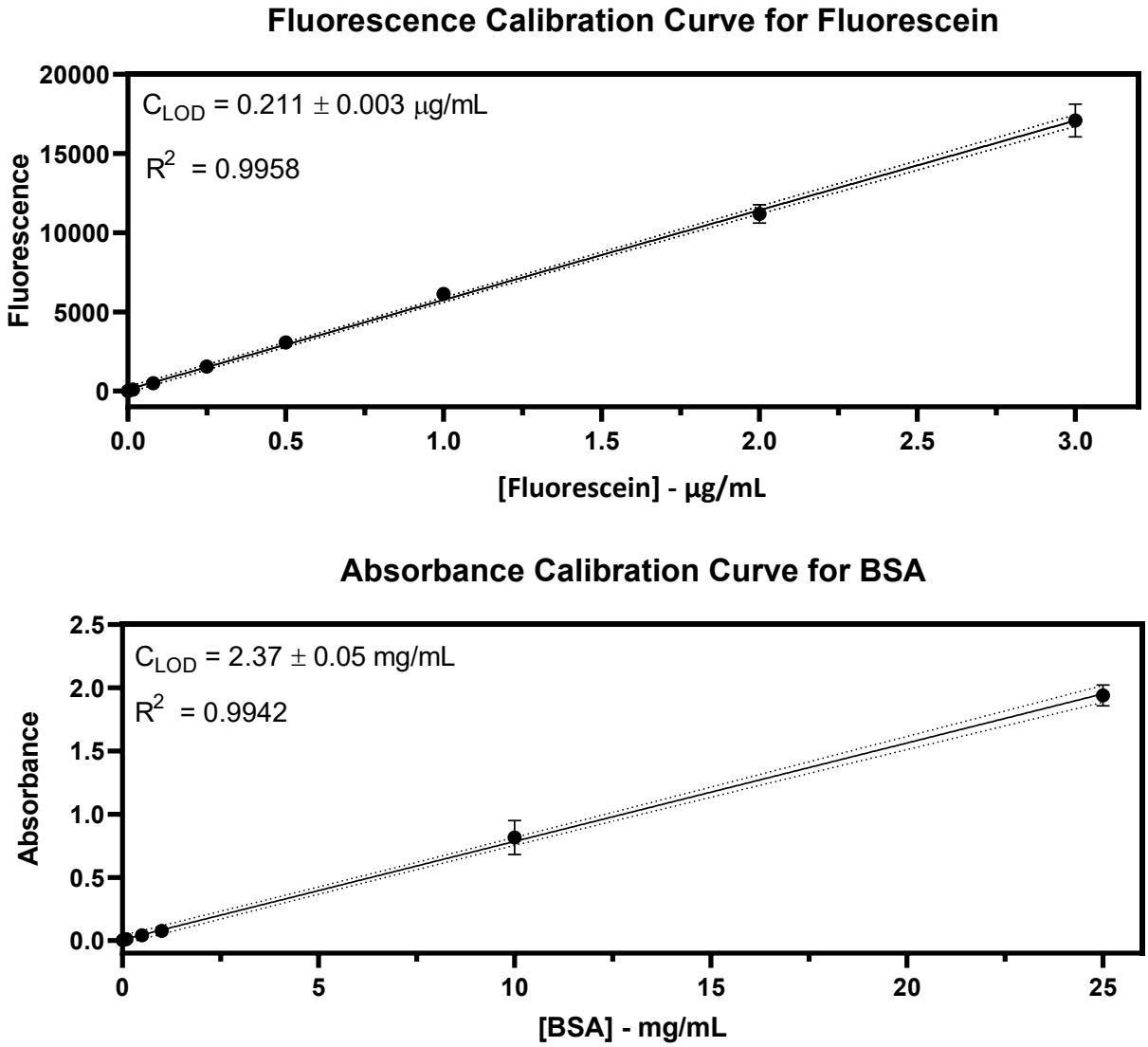

Supplementary Figure 1. Mean fluorescence and absorbance measurements for spiked concentrations of fluorescein and BSA. Data presented as mean ± SD (n = 3).

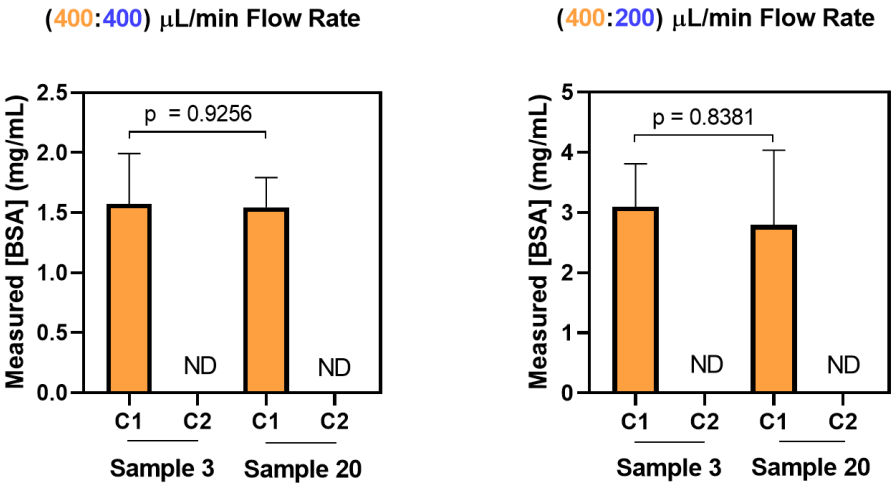

Supplementary Figure 2. Mean ± SD concentrations of BSA (n = 3–6) in circuits 1 and 2 at various flow rates, measured at the beginning (sample 3) and end (sample 20) of the experiments. ND corresponds to *not detected*.

I

Annex

In this Annex, pictures of the instruments used to compose the microfluidic system are available.

Figure I.1: **Elveflow® OB1 MK4 pressure and vaccum controller.** As input, an external pressure (air compressor, local pressure network or gas cyclinder) or vaccum source needs to be connected. It features a USB entry allowing pressure monitoring and sequence automation using a dedicated software. It pressurizes up to four reservoirs and can also connect to up to four flow sensors at the same time. It uses piezoelectric technology which gives more precise and faster flow control than other technologies available in the market. Mainly, its advantages are that it has a fast settling time (around 40 ms) and a highly stable and pulseless flow. Adapted from [97].

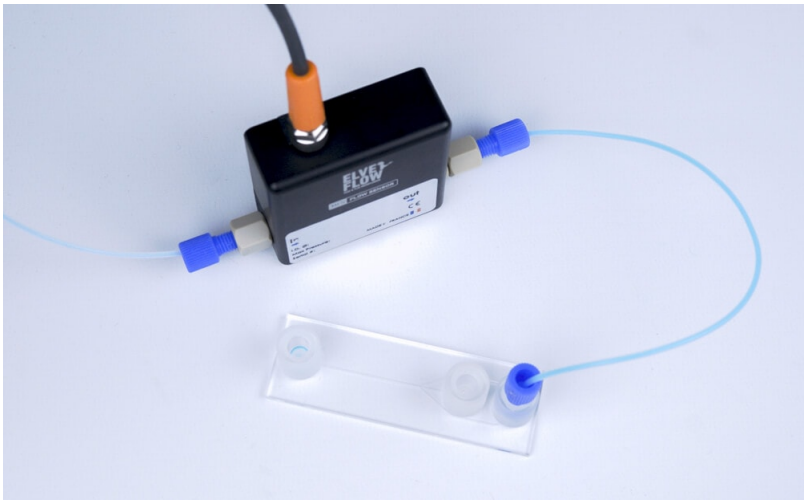

Figure I.2: **Elveflow® standard flow rate sensor.** It makes use of a feedback loop control on the software, so that flow rates' monitoring is precise. Adapted from [98].

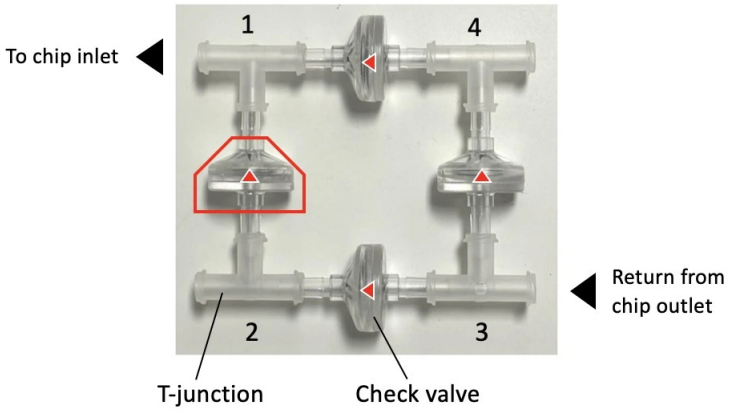

Figure I.3: **Recirculating bridge composed of T-junctions and check valves.** The direction of the flow is indicated by the red arrows and the check valves prevent fluid from going backwards. Adapted from [28].

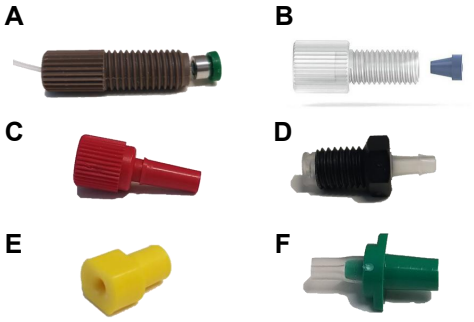

Figure I.4: **Different tubing connectors used in the microfluidic system. (A)** ¼″-28 male to 1/32″ OD tubing connectors. **(B)** ¼″-28 male to 1/16″ OD tubing connectors. **(C)** ¼″-28 female to Luer male connectors. **(D)** ¼″-28 swivel to barbed 3/32″ ID connectors. **(E)** Mini-Luer to 1/32″ OD tubing tuck-in connectors. **(F)** Silicon sleeve tubing connected to a Luer male adaptor.

2025 Automated Microfluidic Platform for Quantitative Analysis of Molecular Transport across Biomimetic Interfaces Beatriz Pais

NOVA